

LIBRARY
Michigan State
University

This is to certify that the

dissertation entitled

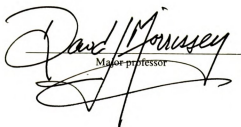
Multi-Particle Correlations
with Intermediate Energy
Heavy Ion Reactions

presented by

ZACHARY MORDECAI KOENIG

has been accepted towards fulfillment
of the requirements for

PH.D. degree in Chemistry


Major professor

Date May 12, 1986



RETURNING MATERIALS:
Place in book drop to
remove this checkout from
your record. FINES will
be charged if book is
returned after the date
stamped below.

DEC 10 2003
0127 03



MULTI-PARTICLE CORRELATIONS
WITH INTERMEDIATE ENERGY
HEAVY ION REACTIONS

By

Zachary Mordecai Koenig

A DISSERTATION

Submitted to
Michigan State University
in partial fulfillment of the requirements
for the degree of

DOCTOR OF PHILOSOPHY

Department of Chemistry

1986



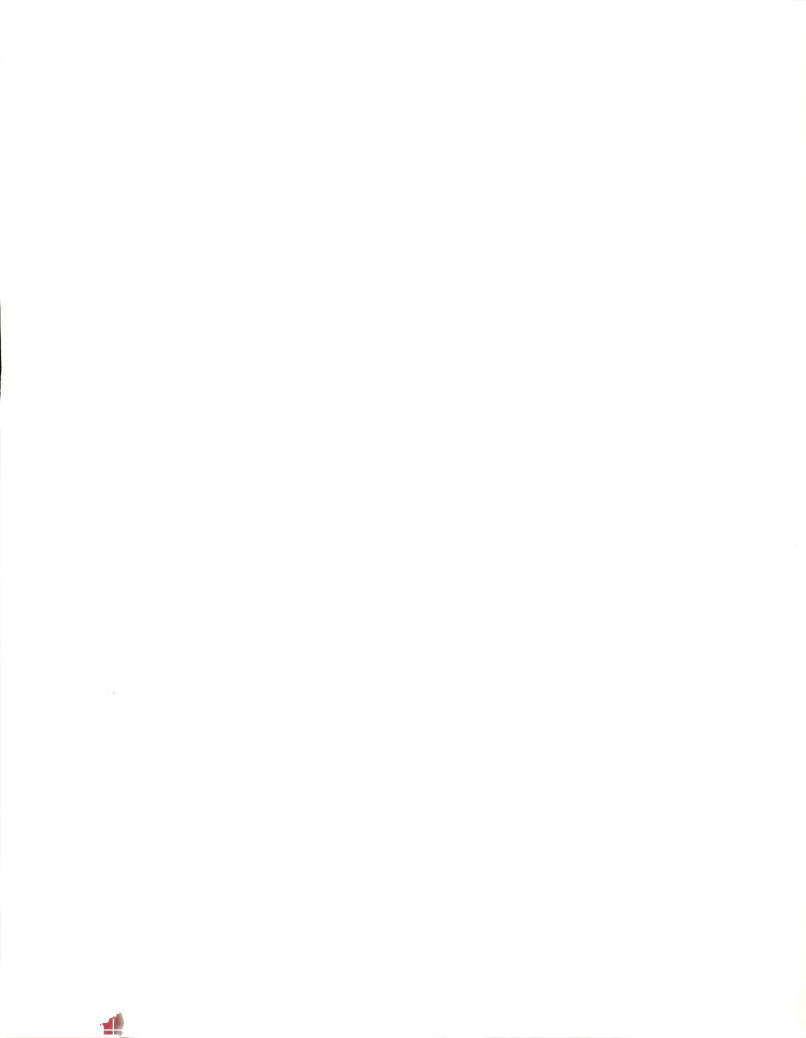
ABSTRACT

MULTI-PARTICLE CORRELATIONS WITH INTERMEDIATE ENERGY HEAVY ION REACTIONS

By

Zachary Mordecai Koenig

Light particle ($Z \leq 2$) inclusive and coincidence spectra have been measured for the reactions 15 and 30 MeV/nucleon $^{12}\text{C} + \text{Au}, \text{C}$ at angles of ± 45 and 90 degrees. The coincident triggers for the light particle spectra were projectile-like fragments ($3 \leq Z \leq 7$) at 15 degrees and target-like fragments ($3 \leq Z \leq 7$) at 45 degrees. The inclusive and coincidence spectra are fit to a single moving source parameterization and very little difference between the inclusive and triggered data were observed. Evidence for some collective, dynamic effects were found, light particle spectra triggered by the small impact parameter collisions of the deep-inelastic part of the projectile-like fragment spectra in the 30 MeV/nucleon C+C data. Light particle spectra triggered on the target-like fragments and the quasi-elastic part of the projectile-like spectra showed much less opposite to same side asymmetry. A momentum conservation calculation in the context of a thermal moving source was found to consistently overpredict the opposite to same side ratios, indicating that the coincident particles come from different sources.



ACKNOWLEDGMENTS

I wish to thank Dr. Gary Westfall, my research advisor, for his guidance, support, and encouragement throughout my graduate career. I would also like to thank Drs. David Scott and David Morrissey, my academic advisors, for their assistance and guidance.

In addition, I would like to thank Drs. Gary Crawley, Dag Horn, Konrad Gelbke, Robert Tickle, Leigh Harwood, and Horst Stocker for their time and effort toward this work.

I would like to thank Ron Fox and John Yurkon for their invaluable help in making this project work.

I wish to thank the friendship and support of my fellow graduate students; Bruce Hasselquist, Barbara Jacak, Charles Chitwood, Dan Fox, Bruce Remington, and Dan Cebra.

I would like to thank my parents, without who all of this would not have been possible.

Most of all, I would like to thank Dr. Joan Kotun for her support, encouragement, and love.



TABLE OF CONTENTS

	PAGE
List of Tables	v
List of Figures	vi
CHAPTER	
I. INTRODUCTION	1
II. DETECTION DEVELOPMENT	11
A. Bragg Curve Detector	11
B. Hit Detector	29
III. EXPERIMENTAL	34
A. Experimental Setup	34
B. Data Reduction and Analysis	39
C. Reaction Loss Correction	40
D. Scattering Out Correction	43
IV. RESULTS	45
A. 15 and 30 MeV/A $^{12}\text{C}+\text{Au,C}$ Inclusive ..	45
1. Light particle inclusive spectra	45
2. Moving Source Parameterization	50
3. Bragg Curve Inclusive Spectra	54
4. Projectile-Like Fragment Spectra	54
B. 15 and 30 MeV/A $^{12}\text{C}+\text{Au,C}$ coincidence	63
1. Momentum Conservation Model ...	63
2. Light particle-Bragg Curve	65
3. Light particle-Projectile Frag.	70
4. Same side to Opposite side	85
V. SUMMARY AND CONCLUSIONS	116



A. Summary of results	116
B. Conclusion	118

APPENDIX

REFERENCES	123
------------------	-----



LIST OF TABLES

TABLE		PAGE
II-1.	Calcium Fluoride Punch Through Energies (MeV/A)	32
III-1.	Detector Angles	36
IV-1.	Moving Source Parameters for 30 MeV/A C+Au,C (Inclusive)	55
IV-2.	Moving Source Parameters for 15 MeV/A C+Au,C (Inclusive)	56
IV-3.	Moving Source Parameters for 30 MeV/A C+Au+p (Coin. HP)	71
IV-4.	Moving Source Parameters for 30 MeV/A C+Au+p (Coin. BP)	72
IV-5.	Moving Source Parameters for 30 MeV/A C+C →p (Coin. BP)	73
IV-6.	Moving Source Parameters for 30 MeV/A C+C →p (Coin. HP)	74
IV-7.	Moving Source Parameters for 15 MeV/A C+C →p (Coin. HP)	75
IV-8.	Moving Source Parameters for 15 MeV/A C+C →p (Coin. BP)	76
IV-9.	Moving Source Parameters for 15 MeV/A C+Au+p (Coin. HP)	77
IV-10.	Moving Source Parameters for 15 MeV/A C+Au+p (Coin. BP)	78

LISTS OF FIGURES

FIGURE		PAGE
I-1	Schematic illustration of two possible heavy-ion processes, a) fireball model b) hydrodynamic model	5
II-1	Schematic representation of the Bragg Curve System (BCS)	12
II-2	Schematic view of the Bragg Curve Spectrometer	15
II-3	Schematic view of the Frisch grid/anode geometry for the BCS	17
II-4	Diagram for two different read out techniques for the BCS	18
II-5	Top: two-dimensional plot of Z (horizontal) Vs. E (vertical) for the reaction $^{14}\text{N} + ^{197}\text{Au}$ at 35 MeV/A. Bottom: projected Z spectrum for the same reaction	19
II-6	Charge spectrum from the BCS for the reaction $^{35}\text{Cl} + ^{58}\text{Ni}$ at 230 MeV	21
II-7	Calibration plot for the BCS for 30 MeV/A C+C	23
II-8	"Snapshot" of the BCS, i.e. the digitized current output as measured with the flash encoder	24
II-9	Timing diagram for the scintillator array telescopes. The anode is a sum of the fast plastic scintillator component and the slow CaF_2 component .	26
II-10	Contour plot of the ΔE (vertical) Vs. E (horizontal) for a CaF_2 /plastic scintillator telescope in the BCS	27
II-11	Seven telescope scintillator array used in the Hit detector, i.e. the Hit plastics (HP)	30

II-12	Contour plot of the ΔE (vertical) Vs. E (horizontal) for a CaF_2 / plastic scintillator telescope in the Hit detector	31
III-1	Chamber setup during the experiment	35
III-2	Electronics schematic for the experiment	38
IV-1	Light particle inclusive energy spectra for 15 MeV/A C+Au	46
IV-2	Light particle inclusive energy spectra for 15 MeV/A C+C	47
IV-3	Light particle inclusive energy spectra for 30 MeV/A C+Au	48
IV-4	Light particle inclusive energy spectra for 30 MeV/A C+C	49
IV-5	Inclusive energy spectra for Be, B and C from the 30 MeV/A C+C reaction, as measured with the BCS	57
IV-6	Projectile-like fragment inclusive energy spectra for the PLF detector at 15° for 15 MeV/A C+Au	58
IV-7	Projectile-like fragment inclusive energy spectra for the PLF detector at 15° for 15 MeV/A C+C	59
IV-8	Projectile-like fragment inclusive energy spectra for the PLF detector at 15° for 30 MeV/A C+Au	60
IV-9	Projectile-like fragment inclusive energy spectra for the PLF detector at 15° for 30 MeV/A C+C	61
IV-10	The weighted distribution of source sizes for the momentum conservation calculation based on $2\pi bN(b)$ for C+Au..	66
IV-11	The weighted distribution of source sizes for the momentum conservation calculation based on $2\pi bN(b)$ for C+C. .	67

IV-12	Energy spectra for protons at 45° in the Hit plastics in coincidence with the BCS for 30 MeV/A C+Au. Solid lines correspond to a moving source fit.	68
IV-13	Energy spectra for protons at 45° in the Hit plastics in coincidence with the BCS for 30 MeV/A C+C. Solid lines correspond to a moving source fit.	69
IV-14	Ratio of coincident to inclusive temperatures from the moving source fits of protons for the quasi-elastic (QE), deep-inelastic (DI) and the bragg curve (BC) as a function of fragment mass from 30 MeV/A C+Au.	79
IV-15	Ratio of coincident to inclusive temperatures from the moving source fits of protons for the quasi-elastic (QE), deep-inelastic (DI) and the bragg curve (BC) as a function of fragment mass from 30 MeV/A C+C.	80
IV-16	Energy spectra for protons at 45° in the Hit plastics in coincidence with the QE for 30 MeV/A C+Au. Solid lines correspond to a moving source fit.	81
IV-17	Energy spectra for protons at 45° in the Hit plastics in coincidence with the DI for 30 MeV/A C+Au. Solid lines correspond to a moving source fit.	82
IV-18	Energy spectra for protons at 45° in the Hit plastics in coincidence with the QE for 30 MeV/A C+C. Solid lines correspond to a moving source fit.	83
IV-19	Energy spectra for protons at 45° in the Hit plastics in coincidence with the DI for 30 MeV/A C+C. Solid lines correspond to a moving source fit.	84
IV-20	Proton energy spectra for the HP (opp. side) and the BP (same side) in coincidence with a lithium in the BCS for 30 MeV/A C+C. The solid (dashed) lines correspond to single (weighted) source momentum conservation calculation. The single source used 24 nucleons.	87

IV-21	Proton energy spectra for the HP (opp. side) and the BP (same side) in coincidence with a carbon in the BCS for 30 MeV/A C+C. The solid (dashed) lines correspond to single (weighted) source momentum conservation calculation. The single source used 24 nucleons.	88
IV-22	Proton energy spectra for the HP (opp. side) and the BP (same side) in coincidence with a lithium in the BCS for 30 MeV/A C+Au. The solid lines correspond to single (38 nucleons) source momentum conservation calculation.	90
IV-23	Proton energy spectra for the HP (opp. side) and the BP (same side) in coincidence with a carbon in the BCS for 30 MeV/A C+Au. The solid lines correspond to single (38 nucleons) source momentum conservation calculation.	91
IV-24	Ratio of opposite (HP) to same (BP) side temperatures from the moving source fits for 15 MeV/A C+Au for protons.	92
IV-25	Same as FIGURE IV-24 for 15 C+C.	93
IV-26	Same as FIGURE IV-24 for 30 C+Au.	94
IV-27	Same as FIGURE IV-24 for 30 C+C.	95
IV-28	Ratio of opposite (HP) to same (BP) side velocities from the moving source fits for 30 MeV/A C+Au for protons.	97
IV-29	Ratio of opposite (HP) to same (BP) side integrated cross sections for for 30 MeV/A C+Au for protons.	98
IV-30	Same as FIGURE IV-29 for deuterons.	99
IV-31	Same as FIGURE IV-29 for tritons.	100
IV-32	Same as FIGURE IV-29 for ^4He	101
IV-33	Same as FIGURE IV-29 for 30 MeV/A C+C. ..	102
IV-34	Same as FIGURE IV-33 for deuterons.	103
IV-35	Same as FIGURE IV-33 for tritons.	104
IV-36	Same as FIGURE IV-33 for ^3He	105

IV-37	Same as FIGURE IV-33 for ^4He	106
IV-38	Same as FIGURE IV-29 for 15 MeV/A C+Au. .	107
IV-39	Same as FIGURE IV-38 for deuterons.	108
IV-40	Same as FIGURE IV-38 for tritons.	109
IV-41	Same as FIGURE IV-29 for 15 MeV/A C+C. ..	110
IV-42	Same as FIGURE IV-41 for deuterons.	111



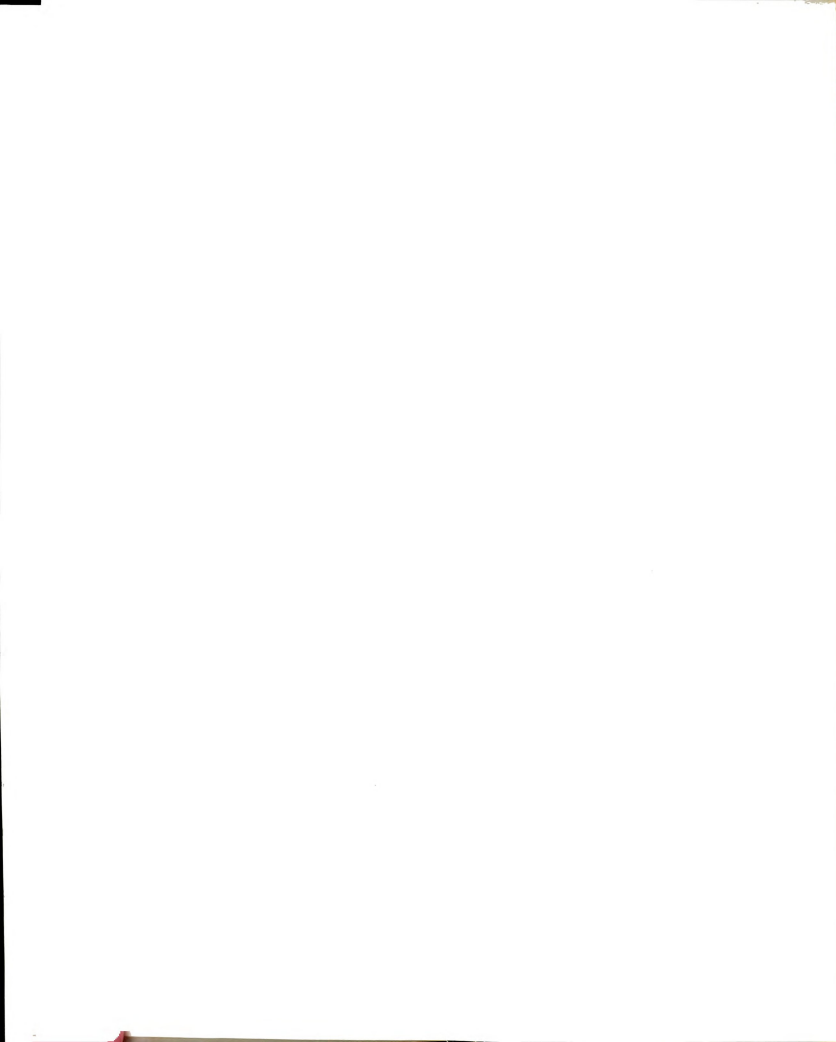
CHAPTER I

INTRODUCTION

Research scientists have for years used heavy ion beams to probe the structure and dynamical properties of the nucleus. Heavy ions with bombarding energies below 10 MeV/nucleon and at relativistic energies above 200 MeV/nucleon have been studied extensively [Sc 81]. Nuclear science has over the last few decades, used nuclear spectroscopy as a means to study the nucleus at the low excitation energies by studying giant dipole resonance, giant quadrupole resonance, and transfer reactions.

Higher energies allow one to investigate the properties of hot and dense nuclear matter. The collective and dynamical effects of a strongly interacting many body system is observed at these higher excitation energies and compared to such models as hydrodynamics [St 80] and cascade [Kr 85].

Particle emission is the primary mode of de-excitation. For low energy nuclear reactions, a compound nucleus can be formed and decays after full statistical equilibrium is reached. The decay of the compound nucleus can be understood in terms of the Hauser-Feshbach theory [Ha 52] and fermi gas formulation. With increasing energy, light particle emission prior to the attainment of full statistical equilibrium becomes important, termed pre-equilibrium particles, possibly showing some forms of



collective and dynamic effects. As the energy is raised, the concept of an expanding gas of nuclear matter in thermodynamic equilibrium becomes applicable. These ideas have been successfully applied to light particle emission from a variety of systems [Go 78, Ka 77]. The understanding of the reaction mechanisms in these two energy regimes has developed two very different theoretical models. Collisions in the low energy regime are dominated by the nuclear mean field, with such dynamical models as the time-dependent Hartree-Fock (TDHF) approach [Wo 82]. At very high energies a pure mean-field approach becomes inadequate and instead, dynamical models such as hydrodynamics or two-body scattering become important [St 80, Sc 81].

In the intermediate energy region between 10 and 200 MeV/nucleon a transition is expected to occur from the mean field description of low energy interactions to the nucleon-nucleon scattering behavior characteristic of high energy collisions [Sc 81]. This transition is expected to result when the velocity of the colliding nucleons surpasses both the Fermi velocity and the velocity of nuclear sound. It is however, unlikely that the transition is a sharp one [Ja 84]. This critical transition region is where the possible coexistence of the gas and liquid phases may be present with possible signatures of a liquid-gas phase transition [Ro 82]. The experimental observation of a phase transition and the determination its critical temperature would be of interest in studying an equation of state for nuclear



matter. The current generation of nuclear accelerators, including the super conducting cyclotron facility here at Michigan State University, are well suited to study this region of transition between 10 and 200 MeV/nucleon, along with GANIL, ORNL, LBL, and SARA.

The observation of energetic light particles (p, d, t, ^3He , and α) is a useful method for studying heavy ion reactions. These particles are assumed to originate from the overlap of the projectile and target. The first generation of experiments was to measure the inclusive spectra of light particles produced in these collisions. The data has been analyzed with the participant-spectator model in which the light particles, emitted from a thermalized participant region of target and projectile nucleons, are fitted to the energy spectra assuming a single moving source. The parameters extracted from these fits have been very useful in quantifying a large amount of data. The fitting processes will be described in more detail in chapter IV. The parameters describing the data have been shown to vary smoothly with bombarding energy [We 82], indicating that the transition to mechanisms typical of relativistic energy reactions is a smooth one. At these energies, 15 and 30 MeV/nucleon, it has been suggested that the participants and spectators are not well separated. There is instead a local thermalized zone, or hot spot, which is formed [Go 79, St 81, Fr 83, Fi 84]. This hot spot begins to break away from the target as the bombarding

energy increases and becomes an independent participant zone. This heated region of the nuclear surface would attain much higher temperatures than the compound nucleus and after its formation would possibly decay by thermal diffusion into the adjacent nuclear matter or by the emission of energetic light particles. Taking a more dynamical approach, intermediate or lighter mass particles might be emitted from the target due to the transfer of momentum showing some form of a collective, dynamical effect.

The emission of particles from heavy ion reactions can be broken up into two major modes. The first of which describes the particles as being emitted from a thermalized source in a statistical framework. The particles are usually fitted to a Maxwell-Boltzmann distribution and assumptions about thermal and chemical equilibrium are usually made. Models that have incorporated this form of emission include the Fireball [We 76] and Quantum Statistical [Gos 78, Su 81, St 83] models. The second mode assumes the particles are emitted from a dynamical framework. These models incorporate a two-body or fluid dynamical approach to a calculation and examples include the single scattering knock-out [Ko 77, Ha 79], cascade [Be 76, Ya 81, Cu 82, To 83, Kr 85], and hydrodynamic [Bu 81, St 80, Bu 83] models. Figure I-1 shows a comparison of these two approaches with an incoming projectile on a stationary target nucleus in the lab frame [We 83], Figure I-1a shows the

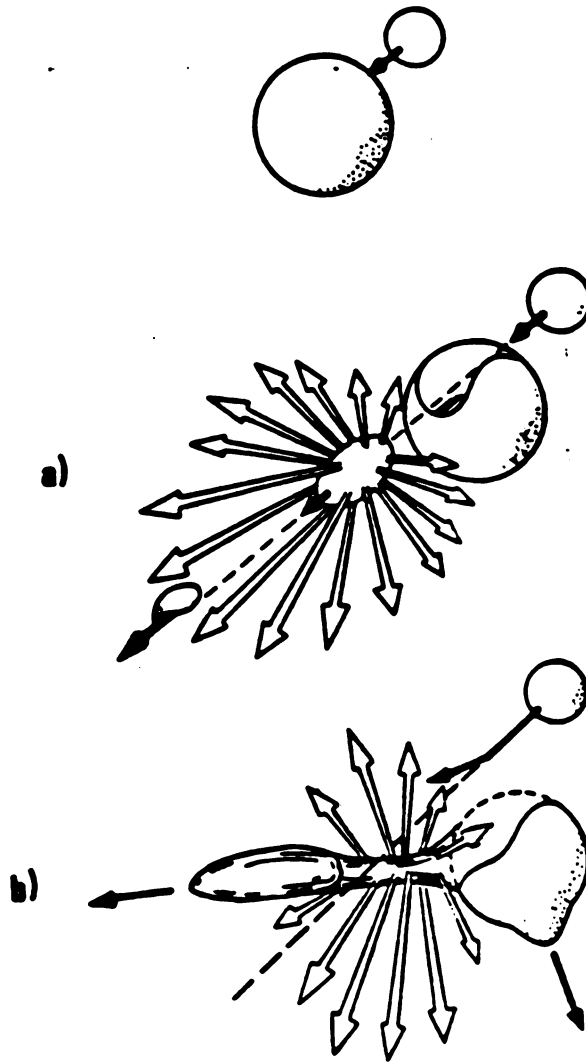


FIGURE I-1. Schematic illustration of two possible heavy-ion processes, a) fireball model b) hydrodynamic model.

geometry of the Fireball model [We 76] and Figure I-1b is an example of the hydrodynamical approach [St 80]. These two modes on the other hand are not mutually exclusive. For these intermediate energy reactions, a more realistic approach would be a combination of these two methods of particle emission. All of these models do a good job of predicting the inclusive data. To distinguish among them one must use coincidence measurements to separate different classes of events.

Evidence for thermal emission is abundant as will be seen later, but observations of dynamical effects are not as easy. Dynamical effects require complex coincidence experiments (i.e. the plastic ball) whereas evidence for thermal emission can be found in inclusive singles data.

It has been shown that for the lower intermediate energy regime, < 40 MeV/nucleon, there is not enough excitation energy in the hot participant region to unbind it into free nucleons [Ga 80]. Fragment production is relatively more important at lower energies. Unlike the relativistic energy heavy ion reactions, these lower energy reactions must take into account the more complex fragments ($A \leq 14$). The complex fragments may carry information about the reaction, such as entropy, temperature, etc.. The second generation of experiments was to measure the inclusive cross sections of these complex fragments [Ja 83, Fi 84]. Jacak has shown that these intermediate mass fragments, which were also fit to a single moving source,

were found to have a velocity intermediate to that of the projectile and target, and its temperature was independent of fragment mass [Ja 83]. This suggests that these complex fragments as well as the light particles are emitted from a thermalized region of the reaction. Single particle inclusive measurements are very useful for obtaining a survey of the data and comparison to theoretical models.

The next generation of experiments in order to better understand heavy ion reactions are coincidence measurements. Coincidence experiments are needed to determine specific reaction mechanisms and observe any collective or dynamic effects. They allow one to tag each coincidence event based on different event topologies. For example, observing a projectile like fragment could determine the reaction plane or determining the multiplicity of charged particles can provide information on the impact parameter.

Intermediate energy heavy ion coincidence experiments is an area of intense current research. Some experiments in this area include two-particle correlations [Ch 85, Fo 85, Po 85], neutron - complex fragment coincidence [Ca 85], light particle - complex fragments [Bh 79, Ho 80, Ha 85], and several others. Awes examined the emission of projectile like fragments and light particles in coincidence with fission fragments for 20 MeV/nucleon ^{16}O -induced reactions on ^{238}U [Aw 81]. It was found that a large portion of the linear momentum lost by the projectile residue was observed to be transferred to the target

residue. This would indicate a strong interaction between the target and projectile, with the target absorbing a portion of the projectile. Tsang et al. found a preference for two light particles in coincidence to be emitted on opposite sides of the beam axis for 25 MeV/nucleon $^{16}\text{O}+\text{C}$ [Ts 84], which would increase with the mass of the light particle. The two light particles were measured at scattering angles of 40 and 70° with azimuthal angles ranging from 0 to 180°. Azimuthal angles of 0 and 180° would correspond to the same and opposite sides of the beam axis, respectively. They also found that for 25 MeV/nucleon $^{16}\text{O}+\text{Au}$, there was a slight opposite side enhancement for protons which decreases to a small same side enhancement with an increase in the mass of the light particles. Hasselquist et al. have found little difference between inclusive and complex fragment triggered coincidence cross sections for light particles of 30 MeV/nucleon $^{12}\text{C}+\text{Al},\text{Au}$ [Ha 85]. This would indicate that all the fragments would have a common source, yet any observation of collective effect was not possible. The next most logical step would be to measure light particles in coincidence with complex fragments on both the same and opposite sides of the complex fragments.

The most encompassing coincident experiments are those which detect particles with an almost 4π acceptance. These experiments would include streamer chamber [Sa 83], emulsion, and the plastic ball experiments [Gu 83], each of



which have their limitations. The study of multi-particle final states with the plastic ball have all been concentrated on incident energies above 200 MeV/nucleon. It has a lower energy cut off of ≈ 40 MeV/nucleon and cannot observe complex fragments, except under special kinematic situations, which for energies below 200 MeV/nucleon has been shown to be major factor for heavy ion reactions [Ja 83]. The emulsion and streamer chamber data is hampered by insufficient statistics, although recent results with CCD cameras will help this problem for steamer chambers in the future [An 85].

Evidence for a dynamic, collective effect has been observed in relativistic energy heavy ion reactions [Gu 84, Bu 84]. The present work seeks to study collective effects in nucleus-nucleus collisions at intermediate energies. The results from 15 and 30 MeV/nucleon $^{12}\text{C}+\text{C}, \text{Au}$ carried out on the K-500 cyclotron at the National Superconducting Cyclotron Laboratory will be presented in this thesis. Light particle spectra ($Z \leq 2$) and complex fragments ($3 \leq Z \leq 7$) have been measured in various inclusive and coincidence modes. The light particle inclusive spectra were measured at 45 and 90° in the laboratory. The energy spectra of the light particles were measured, on the same and opposite side at 45°, in coincidence with the complex fragments at 15 and 45°. This experiment has the unique characteristic of being able to measure both the light particle and heavy fragment at the same place and time. This fact allows one to measure



a same side coincidence at the same angle. The ratio of opposite to same side emission provides a quantitative comparison of coincidence cross sections, which is essential to observing collective, dynamic effects.

The thesis is organized as follows. Chapter II explains the theory and development of the two plastic scintillator arrays and the Bragg Curve detector. The experimental setup and complete data analysis is presented in Chapter III. This chapter includes all corrections to the light particle spectra for reaction loss, scattering out of the plastic scintillators, and normalizations. Chapter IV includes all of the results of the data, including the ratios of the integrated cross sections. An outline of the momentum conservation calculation used for comparison is presented along with a discussion of the observable trends in the data. A summary is presented in Chapter V of the findings of this thesis along with a discussion of the results and some possible future outlooks.

CHAPTER II

DETECTOR DEVELOPMENT

In order to do multi-particle experiments, a large number of relatively inexpensive light particle detectors had to be developed here at MSU. The first generation which was developed and used by Hasselquist [Ha 84], was a multi-wire proportional counter backed by an array of seven phoswich detectors for both particle identification and precise position information. This unit is referred to collectively as the "Hit Detector". The second generation was a Bragg Curve Spectrometer backed by an array of six phoswich detectors [We 85]. Both detector systems were used in the experiment to be described later, along with a silicon ΔE -E telescope for the projectile like fragments.

A. BRAGG CURVE DETECTOR

In order to detect a wide range of particles, it was necessary to develop a detector that was capable of stopping and identifying not only light particles but also medium mass nuclear fragments. This detector can be broken up into two separate subsystems (Fig. II-1); a Bragg Curve Spectrometer (BCS) that can stop and identify low energy, medium mass fragments (Li, Be, B, etc.) and an array of light particle telescopes that are capable of stopping and identifying light particles (p, d, t, ^3He , and ^4He). This

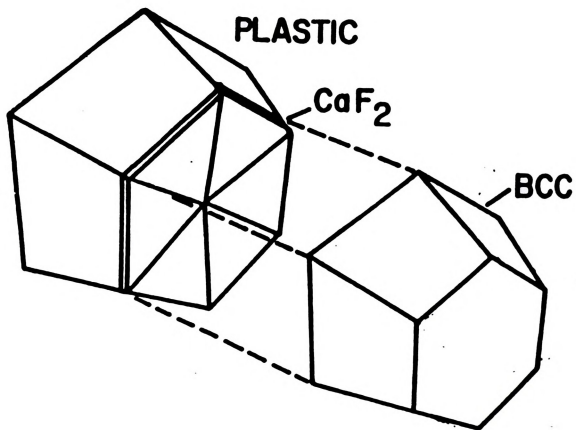


FIGURE II-1 Schematic representation of the Bragg Curve System (BCS).

detection system is unique in that it is capable of detecting both light and intermediate mass particles simultaneously at the same angle.

The first operational Bragg Curve Spectrometer (BCS) was suggested and constructed by Gruhn et.al. [Gr 82]. Several other groups since then have constructed BCS's based on similar concepts [Sc 82, As 82, Mc 84].

A Bragg Curve Spectrometer is basically an ionization chamber with its electric field parallel to the incoming particles to be detected. It is possible to determine the charge and energy deposited in the BCS for those particles that stop inside of the detector from a single signal. One takes advantage of the fact that the maximum specific ionization of a stopping ion is proportional to its atomic number. Therefore, by measuring the maximum of the ionization one can obtain the charge (Z) of the particle, and by measuring the integral of the ionization one obtains the energy that this particle had deposited in the detector. In principle, one can also determine the mass of the particle from either multiple ΔE measurements and by determining the range of the particle from a start signal from the cathode. For those particles that don't stop in the BCS, it is possible to use it as a simple ion chamber for a ΔE signal.

The electrons liberated by the ionization of the stopping charged particle drift to an anode which is shielded by a Frisch grid. Since the electric field is

parallel to the path of the particle, one measures the charge collected on the anode as a function of time, thus one obtains the complete energy loss distribution of the stopping ion. The range of subtended angles to be covered is very large and the information concerning the ionization of the stopping particles will be lost if the electrons do not drift parallel to the trajectory of the particle. Thus, a field shaping grid was installed inside the BCS to approximate a radial field. The design of this field shaping grid was calculated in cylindrical geometry with the program POISSON.

The main structure of the BCS is a truncated hexagonal pyramid made from 6.35 mm G10 fiberglass epoxy laminate (Fig. II-2). The length of the BCS is 15 cm, the entrance window which acts as the cathode, has a minor diameter of 10 cm and is made of 6 μm (or 800 $\mu\text{g}/\text{cm}^2$) thick aluminized mylar supported by a wire grid with 1 cm spacing. The distance between the cathode and the Frisch grid is 14 cm. The Frisch grid is made of 12.5 μm gold plated tungsten wires with 0.5 mm spacing. The anode is a similar wire grid located 1 cm behind the Frisch grid. The rear pressure window is formed by the scintillator telescopes. The BCS operates at a pressure of 500 torr Ar/CH₄ (90/10%) gas. The Frisch grid/anode geometry determines the shielding inefficiency [Fu 79], which for ion chambers in general is defined as:

$$\sigma = \frac{d}{2wb} \ln \frac{d}{2\pi r}$$

MSU-84-606

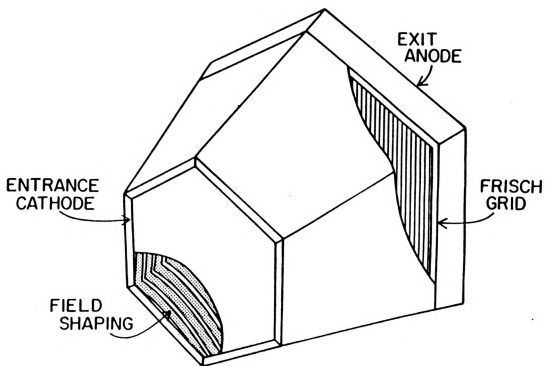


FIGURE II-2 Schematic view of the Bragg Curve Spectrometer.



where b is the grid/anode distance, and d and r are the spacing and the radius of the grid wires (Fig. II-3). For this detector $\sigma = 2\%$, indicating a very efficient shielding for good time and range resolution of the detector.

The Bragg Curve Spectrometer can be read out using two different techniques (Fig. II-4). After integration by a charge sensitive preamplifier, the anode signal of the BCS is split into two amplifiers with different time constants τ . One amplifier is set at $\tau_1 = 0.25 \mu\text{sec}$, and therefore basically measures the height of the peak of the signal which is proportion to the charge Z of the particle. The second amplifier is set at $\tau_2 = 6 \mu\text{sec}$, and therefore measures the area of the total signal which is the energy E of the particle.

Alternatively, the BCS can be read out by a flash encoding ADC as is indicated in Figure II-4 by dashed lines. The flash encoder integrates and digitizes the charge in 75 nsec bins and thus provides a "snapshot" of the particle going through the detector. Also here, the peak of the distribution is a measure of Z and the integral of the curve is the energy E .

Fig. II-5 shows results as obtained with a beam of 35 MeV/nucleon ^{14}N delivered by the K500 superconducting cyclotron of NSCL/MSU. Heavy fragments resulting from the reaction $\text{Au}(^{14}\text{N}, X)$ were detected. The detector was placed at 45° . The first (analog) read out method was used in this case. The top part of Fig. II-5 shows a two-dimensional

MSU-84-585

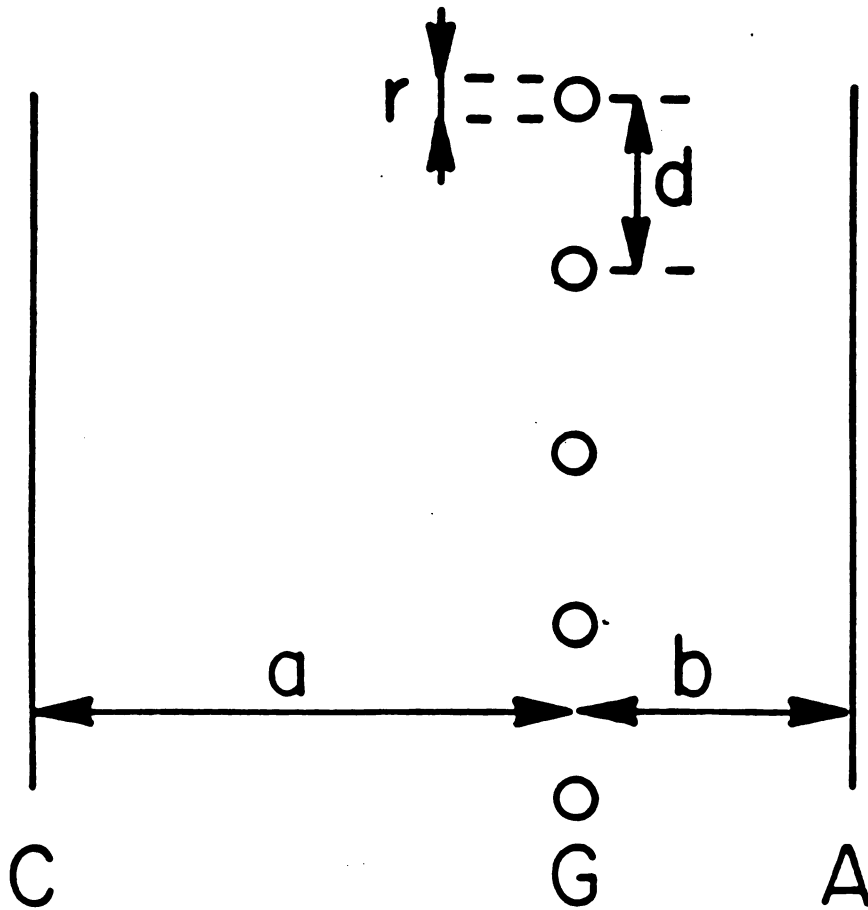


FIGURE II-3 Schematic view of the Frisch grid/anode geometry for the BCS.



MSU-84-588

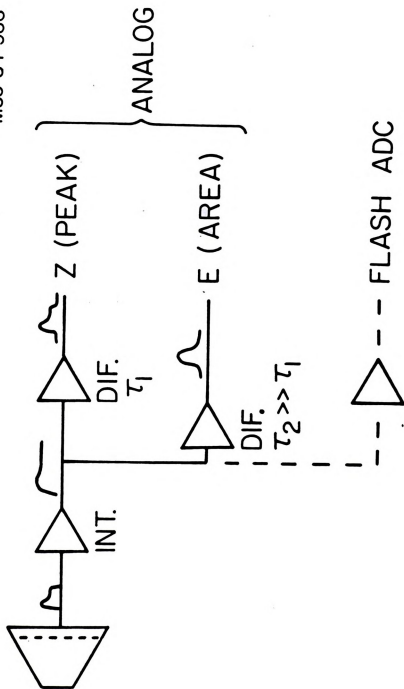


FIGURE II-4 Diagram for two different read out techniques for the BCS.



MSU-84-069

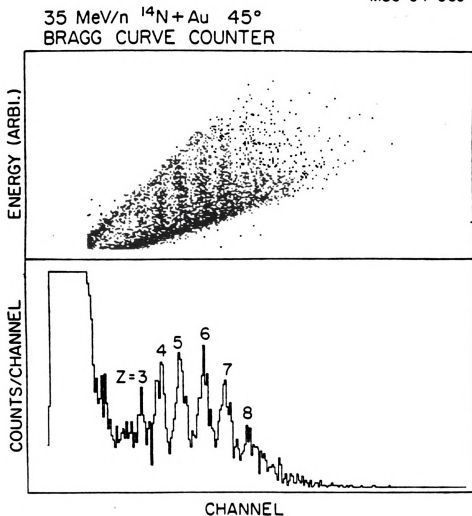


FIGURE II-5 Top: two-dimensional plot of Z (horizontal) Vs. E (vertical) for the reaction $^{14}\text{N} + ^{197}\text{Au}$ at 35 MeV/A. Bottom: projected Z spectrum for the same reaction.

plot of the charge Z (horizontal axis) versus E (vertical axis). The bottom part of Fig. II-5 shows the one-dimensional projection (Z -spectrum) of the same reaction. The individual charges of the particles stopped in the counter are clearly isolated. They show up as peaks in the one-dimensional Z spectrum on a background of particles that barely get into the detector (the lower line), and particles that punch through (the upper line). In actual data analysis energy cuts were used so that these "punch-in" and "punch-through" lines were not included in the energy spectra.

In Fig. II-6, results from the reaction $^{35}\text{Cl} + ^{58}\text{Ni}$ are presented. The beam of 230 MeV ^{35}Cl was provided by the tandem/linac of Argonne National Laboratory. In this case, charges up to $Z=17$ were resolved.

It sometimes appears that the horizontal Z lines are slightly curved. This is due to a non-perfect radial electric field in the pyramidal Bragg Curve Spectrometer. Also, the individual Z lines curve back near the "punch-through" line. As the particle starts to punch through, the peak energy loss information is not immediately cut off as the total integrated charge is reduced. Then, as the Bragg peak starts to punch through one obtains a peak signal that is still somewhat proportional to the charge of the particle and inversely proportional to the energy.

Despite these effects, the individual charges remain resolved as can be seen in Fig. II-7. The energy

MSU-84-068

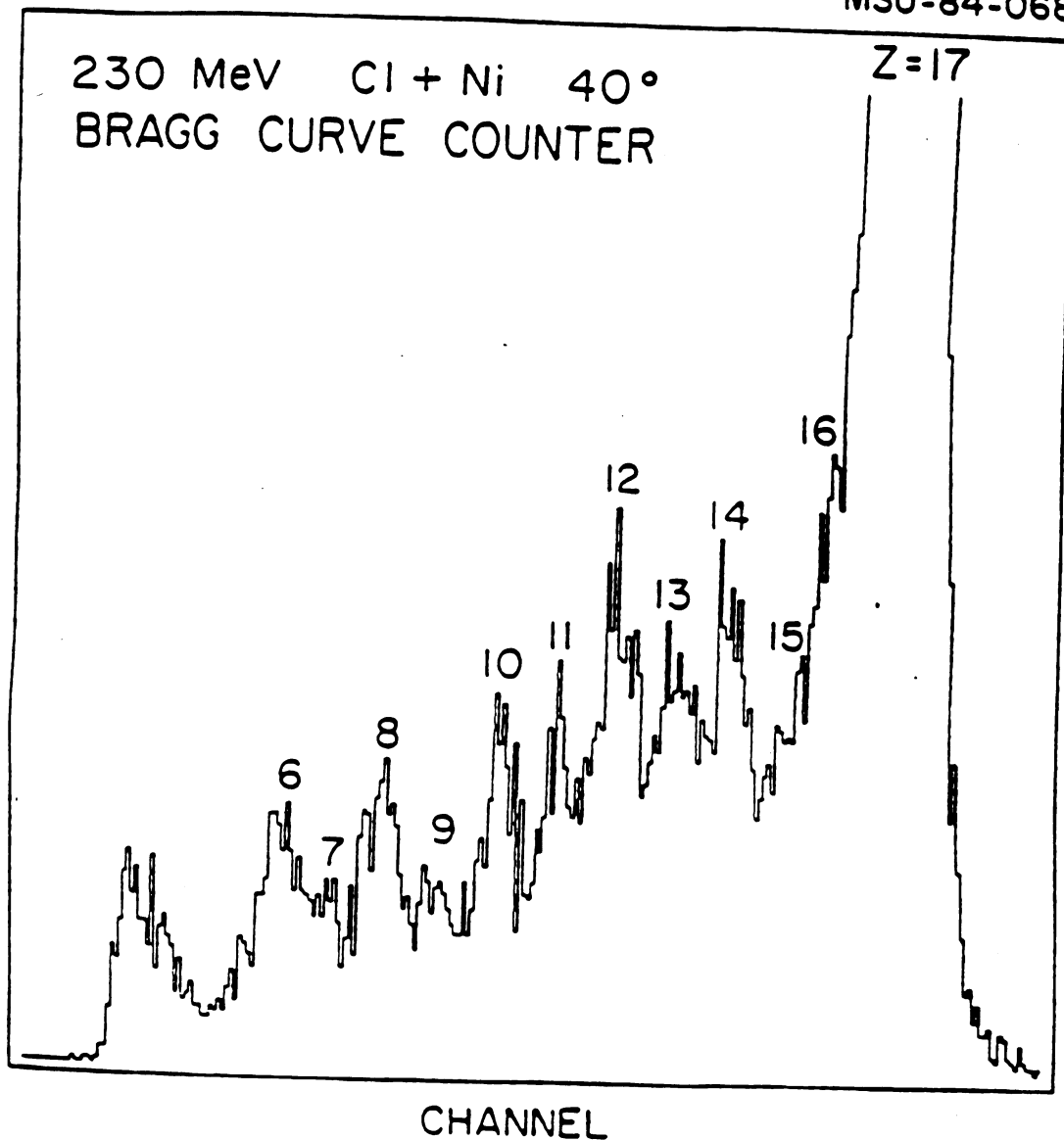


FIGURE II-6 Charge spectrum from the BCS for the reaction $^{35}\text{Cl} + ^{58}\text{Ni}$ at 230 MeV.



calibration for a 30 MeV/nucleon $^{12}\text{C} + ^{12}\text{C}$ experiment, as obtained from the punch through line, is shown in Fig. II-7.

The second method of reading out the BCS is by storing the entire current signal from the anode onto magnetic tape. This signal is digitized by a flash encoder that integrates the charge in 75 nsec time bins. A typical Bragg curve, measured with the flash ADC for the reaction $\text{Au}(^{14}\text{N},\text{X})$ at 35 MeV/nucleon is shown in Fig. II-8. The advantage of this method is the ability to playback the entire anode signal at some later time and analysis it "off-line" with different methods. All of the analysis of the BSC in this thesis has incorporated the first method.

The second subsystem of the Bragg Curve Detector is an array of six CaF_2 - plastic scintillator "phoswich" telescopes as seen in Fig. II-1, which sit directly behind the Bragg Curve Spectrometer and form the rear pressure window for the BCS. This construction ensures that there is not a dead layer between the BCS and the telescopes which are termed Bragg plastics (BP). Each of the six BP's represents a particle-identifying telescope with a ΔE and E detector using a slow and fast scintillator read out via one photomultiplier.

The ΔE counter is a 3 mm $\text{CaF}_2(\text{Eu})$ crystal with a characteristic decay time of 1 μsec for the emission of the scintillation light. The plastic scintillator used for the E counter is 15 cm thick BC412 which emits most of its light in 50 nsec and is capable of stopping a 150 MeV proton. The



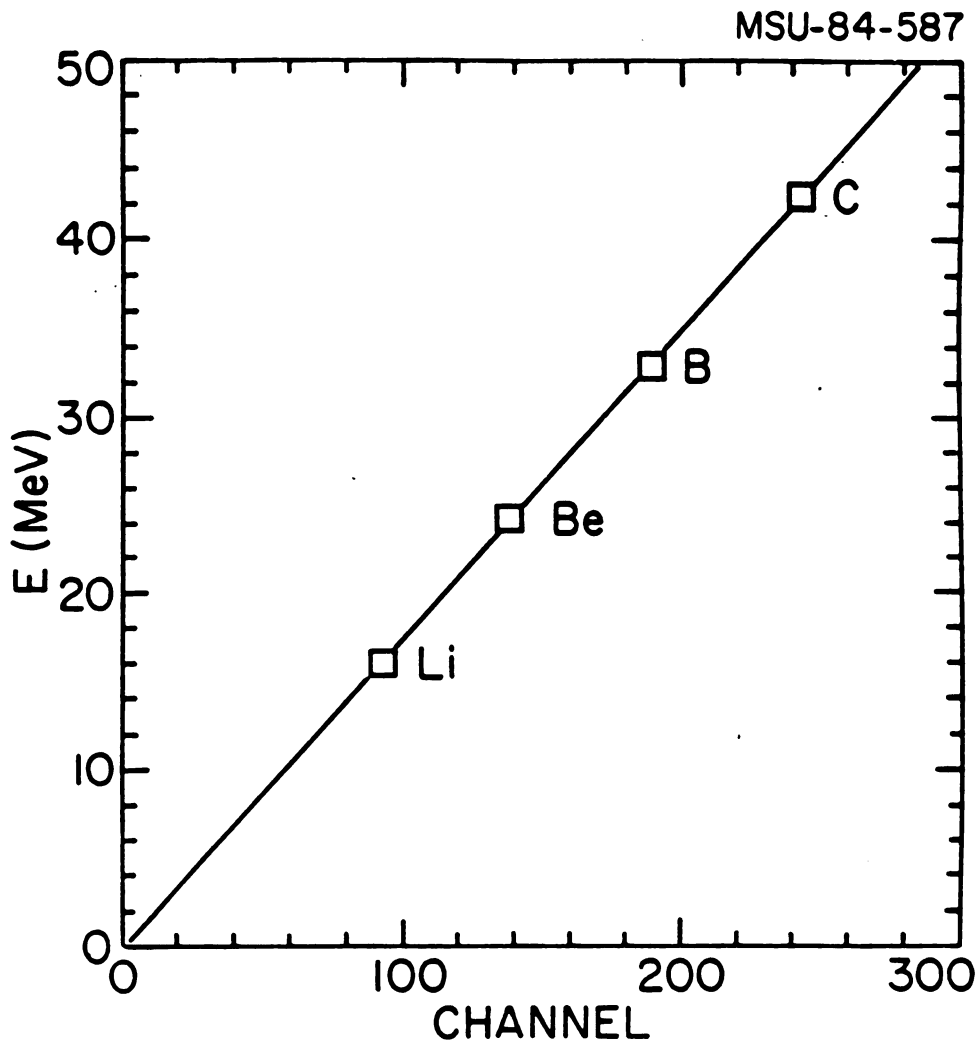


FIGURE II-7 Calibration plot for the BCS for 30 MeV/A C+C.



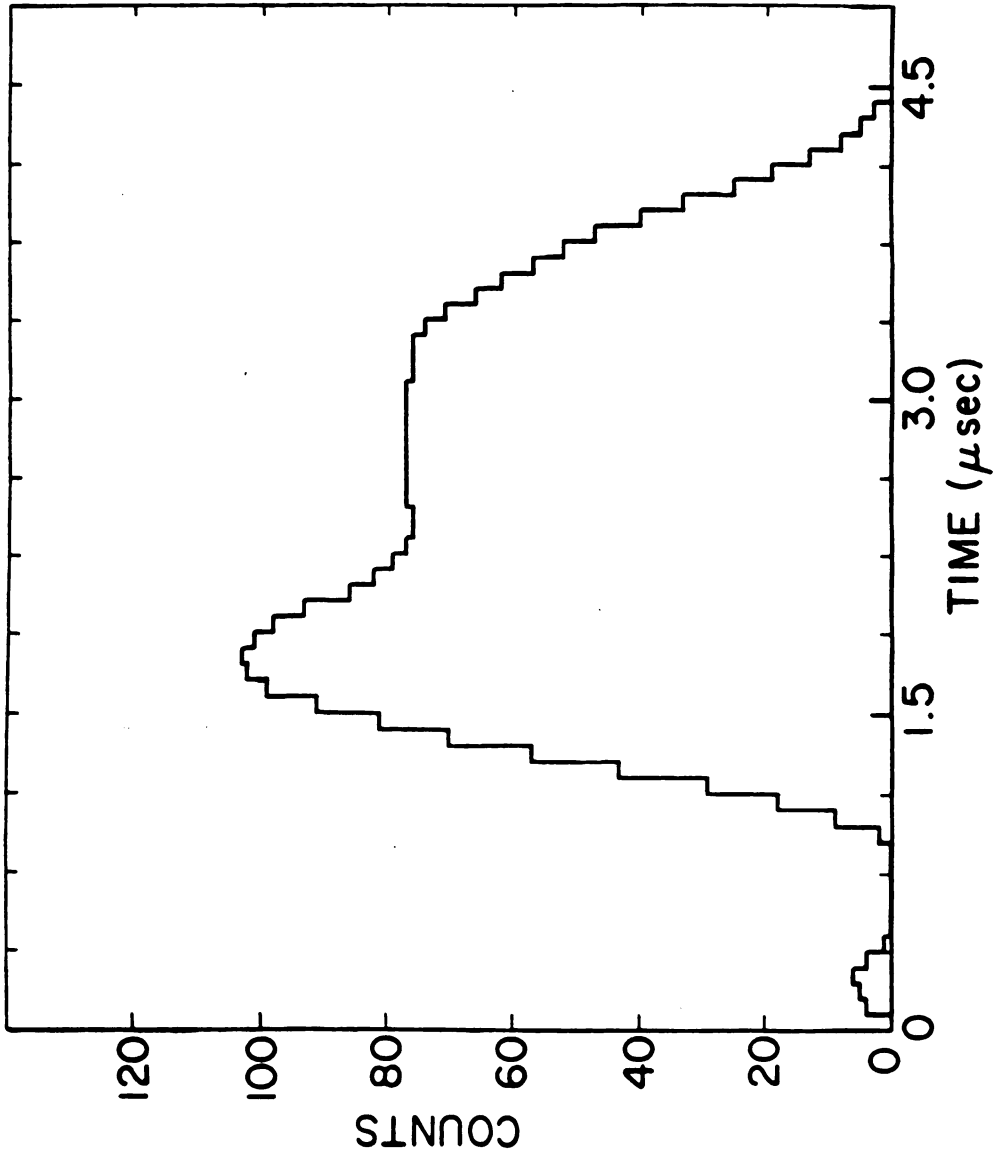


FIGURE II-8 "Snapshot" of the BCS, i.e. the digitized current output as measured with the flash encoder.



light of the CaF_2 is read out through the E counter (the E counter serves as a lightguide) and its light output is about 100 to 120% of anthracene. The light emission of the plastic scintillator is about 45% of the light output of anthracene where as it's more than 100 times faster than that of the CaF_2 so that 90% of the E signal is collected within 10 nsec. Integration of the photomultiplier output in a charge integrating ADC for the first 80 nsec gives most of the plastic scintillator signal. A separate integration in another charge integrating ADC over a period of 2 μsec delayed by 240 nsec relative to the beginning of the first integration gives the CaF_2 signal (Fig. II-9). There is a certain amount of each signal which is either lost or contained within the wrong integration due to the overlap of the two signals. This effect is fairly small and can be corrected offline. The read out of the ΔE -E module is done via a conically shaped lightguide made of lucite, which couples to a 2-inch, 10-stage photomultiplier tube (Amperex PM2202). The base containing the divider chains for the photomultiplier tube was an EMI active base design. The telescope particle identification capability is shown in Figure II-10 where p,d,t, ^3He , and ^4He are clearly separated.

The hexagonal shape of the Bragg Curve Detector system was developed to be a prototype subarray for a 4π detector [We 85]. The shape of the 4π detector is based on a thirty-two face truncated icosahedron containing 20 regular



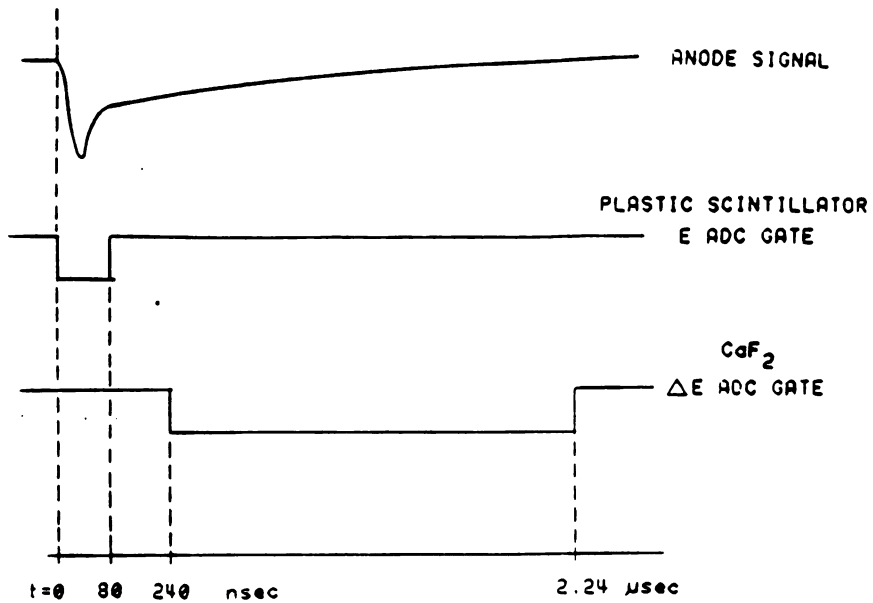
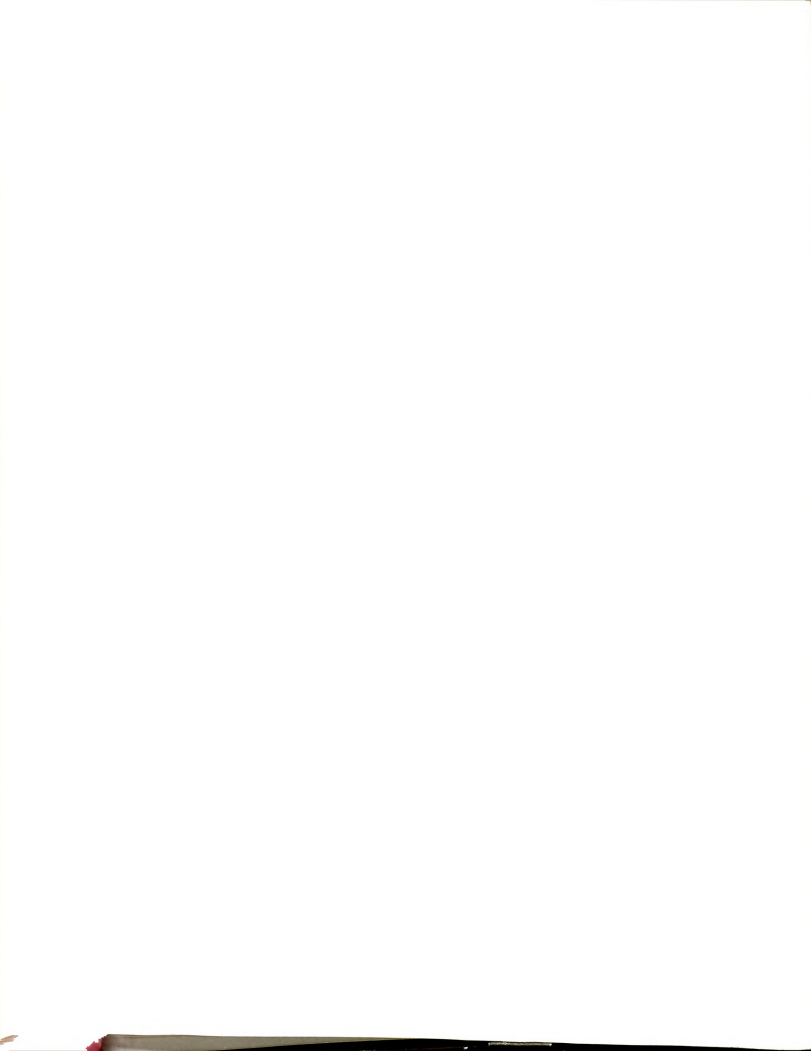


FIGURE II-9 Timing diagram for the scintillator array telescopes. The anode is a sum of the fast plastic scintillator component and the slow CaF₂ component.



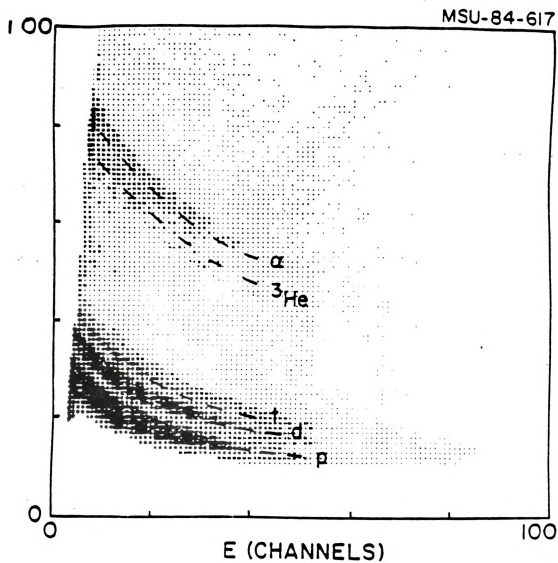


FIGURE II-10 Contour plot of the ΔE (vertical) Vs. E (horizontal) for a CaF_2 /plastic scintillator telescope in the BCS.



hexagonal faces and 12 regular pentagonal faces (a "soccer ball" geometry). In addition, each subarray will include a low pressure Multi-Wire Proportional Counter (MWPC) for fission fragments, which will be in front of the Bragg Curve Spectrometer.

Both the CaF_2 and the plastic scintillator were machined at MSU. Because of its low melting point and tendency to craze near regions of high temperatures, the plastic scintillator was machined with great care. No more than 10 mils of material per cut were taken off and it was cooled with a continuous flow of water soluble oil. The scintillator was then sanded with a fine grade waterproof polishing paper immersed in water and finally polished with optical polishing alumina. The CaF_2 elements were machined from 12.5 cm diameter by 3 mm thick disks of $\text{CaF}_2(\text{Eu})$. Because of the great stress in these large but fairly thin disks, a number of techniques were used to cut them into triangular shapes. The only technique that was able to cut the crystals without fracturing them, was with a vertical table sander cooled with a continuous stream of water and set on a very slow speed. This technique alleviated the stress slowly from the end so that the crystal would not crack. A clear lucite lightpipe was also machined to match the plastic scintillator to the photomultiplier tube.

In order to minimize the space between each telescope and not allow light to cross from one scintillator to the next ("cross talk"), it was necessary to assembled

reflective TiO_2 with epoxy. All six plastic scintillators were combined in this manner. The CaF_2 , lightpipes, and photomultiplier tubes for each telescope were attached with optical epoxy. The entire array of six telescopes was then epoxied onto the rear of the Bragg Curve Spectrometer. The lightpipes were painted with a TiO_2 water based reflective paint [Bi 67].

B. HIT DETECTOR

This detection system is also composed of two subsystems; an array of seven light-particle "Phoswich" telescopes capable of determining the energy and identity of light isotopes (Fig. II-11), and a multiwire proportional counter, which gives more precise position information on these same light particles, positioned in front of the telescope array. The plastic scintillator is 17 cm thick and the CaF_2 is 2 mm thick. The telescopes were designed to close pack in a spherical geometry as six tapered hexagonal shaped detectors surrounding a seventh tapered hexagonal shaped detector. Figure II-12 shows a ΔE -E plot for an HP telescope.

An important consideration for both detector systems was the low energy cutoff imposed by the relatively thick CaF_2 front element. Calculated cutoffs are given in Table II-1 for the hydrogen and helium isotopes for CaF_2 thicknesses of 2 and 3 mm. The cutoffs imposed by these



MSUX-82-366

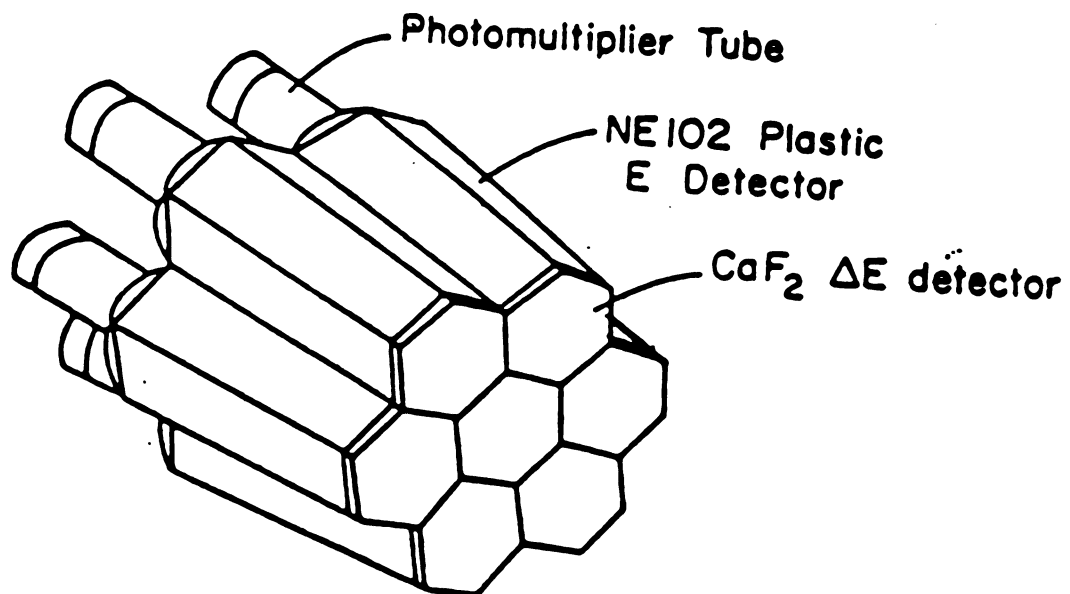


FIGURE II-11

Seven telescope scintillator array used in the Hit detector, i.e. the Hit plastics (HP).

The first part of the document discusses the importance of maintaining accurate records of all transactions. It emphasizes that every entry should be supported by a valid receipt or invoice. This not only helps in tracking expenses but also ensures compliance with tax regulations.

In the second section, the author provides a detailed breakdown of the company's revenue streams. This includes sales from various product lines and services. The analysis shows that while some areas are performing well, others need more attention and investment.

The third section focuses on the company's financial health. It includes a summary of the balance sheet, income statement, and cash flow statement. The author notes that the company's overall financial position is stable, but there are some areas where costs can be reduced to improve profitability.

Finally, the document concludes with a series of recommendations for the future. These include diversifying the product portfolio, strengthening customer relationships, and exploring new market opportunities. The author expresses confidence in the company's long-term success if these strategies are implemented effectively.

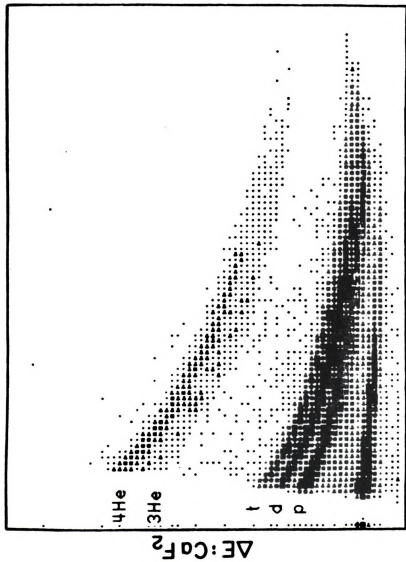


FIGURE II-12 Contour plot of the ΔE (vertical)
 vs. E (horizontal) for a CaF_2 /
 plastic scintillator telescope in
 the Hit detector.

TABLE II-1

CALCIUM FLUORIDE PUNCH THROUGH ENERGIES (MeV/n)

<u>THICKNESS</u>	<u>2 mm</u>	<u>3 mm</u>
Proton	21.5	27.0
Deuteron	14.5	18.2
Triton	11.5	14.5
³ Helium	25.2	31.5
⁴ Helium	21.5	27.0



detector thicknesses were considered to be sufficiently low for the beam energies to be used.

CHAPTER III

EXPERIMENTAL

The experiment was done at the National Superconducting Cyclotron Laboratory (NSCL) at Michigan State University in the 60 inch scattering chamber. Beams of 15 and 30 MeV/nucleon ^{12}C were used on both a gold and a carbon target. The targets used were all self-supporting and consisted of 2.45 mg/cm^2 Au and $201 \text{ } \mu\text{g/cm}^2$ C.

A. EXPERIMENTAL SETUP

The experimental setup, as seen in Fig. III-1, consisted of two plastic scintillator arrays, Hit plastics (HP) and Bragg plastics (BP), for light particle detection (see Chapter II). In front of the Bragg plastics there was a Bragg Curve Spectrometer (BCS) for slow moving Target-Like Fragments. The plastic scintillator arrays were positioned in the chamber with the bottom two telescopes for both arrays at the beam height and each were moved during the experiment. A high energy fragment detector was placed at a fixed angle of 15 degrees from the beam axis as a projectile-like fragment detector (PLF) consisting of a two element silicon stack. A $400 \text{ } \mu\text{m}$ Si detector was used for the ΔE and a 5 mm for the E detector. The positions and solid angles for the detectors are given in Table III-1. The negative angles of the Hit detector indicates that it

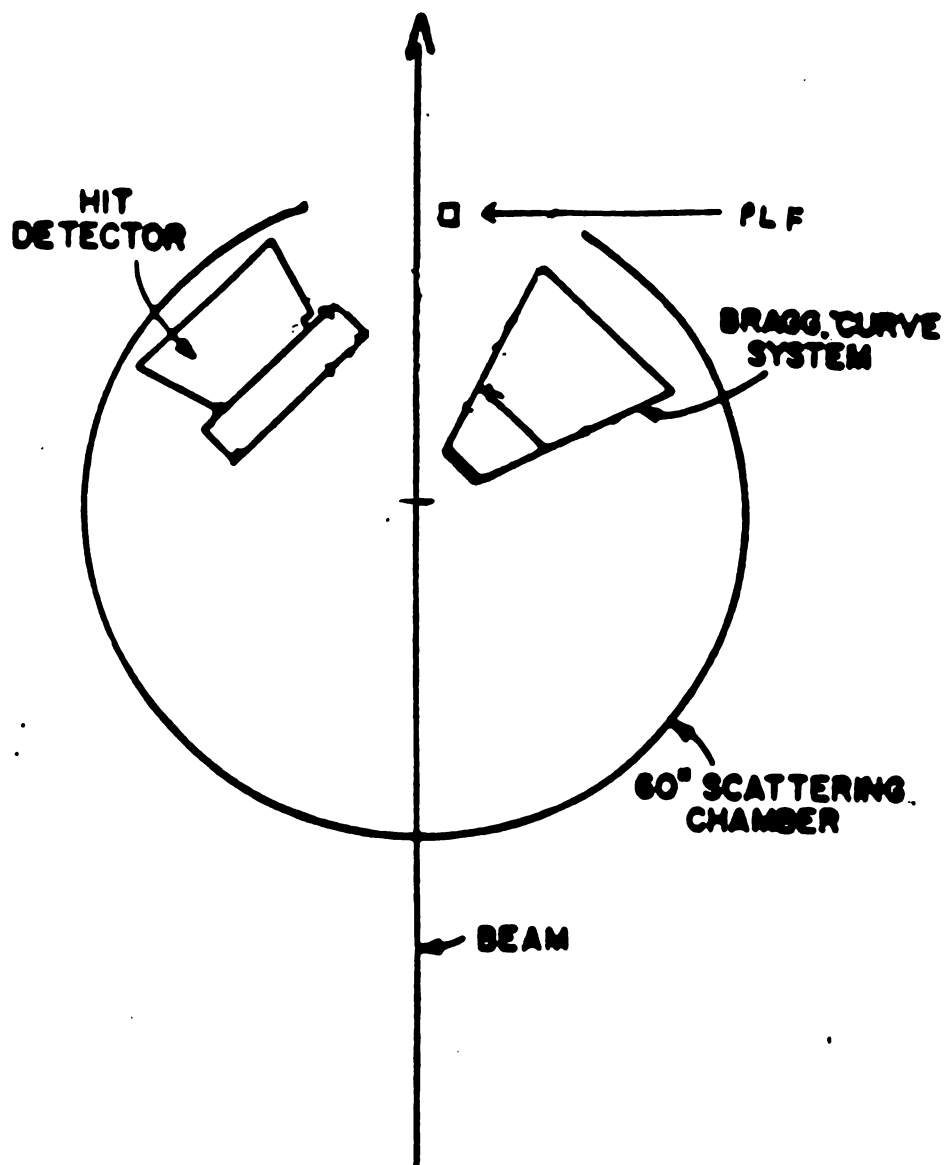


FIGURE III-1 Chamber setup during the experiment.

TABLE III-1
DETECTOR ANGLES

DETECTOR	THETA (DEG)	SOLID ANGLE (MSR)
PLF	15.0	7.8
HP ^(a)	-45.0, -90.0 ^(b)	14.9/element
BCS ^(a)	45.0, 90.0 ^(b)	55.4/element

(a) Angles are for the central element of the array.

(b) The arrays for the C target were at 45° only.

was on the opposite side of the beam from the Bragg Curve System and PLF detector.

Both coincidence and scaled down singles events were taken. Coincidence requirements consisted of any two or more plastics from either array or any one or more plastic scintillators in coincidence with a trigger detector. Both the BCS and the PLF detector served as a trigger detector. The electronics diagram is shown in Fig. III-2.

The data acquisition system at NSCL is based on a multiprocessor, multitasking system. A DEC VAX 750 minicomputer with an LSI-11/23 as a front end data capture device was used [Au 83]. The software in both of these computers is multitasking, the LSI-11 not only takes event data, but has programs which are responsible for the run control, accumulation, and the live display of a number of scalers. The VAX software includes programs which display the accumulated histograms as well as programs which are responsible for binning the raw event data.

A Kinetic Systems CAMAC serial highway connects the VAX to the data acquisition hardware. This system consists of an LSI-11/23 which is resident in a CAMAC crate, and an assortment of scalers, analog to digital converters (ADC), time to digital converters (TDC), and charge integration to digital converters (QDC). The spectra accumulated on line are displayed on an Advanced Electronics Design (AED) model 512 color graphics terminal. This terminal is capable of displaying monochrome one dimensional histograms and color

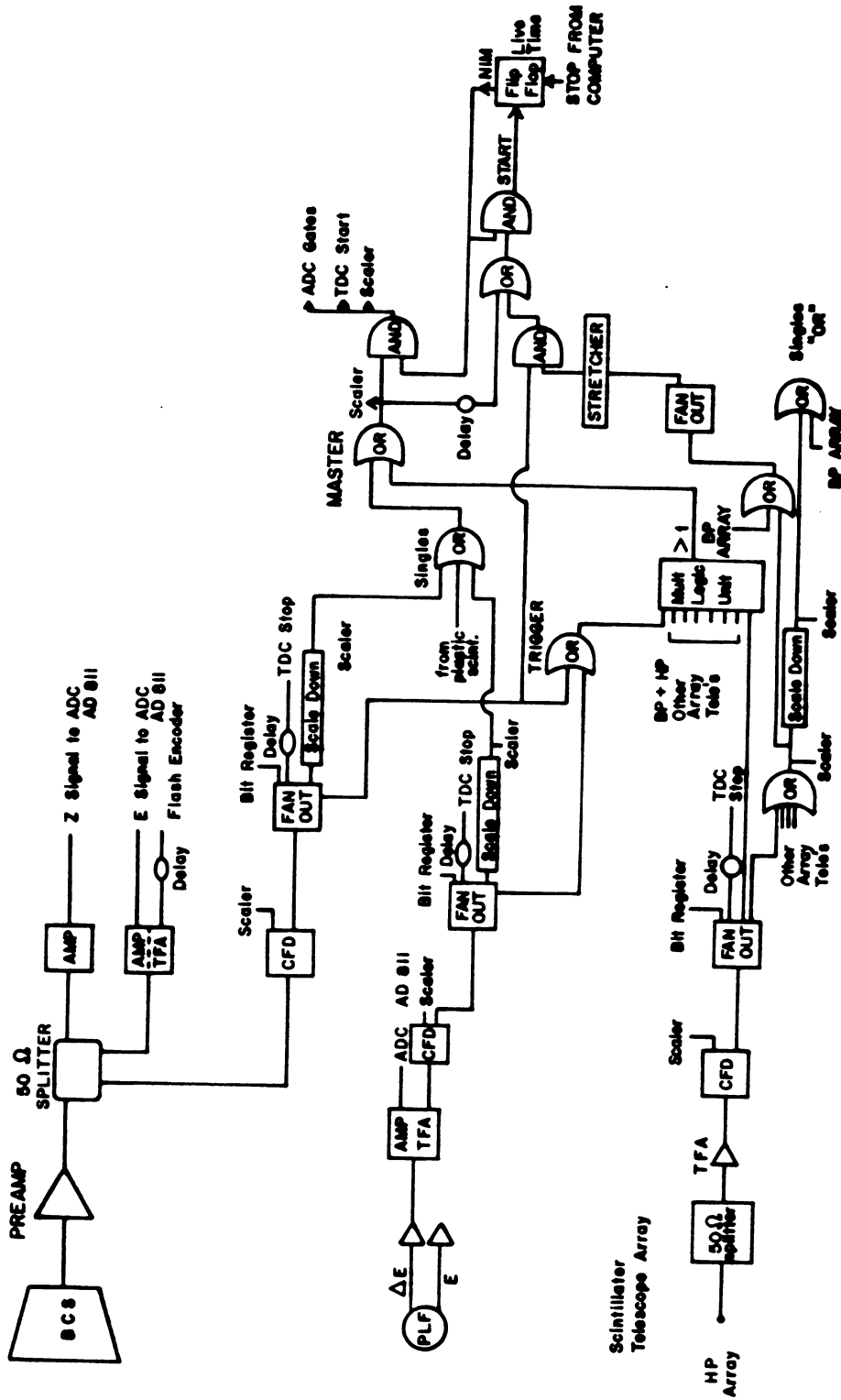


FIGURE III-2 Electronics schematic for the experiment.

The first part of the document discusses the importance of maintaining accurate records of all transactions. It emphasizes that every entry, no matter how small, should be recorded to ensure the integrity of the financial statements. This includes not only sales and purchases but also expenses and income. The document also highlights the need for regular reconciliation of bank statements and the company's records to identify any discrepancies early on.

In addition, the document provides a detailed breakdown of the accounting cycle, from identifying the accounting entity to preparing financial statements. It explains how each step contributes to the overall accuracy and reliability of the financial data. The document also includes a section on the classification of assets and liabilities, providing examples and explanations for each category.

The second part of the document focuses on the practical application of accounting principles. It includes a series of exercises designed to help students understand how to record transactions in the general ledger and how to prepare a trial balance. These exercises cover a wide range of scenarios, from simple sales and purchases to more complex transactions involving multiple accounts and adjustments.

Finally, the document concludes with a summary of the key concepts covered in the course. It reiterates the importance of accuracy, consistency, and transparency in accounting. It also provides a list of resources for further study and a contact information for the instructor.

density plots of two dimensional spectra with 512×512 pixel resolution. The VAX is used for the actual on line analysis and event taping of data buffers sent to it by the LSI-11.

The 15 and 30 MeV/nucleon ^{12}C beam currents were monitored in a shielded faraday cup placed approximately two meters beyond the exit port of the scattering chamber. The current was integrated in a BIC Current Integrator and was recorded in the computer using a CAMAC scaler module. The beam intensity varied from 1.5 particle namps (9×10^9 particles per second) to 10 particle namps (6×10^{10} particles per second).

B. DATA REDUCTION AND ANALYSIS

The data taken in the experiment was recorded on magnetic tape in event mode. All runs with the same detector setting were summed together. Since this was a coincidence experiment, it was necessary to optimize the statistics for each type of coincidence event, therefore all of the Hit plastics were summed together as if it were single detector. The same was done for the Bragg plastics. In addition, the singles events were scaled down so that better statistics could be obtained for the coincidence events. The absolute normalization was based on the integrated beam current in the faraday cup.

The event data was later played backed onto the computer and sorted by particle type using software gates which had been created with the aid of a two dimensional

color display from the AED terminal. The sorted data were then calibrated, binned into histograms, and then normalized to obtain the final absolute normalized spectra. The data was corrected for several experimental effects including reaction loss, scatter out and computer dead time.

Energy calibrations for the scintillator array telescopes were based on both direct beam calibration and fits to previously calibrated data. A beam of 25 MeV/nucleon alpha particles was used to calibrate the detectors. However, since the minimum energy for an alpha particle which penetrates the CaF_2 in the Hit and Bragg plastics are 22 and 27 MeV/nucleon respectively, and since the calibration for protons and alphas are not the same, this calibration was found to be inadequate. By using a least squares fitting routine to previously calibrated 30 MeV/nucleon C+Au data [Ha 84], a calibration was obtained for each telescope. Values of the reduced χ^2 for the fits were typically less than 5 and a comparison to the beam calibration indicated that a satisfactory calibration was obtained.

The energy calibration for the silicon PLF detectors was done by injecting a known amount of charge by means of a chopper pulser in the input stage of the detector preamplifiers and using the measured values of the ionization energy of silicon, $\epsilon=3.67$ MeV/ion pair [Pe 68].

C. Reaction Loss Correction



The plastic scintillator telescope spectra were corrected for reaction losses of the light particles stopping in the detectors. Nuclear interactions, as compared to atomic electron interactions, tend to broaden the full energy peak on the low energy side. Inelastic collisions in the detector typically have neutrons, gammas, and alphas as the reaction products. The light output in the detector is less for these reaction products than it would have been for the original particles because of the nonlinearity of the response of scintillation materials to more highly ionizing particles and production of uncharged particles. These effects result in the loss of the particle from the full energy peak. The particles then no longer fall into particle identification lines and appear as a smooth background in the Fig. II-10.

The fraction of reaction loss for protons as a function of proton energy was taken from Measday and Richard-Serre [Me 69]. In order to make the corrections, the detector was divided up into slices, and the particle energy of each slice calculated from the entrance energy using energy-range tables generated by the code DONNA. The reaction cross section was then calculated by parameterization obtained by fitting a form of the standard reaction cross section

$$\sigma_R = \pi R^2 (1 - V_c/E) (1 - (\kappa/E)^\lambda) \quad (\text{III-1})$$

to measured cross sections tabulated by Measday and Richard-Serre [Me 69]. Where the nuclear interaction radius R is given by

$$R=r_0(A_1^{1/3}+A_2^{1/3}-1) \quad (\text{fm}), \quad (\text{III-2})$$

where $r_0=1.2$ fm, the coulomb potential at the interaction radius V_c is,

$$V_c=1.44(Z_1Z_2/R) \quad (\text{MeV}), \quad (\text{III-3})$$

and κ and λ are the adjustable parameters. An adjustable overall normalization factor was also included in the fit. The reaction cross section for each slice was then calculated and the reaction probability of a particle was given by the integration over the slices

$$f=1-\exp(-\sum_i n_i \sigma_i), \quad (\text{III-4})$$

where n_i is the number of atoms/cm² in the i^{th} cell and σ_i is the calculated cross section in each cell. The parameterized fit was for protons in scintillator. The values for κ and λ were $\kappa=20$ MeV and $\lambda=1.2$, with the normalization constants being 1.45 for plastic scintillator and 2.7 for CaF₂. The reaction probability was calculated

for each energy bin in the spectrum of each particle, and the cross section corrected by the factor $1/(1-f)$.

D. Scattering Out Correction

The need for large area detectors in multi-particle coincidence experiments lead to the construction of high density plastic scintillator arrays in which the individual telescopes were not collimated. A scattering out correction was necessary because particles incident near the edge of a plastic scintillator detector were likely to scatter out and not be identified as valid events. Particles scattering into the detectors from neighboring telescopes would not be identified as valid events since there would be no CaF_2 (ΔE) signal for such events. A Monte Carlo calculation was developed to simulate the scattering out effects of transverse straggling of the particles. First the code calculated the total range of a given energy particle in the plastic scintillator and then calculated the transverse straggling based on a gaussian distribution with a root mean square projected angle given by the formula [Pa 84]

$$\theta_{\text{proj}} = \frac{Z}{A} \frac{14(t+m_a)}{t(t+2m_0)} (L/L_R)^{1/2} \left[1 + \frac{1}{9} \text{Log}_{10}(L/L_R) \right] \left[1 + \frac{Am_a}{(t+m_0)A_s} \right]$$

(III-5)

where

t = Incident kinetic energy per nucleon,

$m_0=931.5,$

L =Thickness of material traversed (g/cm^2),

L_R =Radiation length,

A, A_s =Mass number of particle, medium,

Z =Atomic number of particle.

The radiation length for different materials are tabulated in the literature [Pa 84]. For those materials that do not have measured radiation lengths, they were calculated based on a formulation given by Tsani [Ts 74]. The entrance point for each particle and each energy were found using a Monte Carlo technique in which the geometry of the front face of the telescope was treated with equal probability. The transverse scattering in the CaF_2 was calculated first and the particles new trajectory was then used for the calculation in the plastic scintillator. The final calculated trajectory of the particle was checked against the actual geometry of the detector to ascertain if the particle would have scattered out. The fraction scattered out, R , was calculated as the number of simulated events for which the particle scattered out divided by the total number of events. The scatter out correction factor for each bin of the energy spectra was divided by $(1-R)$.

CHAPTER IV

RESULTS

In this chapter, light particle ($Z=1,2$) spectra are presented as inclusive and coincidence cross sections. The coincidence spectra are in coincidence with intermediate mass fragments ($3 \leq Z \leq 6$) in the Bragg Curve Spectrometer (BCS) at 45° and the Projectile-Like Fragment (PLF) detector at 15° . The requirement that the spectra have sufficient statistics dictated the need to sum all of the plastic scintillators in each of the arrays, as if each of the arrays were one detector. The inclusive spectra for the trigger (PLF and BCS) detectors are also shown. The error bars shown in each of the spectra are statistical. Positive angles for an array indicates that it is on the same side of the reaction plane as the trigger particle, negative angles imply the opposite side.

A. 15 and 30 MeV/nucleon $^{12}\text{C}+\text{Au},\text{C}$ Inclusive Spectra

1. Light Particle Inclusive Spectra

Figures IV-1 and IV-2 show the double differential cross sections of the hydrogen and helium isotopes for 15 MeV/nucleon C+Au and C targets, respectively, and figures IV-3 and IV-4 show the double differential cross sections for the 30 MeV/nucleon C+Au and C targets, respectively. The 30 MeV/nucleon C+Au spectra consist of angle

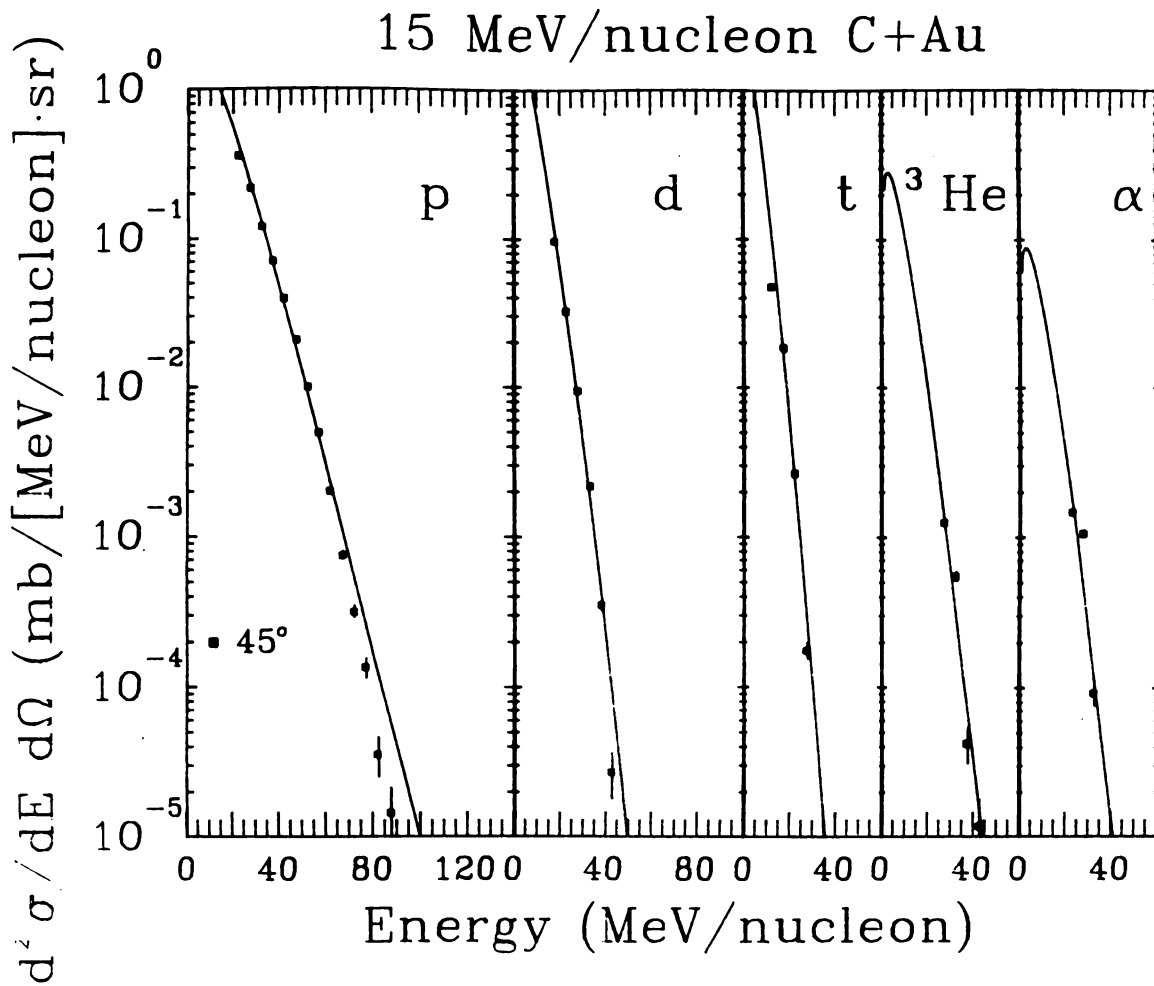


FIGURE IV-1

Light particle inclusive energy spectra
for 15 MeV/A C+Au.



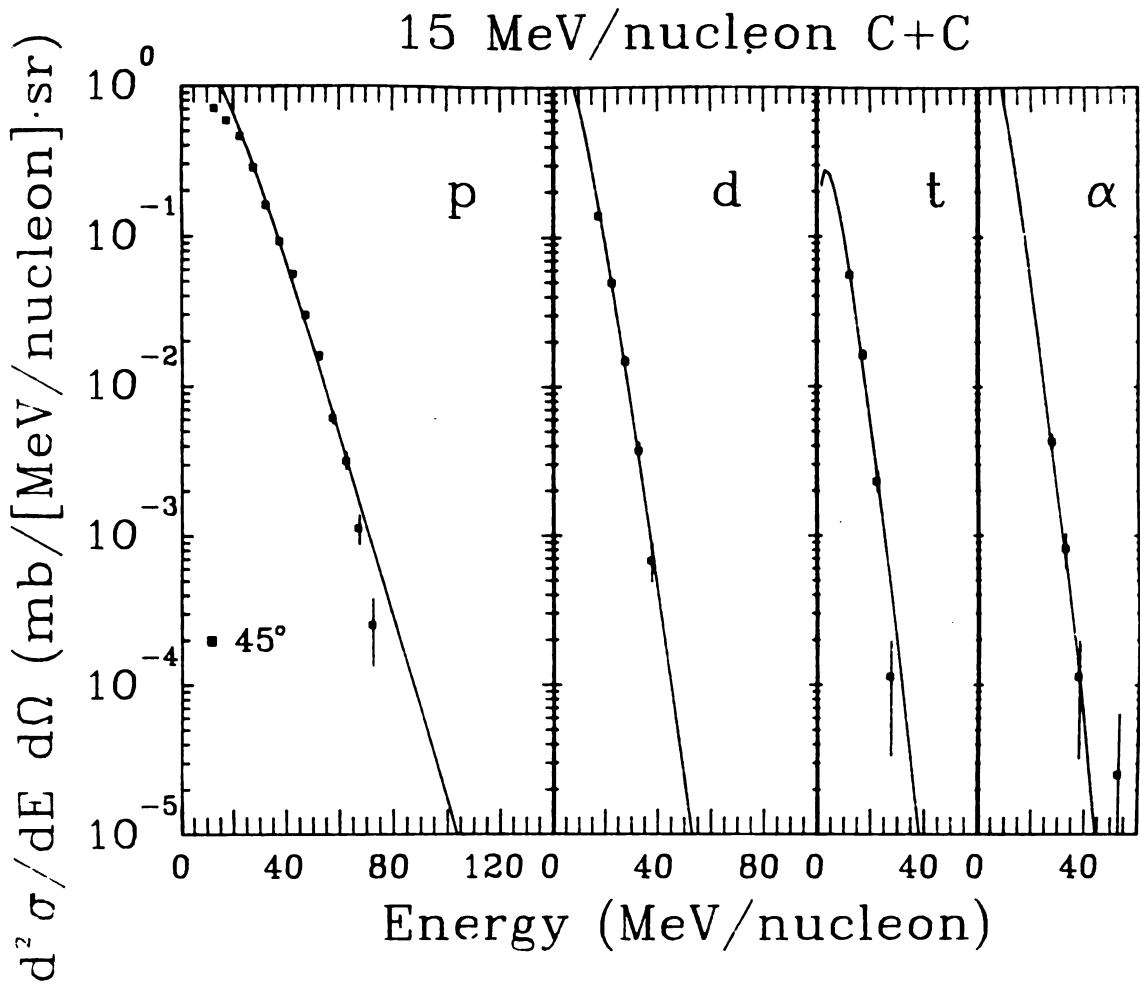


FIGURE IV-2 Light particle inclusive energy spectra for 15 MeV/A C+C.



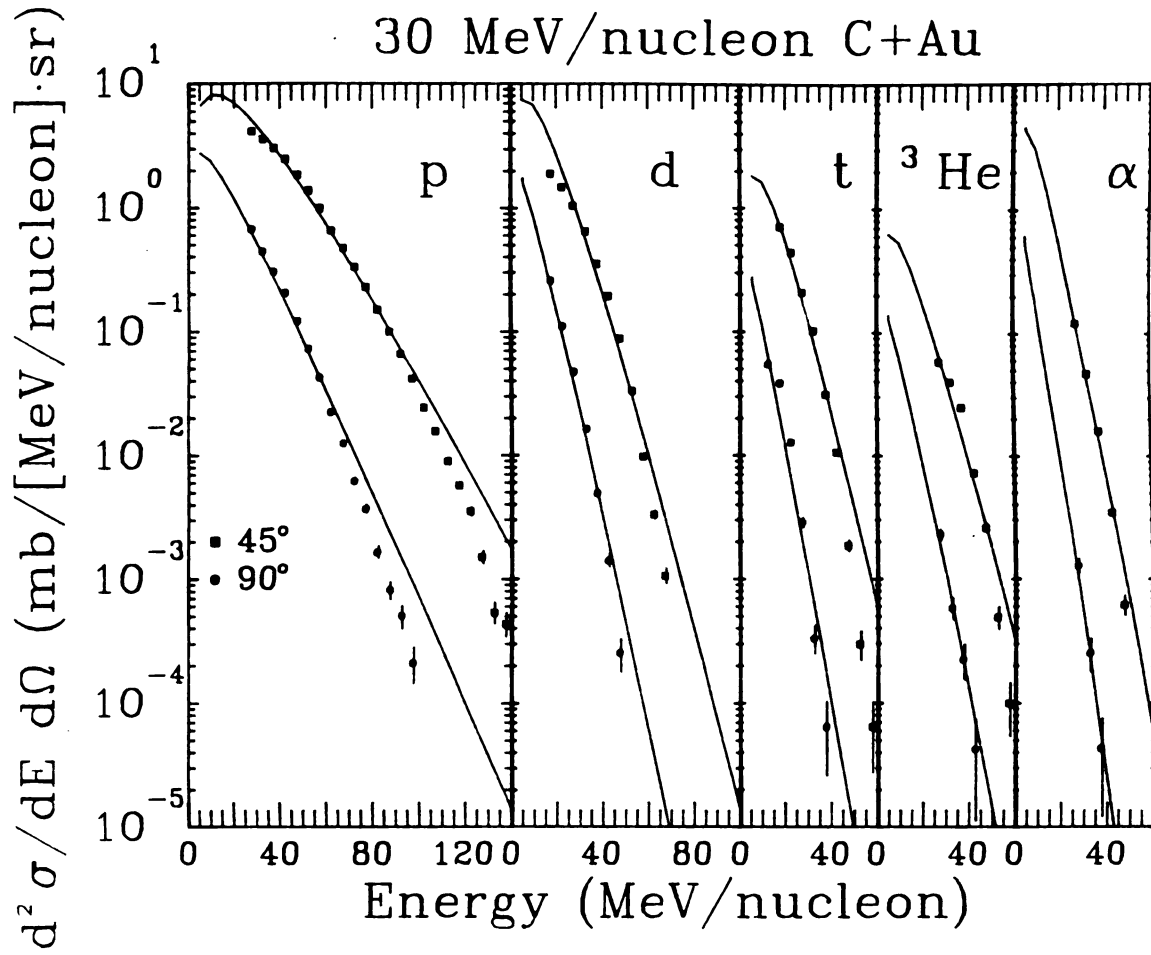


FIGURE IV-3 Light particle inclusive energy spectra
for 30 MeV/A C+Au.



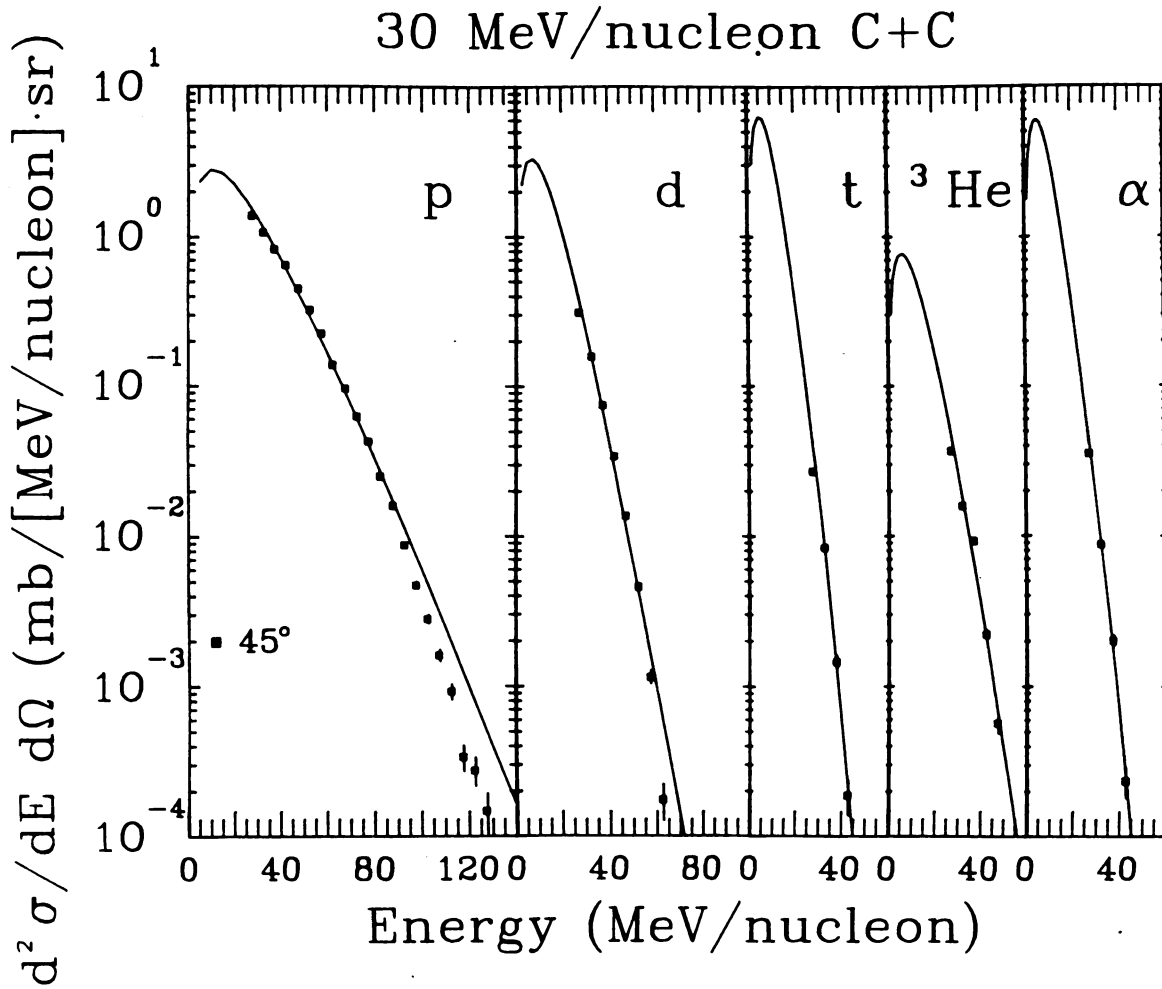


FIGURE IV-4

Light particle inclusive energy spectra
for 30 MeV/A C+C.



measurements of 45 and 90° in the laboratory. The solid curves in the figures correspond to moving source fits. All of the inclusive spectra are smooth and similar in shape and were fit well with the moving source parameterization. The C+C data were fit assuming the velocity of the source was the center of mass velocity.

2. Moving Source Parameterization

The light particles emitted can be parameterized by assuming they come from a single source with a Maxwellian energy distribution observed in a moving frame. This source emits particles isotropically in its rest frame which is moving at approximately half the beam velocity. The light particle energy spectra from the plastic scintillator arrays are fit by a single moving source parameterization. Heavy ion reactions have been described as having three distinct regions from which particles are emitted. This idea is known as the participant-spectator picture of nuclear collisions [We 76, Go 78, Aw 81]. The participant region is described as the overlap region between the projectile and target consisting of a highly excited system of nucleons and light nuclei, whereas the spectator region is described as the cold remnants of the target and projectile that did not overlap. The single moving source parameterization refers to a fit of the energy spectra taking into account only the participant region emission of light particles.

In order to isolate the participant region or intermediate velocity source in the energy spectra, it is necessary to exclude those parts of the spectra that correspond to the spectator region, that is the projectile and target velocity sources. The projectile source is usually associated with fragments at the beam velocity centered around 0° . Because the center of the most forward angle light particle detector array is at 45° , we are not sensitive to the PLF's. A target velocity source due to target fragmentation is usually associated with low energy particles distributed almost isotropically in the laboratory frame. A low energy cut off of about 25 MeV/nucleon eliminates most of the target velocity source, although there are certainly still contributions from the spectator region in the energy spectra. A parameterization using three moving sources have been attempted for relativistic heavy ion reactions [Ja 83]. It should be noted that the participant region for the present energies is not always thought of as a separate non-interacting entity from the target and projectile, but instead emits particles while still very close to the spectator regions [Bo 84]. However, we still apply the moving source parameterization as convenient method of extracting information from the light particle spectra.

The moving source parameterization is a useful tool for comparing large volumes of data in which the data can be condensed into just three parameters (described below) which

were fit to all the data. The idea of a thermalized region emitting particles, has had great success in describing data over a wide range of bombarding energies and systems [Ba 75, Am 75, So 75, We 76, Da 81, We 82]. Therefore a parameterization based on such a formulation is useful in comparing various sets of data and seeking evidence for thermalization.

The energy spectra is fitted to a relativistic Maxwell-Boltzmann energy distribution which is isotropic in the rest frame of the source. The distribution is given by

$$\frac{d^2\sigma}{p^2 dp d\Omega} = \frac{\sigma}{4\pi m^3} \frac{\exp(-E/\tau)}{2(\tau/m)^2 K_1(m/\tau) + (\tau/m) K_0(m/\tau)} \quad (\text{IV-1})$$

where p and E are the momentum and total energy, respectively, of a particle in the source rest frame. K_0 and K_1 are MacDonalld functions, also known as modified Bessel functions of the second kind. The particle mass is given by m , σ is the energy-integrated cross section, and τ is the source temperature. The distribution is assumed to be isotropic in a frame moving with the velocity, β , in the laboratory frame. The double differential cross sections are transformed into the laboratory frame using

$$\frac{d^2\sigma}{dE d\Omega} = p E' \frac{d^2\sigma}{p'^2 dp' d\Omega'} \quad , \quad (\text{IV-2})$$

where

$$E' = \gamma (E - \beta pc \cos \theta_{lab}) , \quad (IV-3)$$

and

$$\gamma = 1/(1-\beta^2)^{1/2} . \quad (IV-4)$$

The primed quantities refer to the source frame and the unprimed quantities refer to the laboratory frame. The moving source spectra are fit to the data using a least squares fit with three free parameters. The three fit parameters are σ , the total cross section, β , the velocity of the moving source (usually expressed as the ratio to the beam velocity), and τ , which is referred to as the temperature of the source. An energy shift correction due to the coulomb interaction between the observed fragment and the charged emitting region was applied to the data before fitting. The coulomb shifts used in the analysis of the Au target data were 10 and 18 MeV for Z=1 and 2, respectively. Shifts of 2 and 4 MeV were used for the C target data, for the Z=1 and 2, respectively. The inclusive spectra for p, d, t, ^3He , and ^4He are shown with their single moving source fits as solid lines in Figures IV-1-4. Since only the 30 MeV/nucleon C+Au has two angles (45 and 90°), it was the only one which could have the velocity parameter fitted. The C+C cases had the velocity fixed at the velocity of the center of mass. This is a reasonable assumption for the C+C data because both the nucleon-nucleon and system center of



mass are the same as well as the fireball center of mass. The values of the moving source parameters for the inclusive spectra are given in Tables IV-1 and IV-2.

3. Bragg Curve Spectrometer Inclusive Spectra

The Bragg Curve Spectrometer (BCS) is well suited for measuring the slow moving target-like fragments that stop in the detector. The inclusive fragment spectra ($3 \leq Z \leq 5$) for 30 MeV/nucleon C+C with the Bragg Curve Spectrometer trigger at 90 degrees are shown in Figure IV-5. The data have been plotted as double differential cross sections as a function of total fragment energy. As was mentioned in Chapter 2, only that part of the spectra that correspond to particles which stopped in the BCS are plotted and used as a trigger for coincidence events. The spectra show that the dynamic range of the stopped particles increases with the charge of the particle (Z) as one would expect from simple range-energy relations. The similarity of the shapes of the cross sections is an indication that a single reaction mechanism is responsible for the production of the various fragments.

4. Projectile-Like Fragment Inclusive Spectra

The inclusive spectra of the projectile-like fragment (PLF) trigger detector at 15 degrees are shown in Figures IV-6 and IV-7 for the Au and C targets, respectively, for the 15 MeV/nucleon data. Figures IV-8 and IV-9 show the Au and C data at 30 MeV/nucleon, respectively. The spectra



TABLE IV-1

MOVING SOURCE PARAMETERS 30 MeV/A C+Au,C (INCLUSIVE)

Particle	Temperature τ (MeV)	Cross section σ (mb)	Velocity β (c)
30 MeV/nucleon C+Au			
PROTON	9.7±0.2	1512.±30.	0.1247±0.0008
DEUTERON	9.0±0.3	1048.±130.	0.103±0.003
TRITON	11.8±0.4	471.±30.	0.109±0.002
HELIUM3	13.1±0.4	161.±120.	0.096±0.008
ALPHA	12.6±0.3	1176.±66.	0.092±0.008
30 MeV/nucleon C+C			
PROTON	8.5±0.2	671.±35.	
DEUTERON	8.1±0.3	314.±60.	
TRITON	7.1±0.3	99.±130.	
HELIUM3	12.1±0.5	68.±110.	
ALPHA	9.5±0.2	578.±20.	



TABLE IV-2

MOVING SOURCE PARAMETERS 15 MeV/A C+Au,C (INCLUSIVE)

Particle	Temperature	Cross section
	τ	σ
	(MeV)	(mb)

15 MeV/nucleon C+Au

PROTON.	6.0 \pm .2	155. \pm 23.
DEUTERON	5.3 \pm .3	88. \pm 35.
TRITON	5.5 \pm .3	47. \pm 51.
HELIUM3	6.6 \pm .5	14. \pm 67.
ALPHA	6.6 \pm .2	120. \pm 44.

15 MeV/nucleon C+C

PROTON	5.6 \pm .3	166. \pm 23.
DEUTERON	5.2 \pm .4	78. \pm 35.
TRITON	6.0 \pm .6	13. \pm 55.
ALPHA	8. \pm 2.1	97. \pm 120.



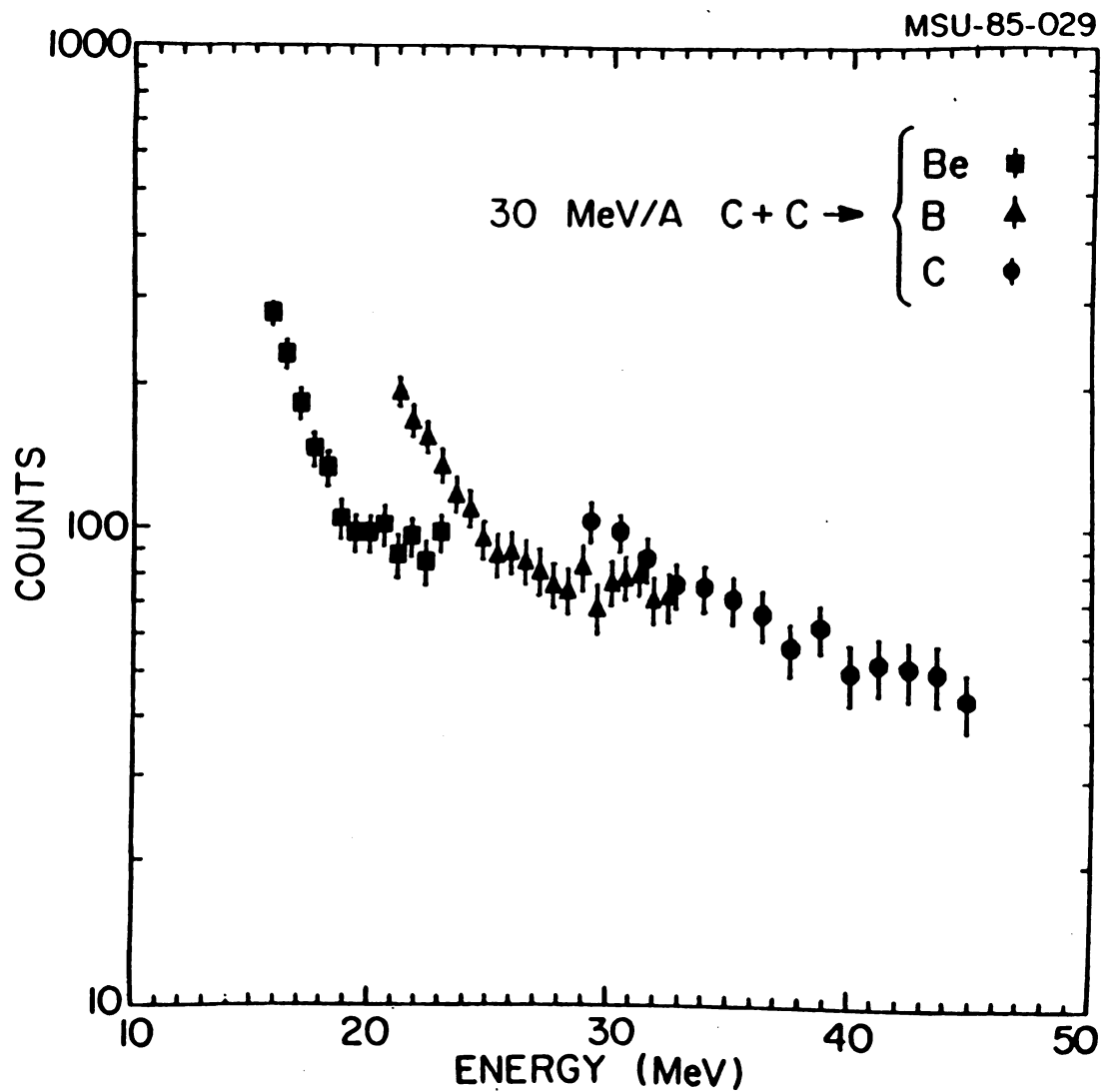


FIGURE IV-5 Inclusive energy spectra for Be, B and C from the 30 MeV/A C+C reaction, as measured with the BCS.

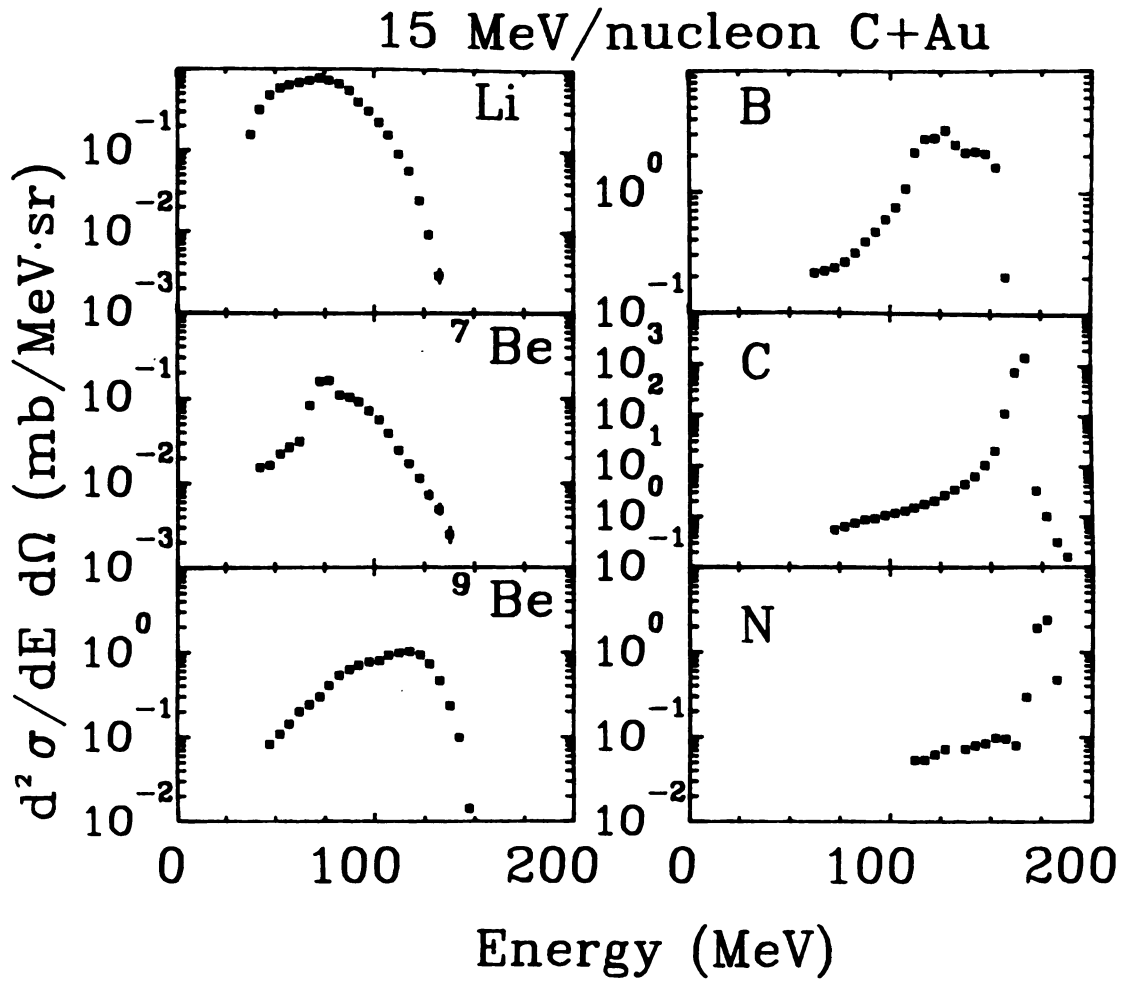


FIGURE IV-6

Projectile-like fragment inclusive energy spectra for the PLF detector at 15° for 15 MeV/A C+Au.

15 MeV/nucleon C+C

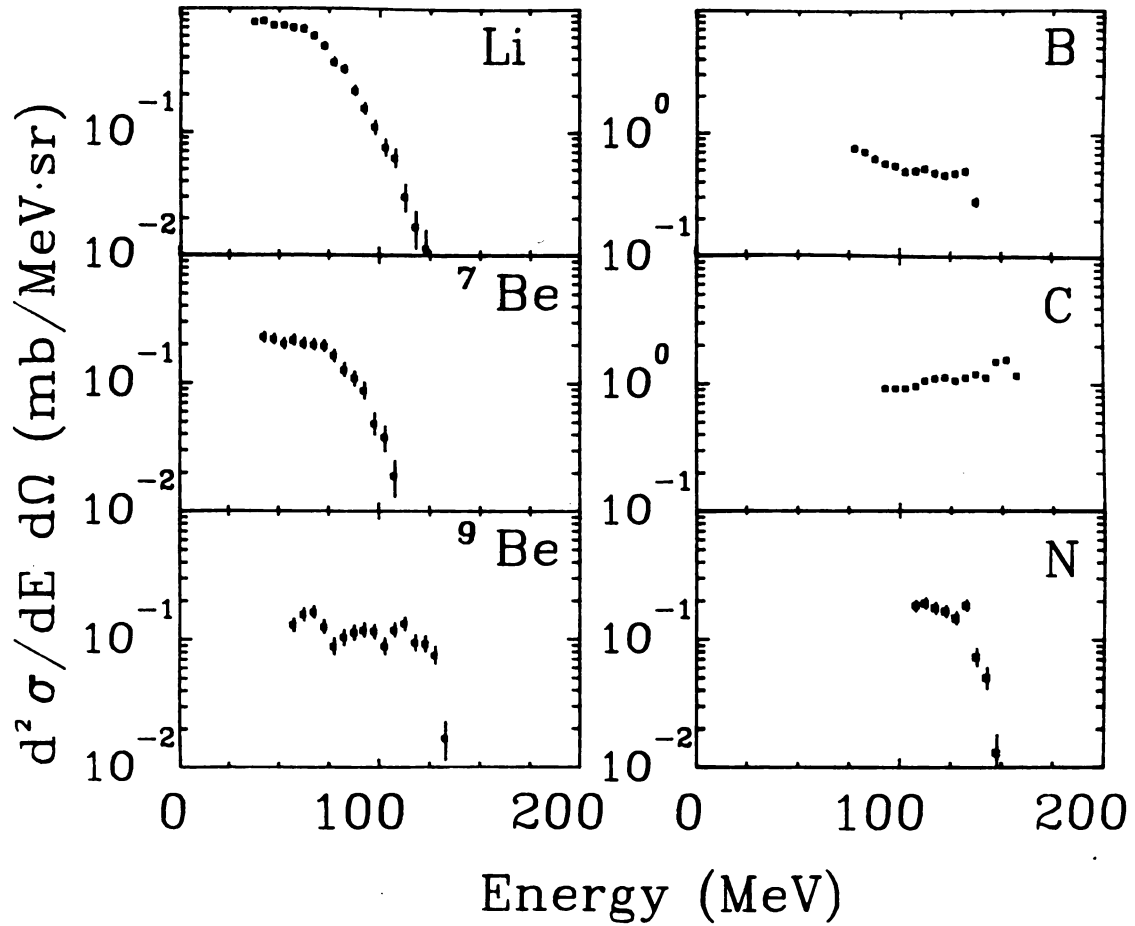


FIGURE IV-7

Projectile-like fragment inclusive energy spectra for the PLF detector at 15° for 15 MeV/A C+C.

30 MeV/nucleon C+Au

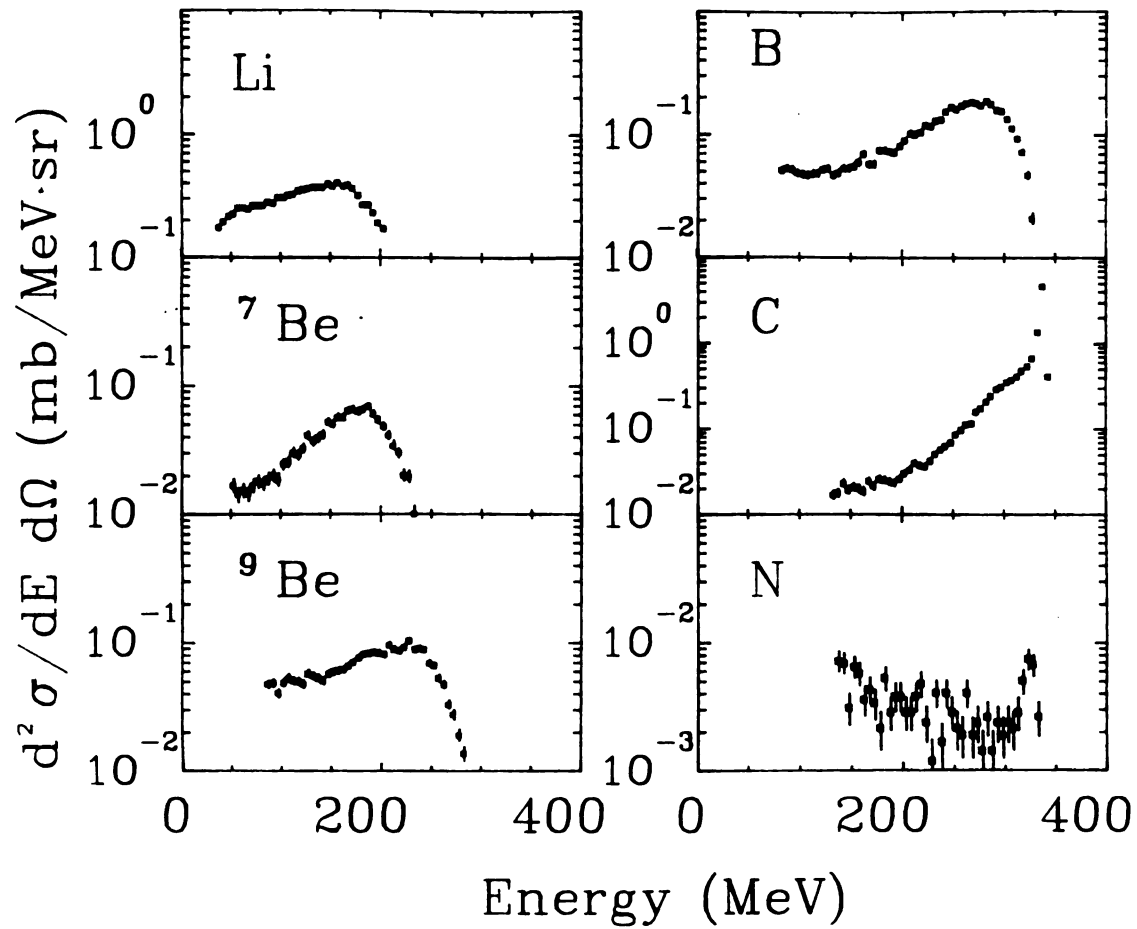


FIGURE IV-8

Projectile-like fragment inclusive energy spectra for the PLF detector at 15° for 30 MeV/A C+Au.

30 MeV/nucleon C+C

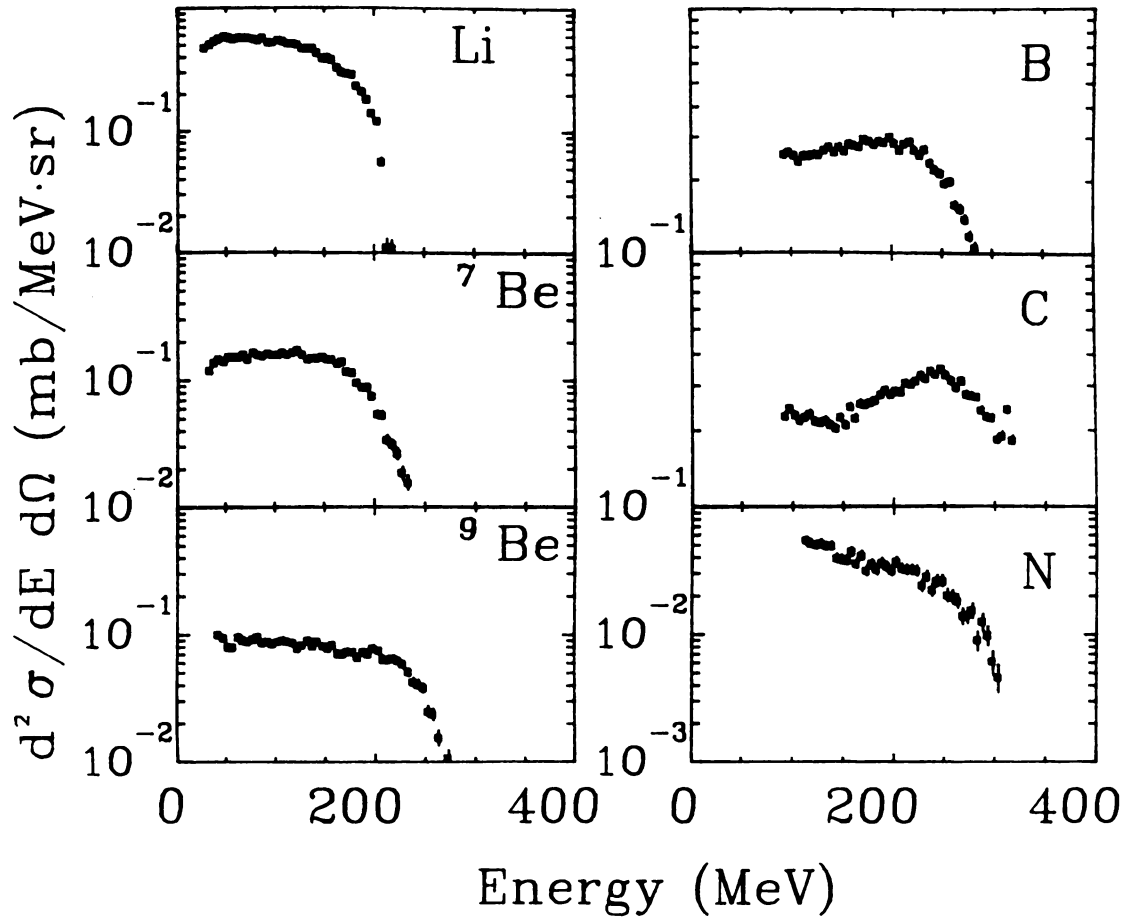


FIGURE IV-9

Projectile-like fragment inclusive energy spectra for the PLF detector at 15° for 30 MeV/A C+C.

are plotted as double differential cross sections as a function of the total fragment energy.

Projectile-Like Fragment spectra can be broken up into two distinct reaction mechanisms, projectile fragmentation - few nucleon transfer reaction otherwise known as quasi-elastic (QE) and an intermediate rapidity or deep-inelastic (DI) part. Projectile fragmentation can be described as an interaction occurring at large impact parameters in which the incoming projectile nucleus becomes excited upon contact with the target nucleus. The velocity of this projectile fragment is not appreciably reduced by the collision. The excited projectile either breaks up near the target nucleus before equilibration of the excitation energy or decays in flight after thermal equilibrium is established. The fragment velocity distributions for the projectile fragmentation process can be characterized by observed peaks which are gaussian in shape with their centroid between 85 and 90 percent of the projectile velocity. The beryllium and boron fragment velocity distribution seem to be dominated by this reaction mechanism. The QE part of the PLF spectra could also be associated with a few nucleon transfer reaction mechanism. This phenomenon involves the exchange between target and projectile nuclei of one or more nucleons. The fragment velocity distributions for the transfer process are characterized by narrow peaks centered near the beam velocity. The carbon and nitrogen fragment velocity distribution seem to be dominated by this reaction



mechanism. Hasselquist et al. [Ha 85] have shown that it is difficult to distinguish these different processes for these energies and systems. Because the energies for these processes are not well separated, it is assumed that a combination of these processes are involved.

The DI part of the PLF energy spectra can be associated with smaller impact parameters. This mechanism is usually associated with particles which are much lower in velocity than the beam velocity and are emitted from a more thermalized source. This reaction mechanism can be thought of as the transfer of nucleons between the projectile and target while they rotate usually less than one turn, then the projectile fragment is ejected. By using that part of the PLF energy spectra which is below the quasi-elastic peak, one can be assured of getting only the DI reaction part of the spectra.

B. 15 and 30 MeV/nucleon $^{12}\text{C}+\text{Au,C}$ Coincidence Spectra

1. Momentum Conservation Model

In order to interpret coincidence spectra as a collective and dynamic effect, the effects due simply to momentum conservation must be considered. This precaution would prevent you from assigning any special significance to effects which are simply due to conservation laws. It is therefore necessary to use a simple momentum conservation model and construct a theoretical coincidence spectra. By

comparing these theoretical calculations with the actual data, one can now eliminate any simple momentum conservation effects. However, it is impossible to reconstruct realistically any nuclear reaction with any simple model that must have limitations due to assumptions which are made in order to simplify the calculations. It is still useful to be able to compare measured data with even the simplest level of calculation.

The momentum conservation calculation is based on a treatment by Lynch, et al. [Ly 82] and formulated by Hasselquist [Ha 84]. The calculation assumes that particles are emitted isotropically in the rest frame of a moving thermal source with a fixed number of nucleons. The energy distribution is given by the relativistic Maxwell-Boltzmann distribution (IV-1). The coincidence spectra are calculated based on the moving source fits to the inclusive spectra. The calculation is performed assuming that two coincident particles are emitted sequentially from a single moving source. In reality, more than two particles are usually emitted from these type of reactions, however, the requirement of the emission of two particles is essential to the calculation. By knowing the momentum of the first particle, it is possible to calculate the reduction in excitation energy of the source and its recoil momentum. The second particle is then emitted from this new cooled down and recoiling source. It is impossible to determine which particle was emitted first, therefore both

combinations of sequential emission must be considered and then combined to give the final coincidence spectra. The initial source parameters used in the calculations were those extracted from the inclusive light particle spectra for the particle of interest. The initial calculations were done with the size of the emitting source corresponding to a fireball formed at the most probable impact parameter [We 76]. In order to obtain a more realistic coincidence spectra, it was necessary to integrate over different source sizes weighted by their geometric probability ($2\pi bN(b)$), where b is the impact parameter and $N(b)$ is the number of nucleons at the impact parameter b . Figures IV-10 and IV-11 show the weight assigned for each source size for the C+Au and C+C systems, respectively. The calculated spectra for the reactions were arbitrarily normalized in order to compare the shapes of the distributions. The same energy cutoffs that the detectors had were incorporated into the calculations in order to compare with the measurements.

2. Light Particle - Bragg Curve Coincidence

The proton spectra that are in coincidence with the slow moving target-like fragments in the Bragg Curve Spectrometer are shown in Figures IV-12-13 for the 30 MeV/nucleon C+Au,C respectively. All of the coincidence spectra that are presented here have been divided by the solid angle of the trigger detector. The solid curves in the figures are moving source fits to the data with the same

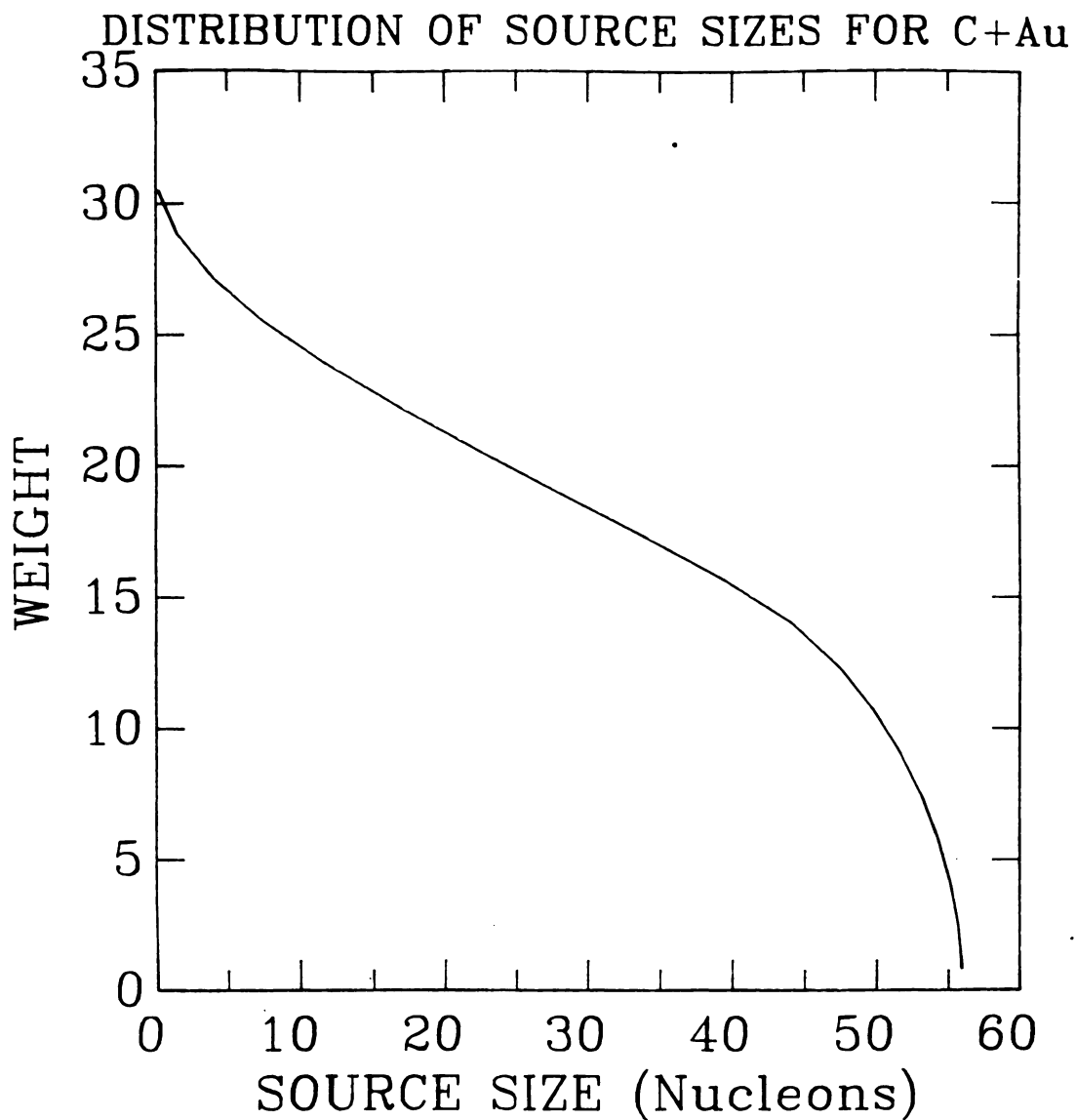


FIGURE IV-10

The weighted distribution of source sizes for the momentum conservation calculation based on $2\pi bN(b)$ for C+Au.

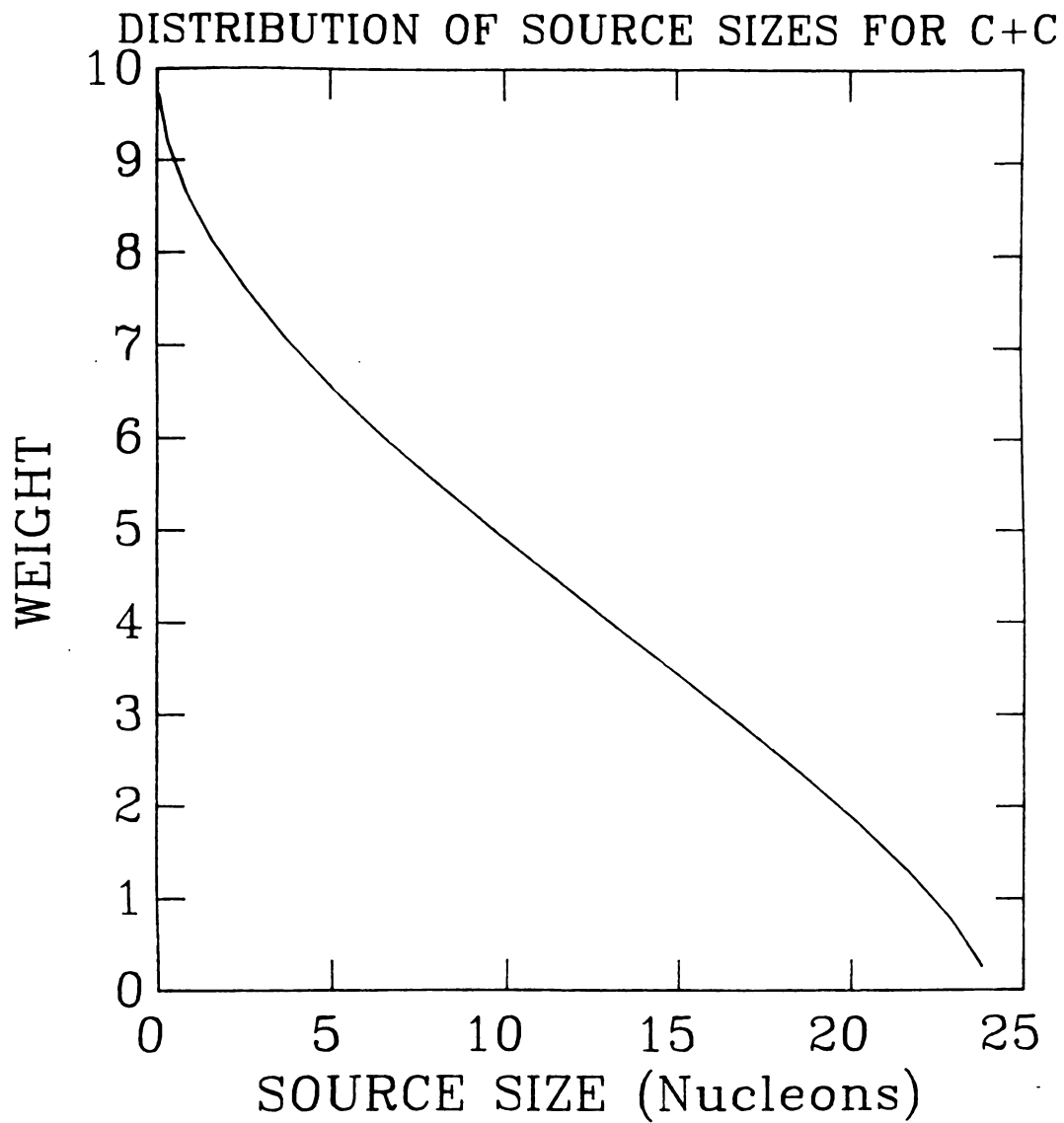


FIGURE IV-11

The weighted distribution of source sizes for the momentum conservation calculation based on $2\pi bN(b)$ for C+C.

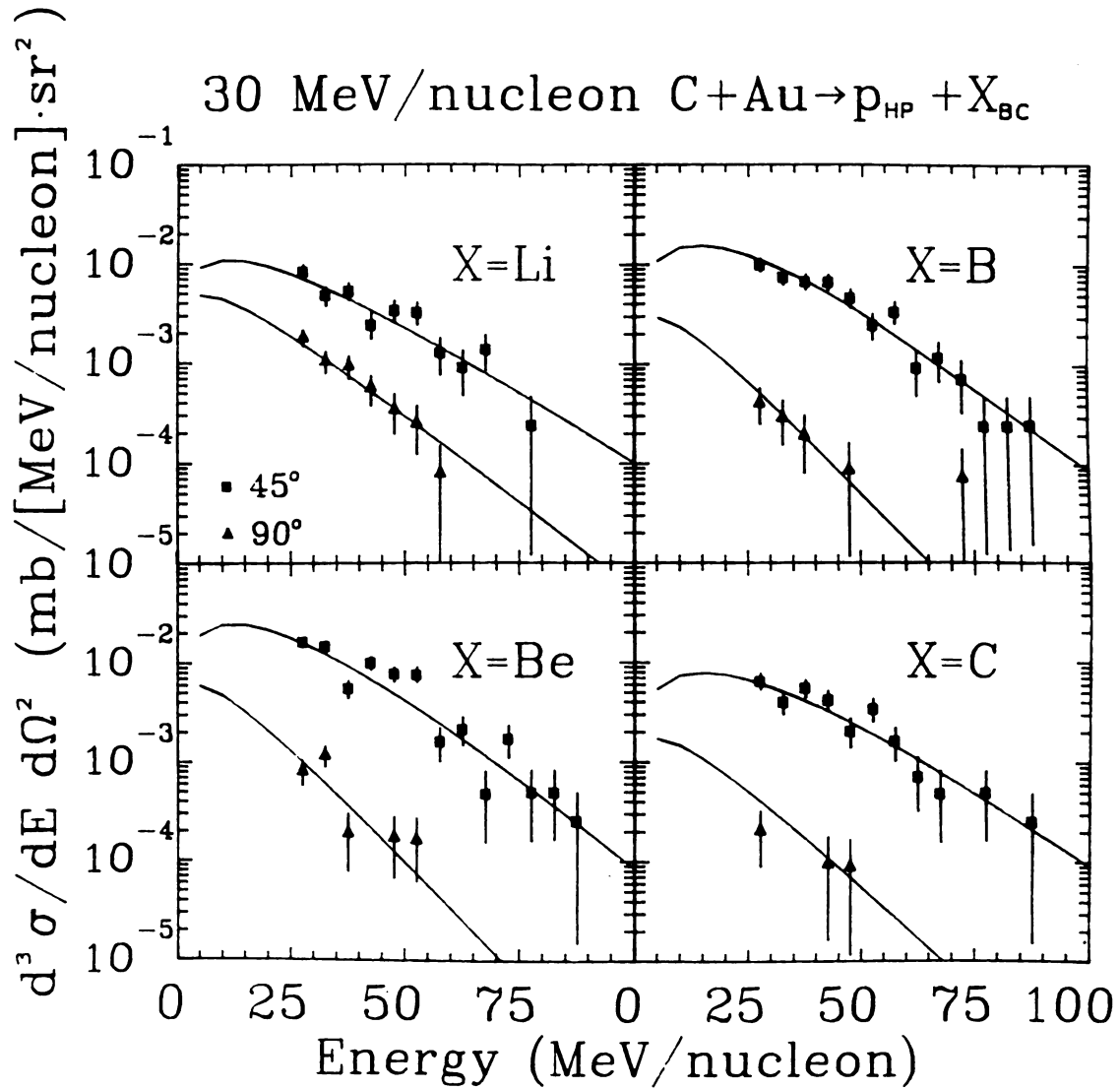


FIGURE IV-12

Energy spectra for protons at 45° in the Hit plastics in coincidence with the BCS for 30 MeV/A C+Au. Solid lines correspond to a moving source fit.

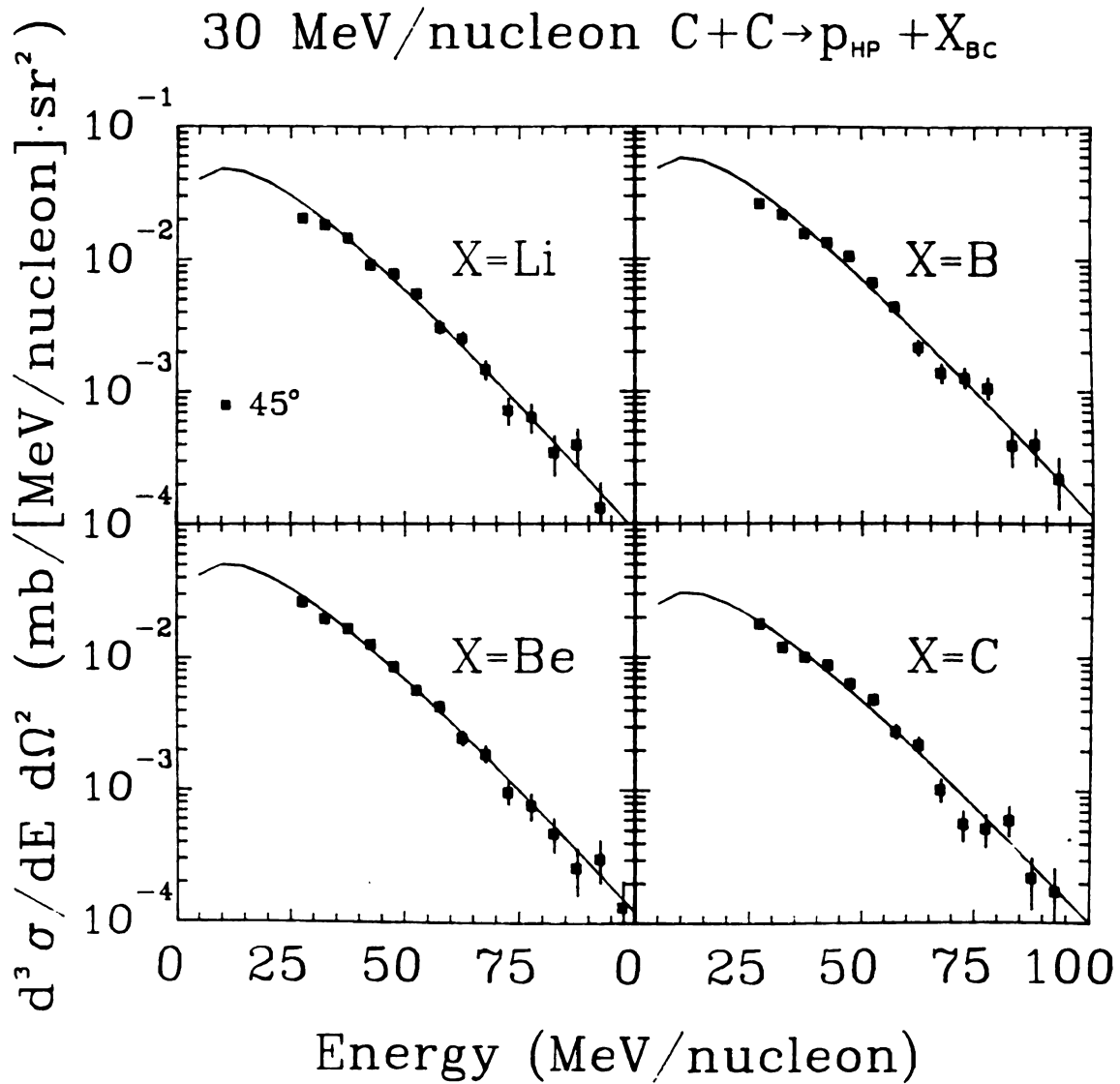


FIGURE IV-13

Energy spectra for protons at 45° in the Hit plastics in coincidence with the BCS for 30 MeV/A C+C. Solid lines correspond to a moving source fit.

energy cuts as the inclusive data. The extracted moving source fit parameters for the BCS triggered proton coincidence spectra are tabulated in Tables IV-3-10. The temperatures from the fits for 30 MeV/nucleon C+Au,C are plotted in Figures IV-14 and IV-15, respectively, as ratios to the inclusive values. The square symbols are the light particles on the same side of the trigger detector and the triangle symbols are for the light particles on the opposite side. There seems to be no significant dependence of the temperature and velocity parameters on the mass of the trigger particle. The deviations from 1 appear to have no significance. The 15 MeV/nucleon temperature ratios showed the same trend. The protons were the only light particle fit to a moving source because the other light particles did not have enough statistics to do so. Another form of light particle or mass dependence in which all the light particles can be compared, is found by simply integrating the coincidence energy spectra and comparing correlations. These correlation functions will be presented later in this chapter.

3. Light Particle - Projectile Like Fragment Coincidence

The proton spectra that are in coincidence with the quasi-elastic (QE) and deep inelastic (DI) part of the projectile-like fragments in the PLF detector are shown in Figures IV-16-19, respectively for the 30 MeV/nucleon C+Au,C. The extracted moving source fit parameters for the

TABLE IV-3

MOVING SOURCE PARAMETERS 30 MeV/A C+Au→p (COINCIDENCE HP)

Fragment	Temperature	Cross section	Velocity	
Mass	τ	σ	β	
	(MeV)	(mb)	(c)	
QE	7	12.3±1.1	35.2±5.2	0.302±0.006
	9	10.6±1.4	30.5±8.	0.145±0.008
	11	7.5±1.0	75.±30.	0.106±0.006
	12	14.1±1.5	39.5±5.7	0.084±0.005
DI	7	12.6±1.5	31.±6.	0.112±0.006
	9	18.±5.	9.±2.	0.118±0.002
	11	22.±5.	11.±2.	0.136±0.002
	12	15.±3.	12.±3.	0.147±0.002
BC	7	11.±1.	2.3±0.4	0.11±0.05.
	9	8.6±0.5	4.3±0.6	0.14±0.04
	11	8.6±0.6	2.9±0.4	0.16±0.05
	12	9.7±0.9	1.6±0.3	0.16±0.09

TABLE IV-4

MOVING SOURCE PARAMETERS 30 MeV/A C+Au→p (COINCIDENCE BP)

Fragment	Temperature	Cross section	Velocity	
Mass	τ	σ	β	
	(MeV)	(mb)	(c)	
QE	4	9.9±0.3	226.±12.	0.13±0.02
	7	9.0±0.8	48.±8.	0.17±0.04
	9	12.±3.	11.±2.	0.16±0.09
	11	9.±1.	26.±7.	0.10±0.05
	12	10.8±0.8	41.±6.	0.12±0.03
DI	4	9.9±0.2	378.±15.	0.13±0.01
	7	11.±1.	21.±3.	0.14±0.05
	9	13.1±3.	6.±1.	0.16±0.01
	11	10.±2.	13.±4.	0.118±0.009
	12	10.±1.	19.±3.	0.144±0.006
BC	7	12.±2.	0.76±.14	0.132±0.006
	9	9.4±0.4	3.2±0.2	0.206±0.003
	11	7.9±0.5	2.4±0.3	0.181±0.004
	12	10.6±0.6	1.7±0.2	0.196±0.004
	14	10.±1.5	0.68±0.9	0.19±0.01

TABLE IV-5

MOVING SOURCE PARAMETERS 30 MeV/A C+C+p (COINCIDENCE BP)

Particle		Temperature	Cross section
		τ (MeV)	σ (mb)
QE	4	7.49 ± 0.04	$357. \pm 7.$
	7	7.47 ± 0.09	$79. \pm 3.$
	9	7.0 ± 0.5	$34. \pm 2.$
	11	7.2 ± 0.8	$20. \pm 2.$
	12	$11. \pm 3.$	1.1 ± 0.5
DI	4	8.84 ± 0.06	$862. \pm 9.$
	7	8.8 ± 0.2	$97. \pm 3.$
	9	8.2 ± 0.4	$57. \pm 3.$
	11	8.2 ± 0.2	$116. \pm 3.$
	12	7.4 ± 0.1	$83. \pm 3.$
BC	7	9.1 ± 0.3	1.54 ± 0.05
	9	9.38 ± 0.05	5.8 ± 0.1
	11	9.6 ± 0.1	5.2 ± 0.1
	12	9.8 ± 0.2	2.5 ± 0.7
	14	$13. \pm 3.$	0.25 ± 0.007

TABLE IV-6

MOVING SOURCE PARAMETERS 30 MeV/A C+C+p (COINCIDENCE HP)

Particle		Temperature	Cross section
		τ	σ
		(MeV)	(mb)
QE	4	8.1 ± 0.2	$289. \pm 8.$
	7	8.5 ± 0.4	$68. \pm 4.$
	9	7.7 ± 0.2	$38. \pm 3.$
	11	8.0 ± 0.4	$22. \pm 2.$
	12	$7. \pm 3.$	$8. \pm 2.$
DI	4	8.9 ± 0.1	$916. \pm 13.$
	7	8.7 ± 0.3	$116. \pm 5.$
	9	9.1 ± 0.5	$61. \pm 3.$
	11	9.3 ± 0.2	$140. \pm 5.$
	12	8.9 ± 0.4	$105. \pm 4.$
	14	$14. \pm 5.$	$10. \pm 1.$
BC	7	8.4 ± 0.2	7.8 ± 0.2
	9	8.71 ± 0.06	8.4 ± 0.2
	11	8.4 ± 0.1	9.5 ± 0.2
	12	9.1 ± 0.2	5.3 ± 0.1
	14	$37. \pm 15.$	0.07 ± 0.02

TABLE IV-7

MOVING SOURCE PARAMETERS 15 MeV/A C+C→p (COINCIDENCE HP)

Particle		Temperature	Cross section
		τ	σ
		(MeV)	(mb)
QE	4	6.8 ± 0.9	$130. \pm 16.$
	7	$14. \pm 4.$	$9. \pm 3.$
DI	4	5.5 ± 0.5	$431. \pm 40.$
	9	$10. \pm 7.$	$5. \pm 2.7$
	11	6.0 ± 0.5	$56. \pm 13.$
	12	$8. \pm 2.$	$22. \pm 7.$
BC	7	6.1 ± 0.4	$22. \pm 1.4$
	9	5.7 ± 0.3	$50. \pm 2.$
	11	5.7 ± 0.2	$70. \pm 3.$
	12	5.7 ± 0.2	$54. \pm 3.$
	14	$7. \pm 3.$	$1. \pm 0.3$

TABLE IV-8

MOVING SOURCE PARAMETERS 15 MeV/A C+C→p (COINCIDENCE BP)

Particle		Temperature	Cross section
		τ	σ
		(MeV)	(mb)
QE	4	5.9 ± 0.2	$270. \pm 14.$
	7	$7. \pm 2.5$	$13. \pm 3.$
	11	7.9 ± 0.7	5.8 ± 0.2
	12	$10. \pm 3.$	$5. \pm 2.$
DI	4	6.2 ± 0.2	$396. \pm 16.$
	7	4.4 ± 0.9	$64. \pm 11.$
	9	7.7 ± 0.9	$7. \pm 1.8$
	11	5.3 ± 0.5	$51. \pm 7.5$
	12	6.8 ± 0.3	$42. \pm 5.$
BC	7	6.4 ± 0.2	7.5 ± 0.4
	9	5.9 ± 0.1	$64. \pm 1.$
	11	5.97 ± 0.09	$78. \pm 1.$
	12	5.9 ± 0.1	$41. \pm 1.$
	14	$8. \pm 2.$	0.44 ± 0.08

TABLE IV-9

MOVING SOURCE PARAMETERS 15 MeV/A C+Au+p (COINCIDENCE HP)

Particle		Temperature	Cross section
		τ	σ
		(MeV)	(mb)
QE	4	9. ±4.	0.4 ±0.3
	7	7.6 ±0.8	8.1 ±0.1
	9	6.1 ±0.7	17. ±2.
	11	5.5 ±0.2	66. ±5.
	12	6.04 ±0.02	4688. ±32.
	14	6.8 ±0.7	22. ±2.
DI	4	6.2 ±0.3	85. ±4.
	7	15. ±5.	0.7 ±0.2
	9	17. ±6.	1.2 ±0.3
	11	6.2 ±0.6	8. ±1.3
	12	5.7 ±0.4	50. ±4.
	14	6.6 ±0.8	2.0 ±0.6
BC	7	6.1 ±0.3	1.9 ±0.1
	9	6.3 ±0.3	2.2 ±0.1
	11	6.2 ±0.1	2.1 ±0.1
	12	5.9 ±0.4	1.7 ±0.1
	14	9. ±2.	0.03 ±0.01

TABLE IV-10

MOVING SOURCE PARAMETERS 15 MeV/A C+Au→p (COINCIDENCE BP)

Particle		Temperature	Cross section
		τ (MeV)	σ (mb)
QE	7	6.0±0.4	15.±1.
	9	5.5±0.2	28.±1.5
	11	5.6±0.2	66.±2.2
	12	5.98±0.01	4972.±17.
	14	6.4±0.1	31.±1.2
DI	4	5.5±0.1	140.±4.
	7	7.±3.	2.1±0.3
	9	6.±1.	5.2±0.7
	11	5.4±0.3	17.±1.2
	12	5.96±0.06	47.±1.7
	14	6.9±0.5	1.6±0.3
BC	7	6.3±0.2	0.42±0.02
	9	6.0±0.1	2.4±0.06
	11	6.1±0.1	2.3±0.05
	12	6.0±0.2	1.4±0.05
	14	7.6±0.5	0.05±0.006

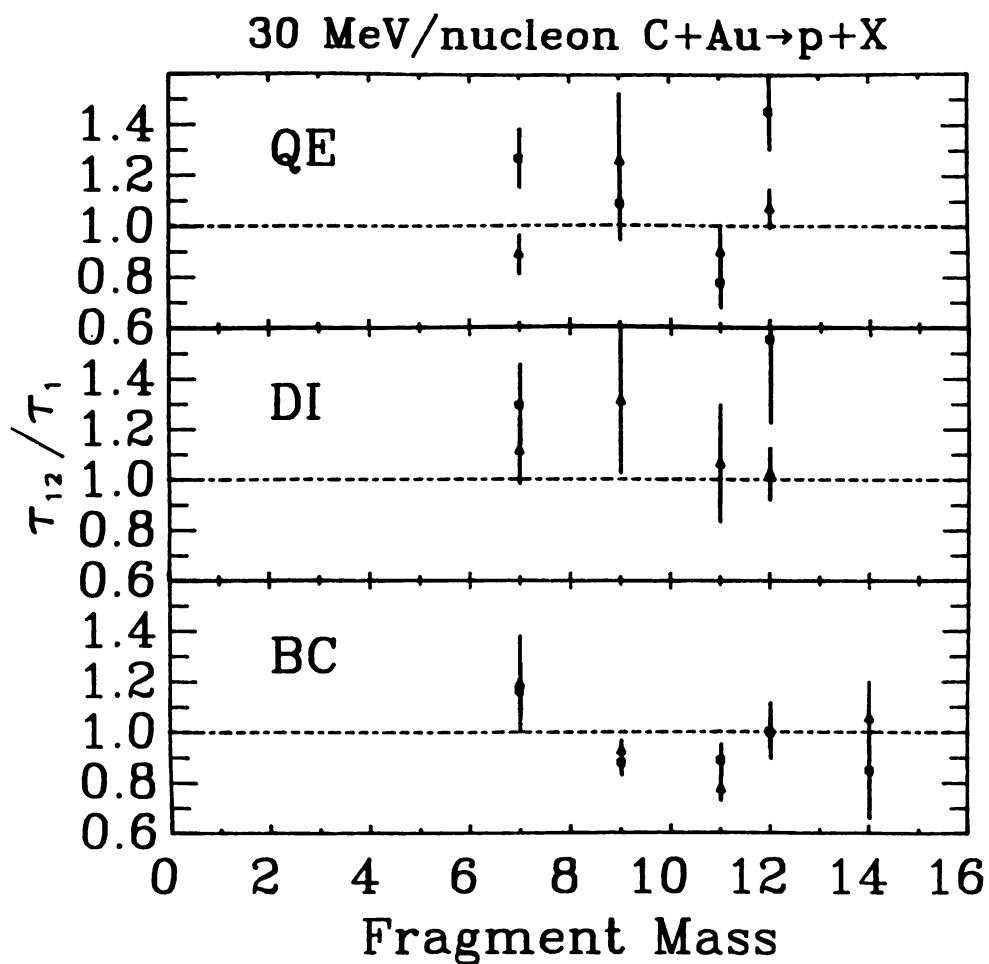


FIGURE IV-14

Ratio of coincident to inclusive temperatures from the moving source fits of protons for the quasi-elastic (QE), deep-inelastic (DI) and the bragg curve (BC) as a function of fragment mass from 30 MeV/A C+Au.

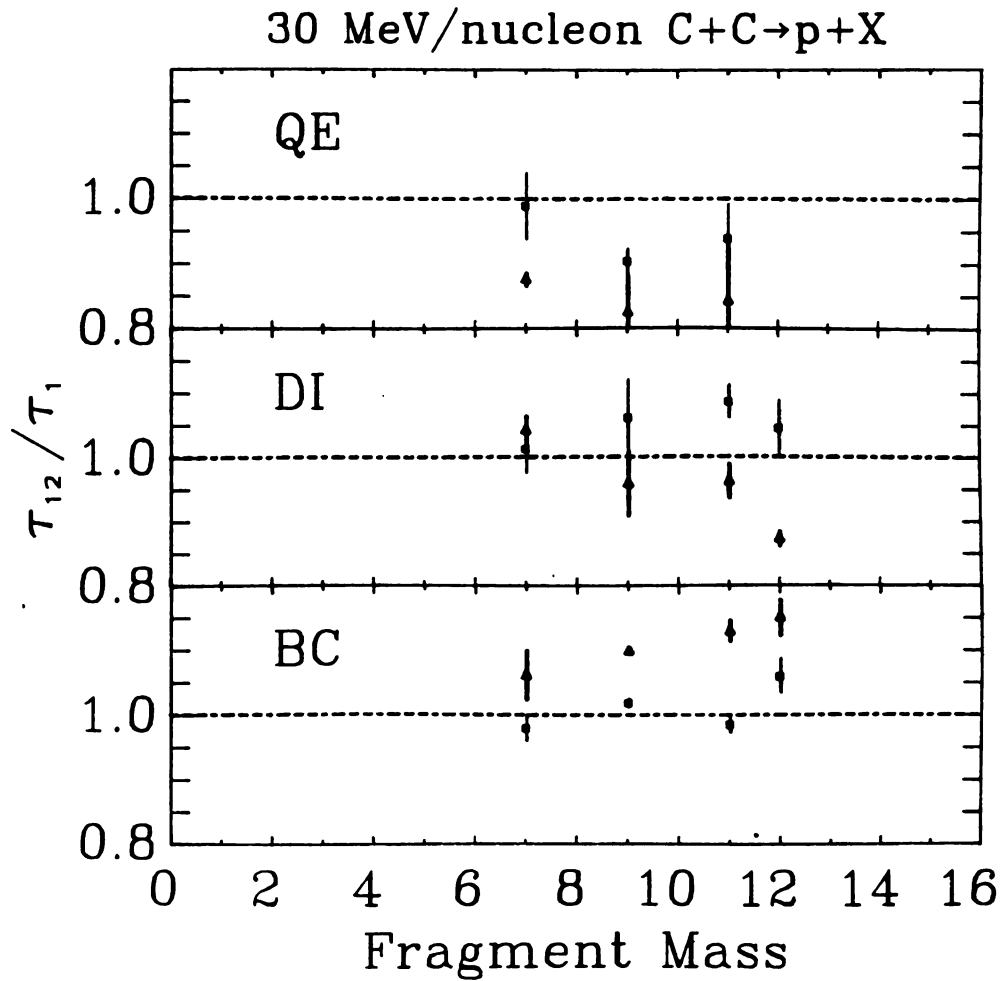


FIGURE IV-15

Ratio of coincident to inclusive temperatures from the moving source fits of protons for the quasi-elastic (QE), deep-inelastic (DI) and the bragg curve (BC) as a function of fragment mass from 30 MeV/A C+C.

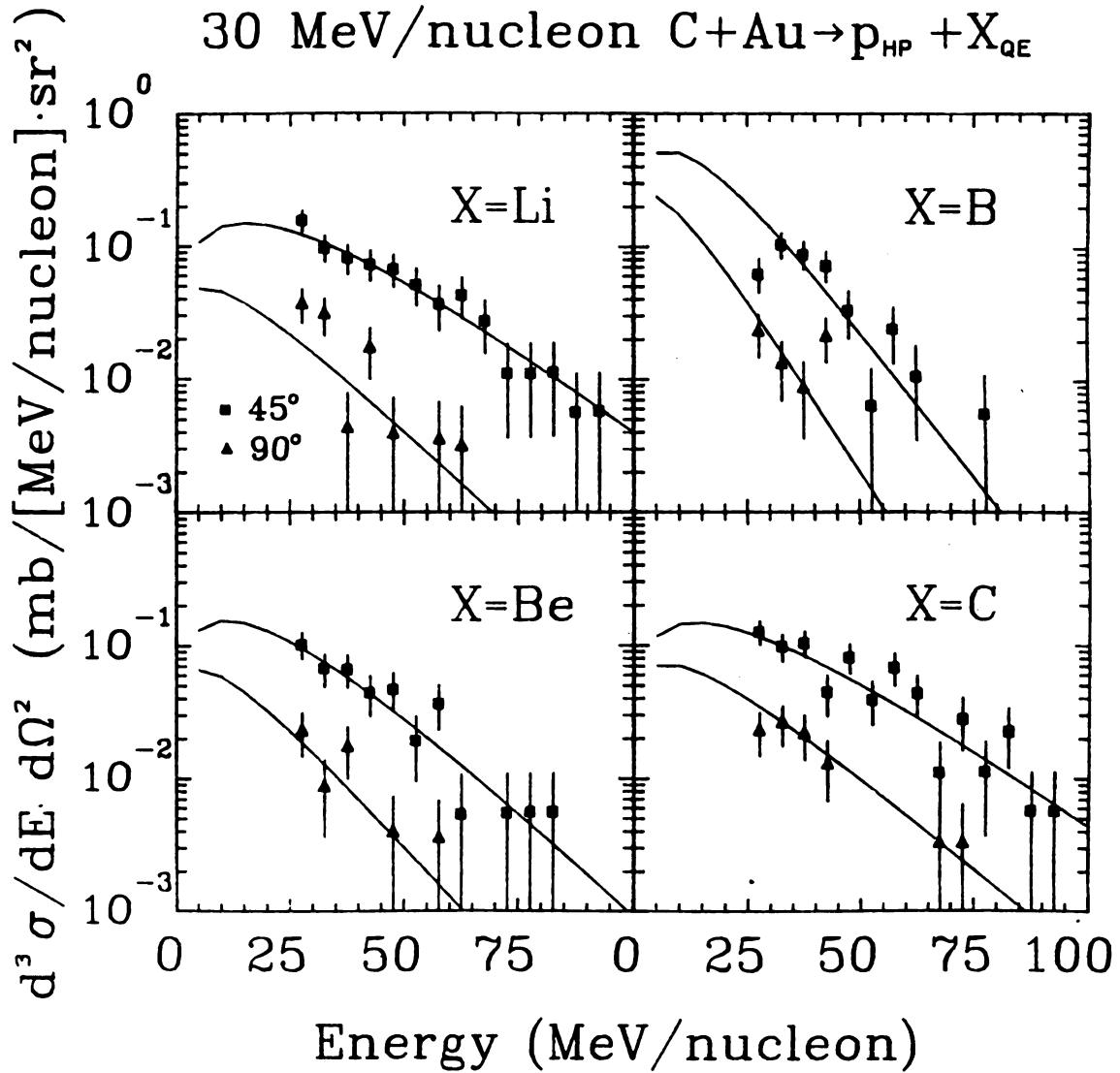


FIGURE IV-16

Energy spectra for protons at 45° in the Hit plastics in coincidence with the QE for 30 MeV/A C+Au. Solid lines correspond to a moving source fit.



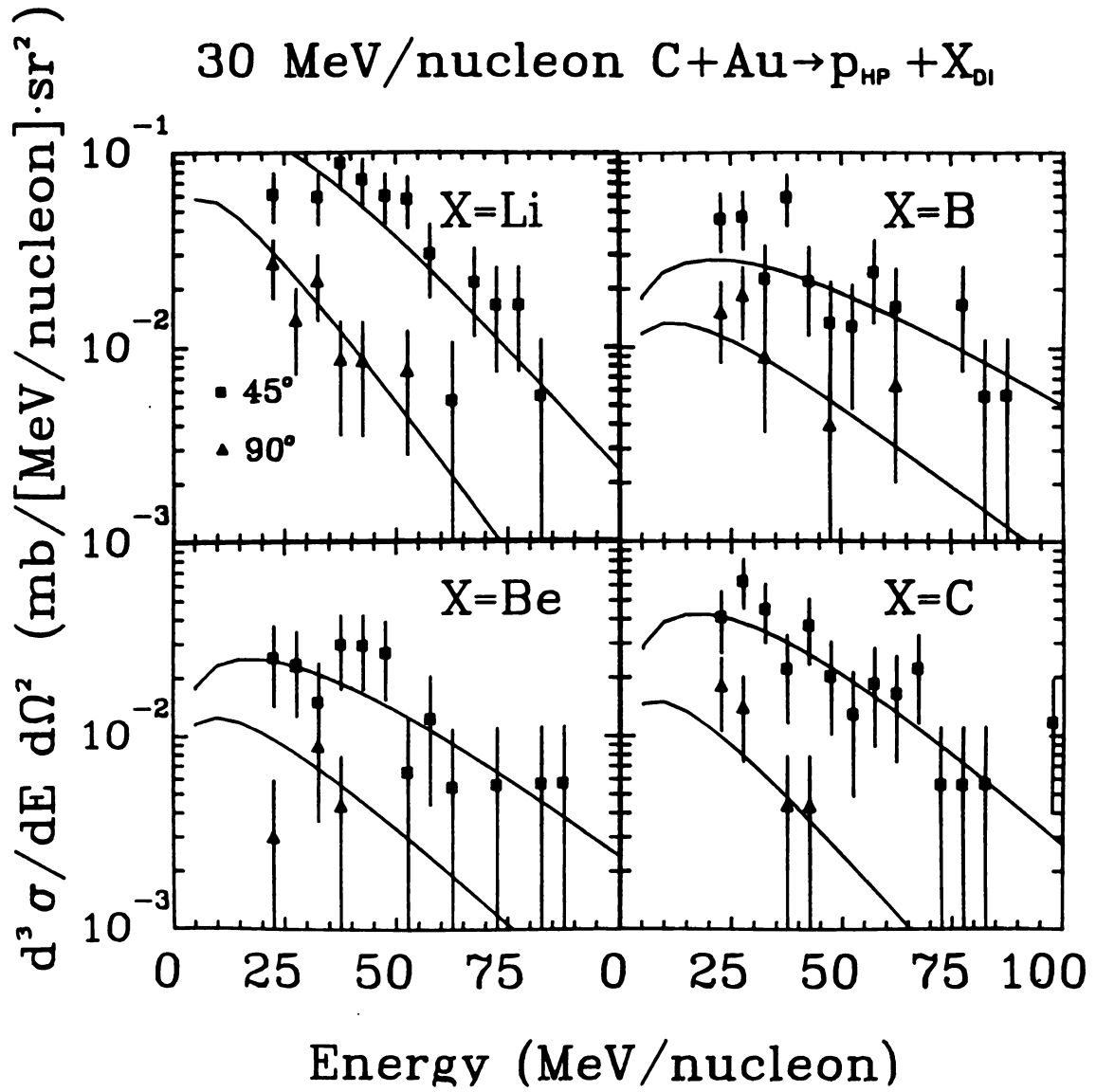


FIGURE IV-17

Energy spectra for protons at 45° in the Hit plastics in coincidence with the DI for 30 MeV/A C+Au. Solid lines correspond to a moving source fit.

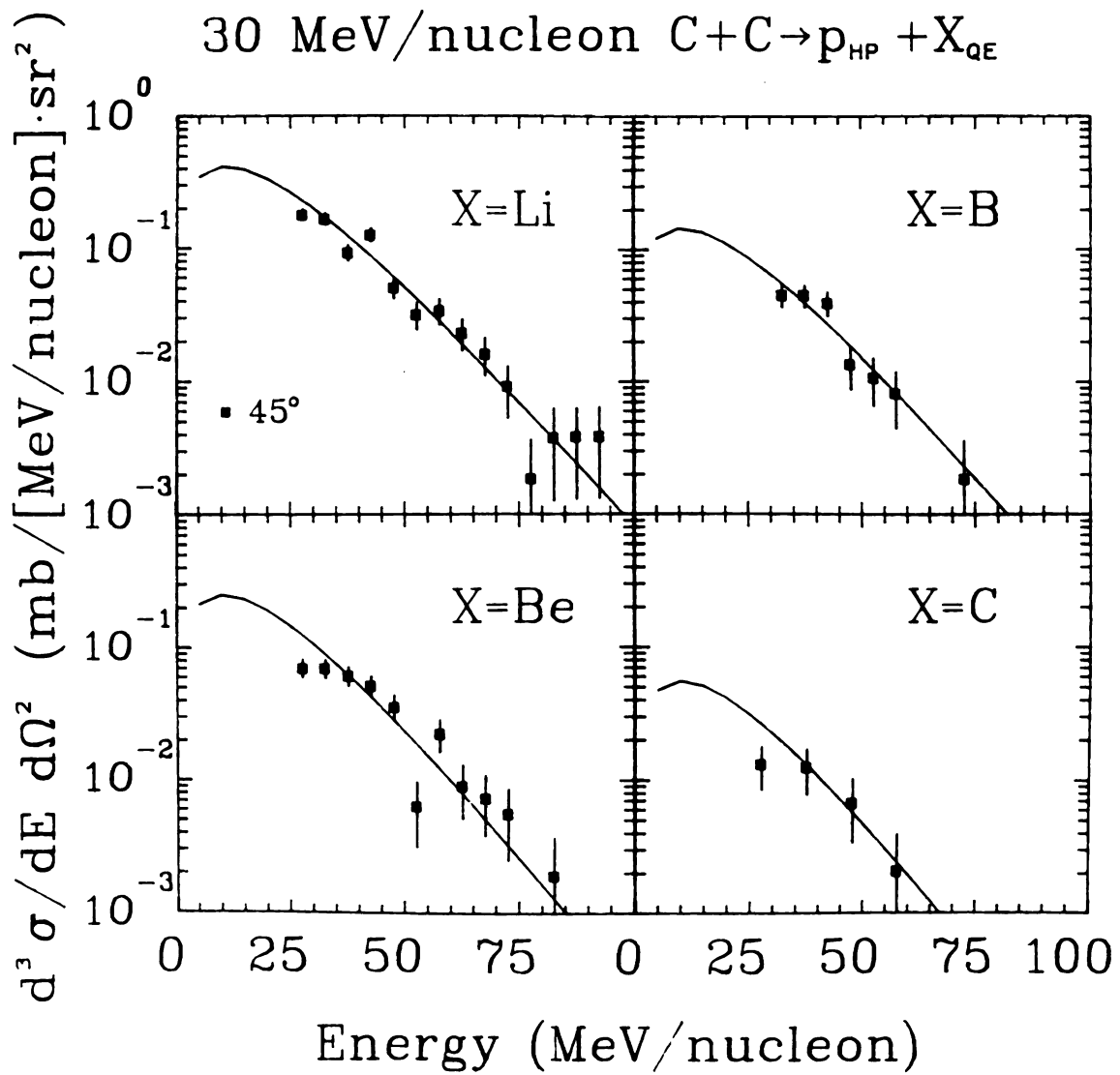


FIGURE IV-18

Energy spectra for protons at 45° in the Hit plastics in coincidence with the QE for 30 MeV/A C+C. Solid lines correspond to a moving source fit.

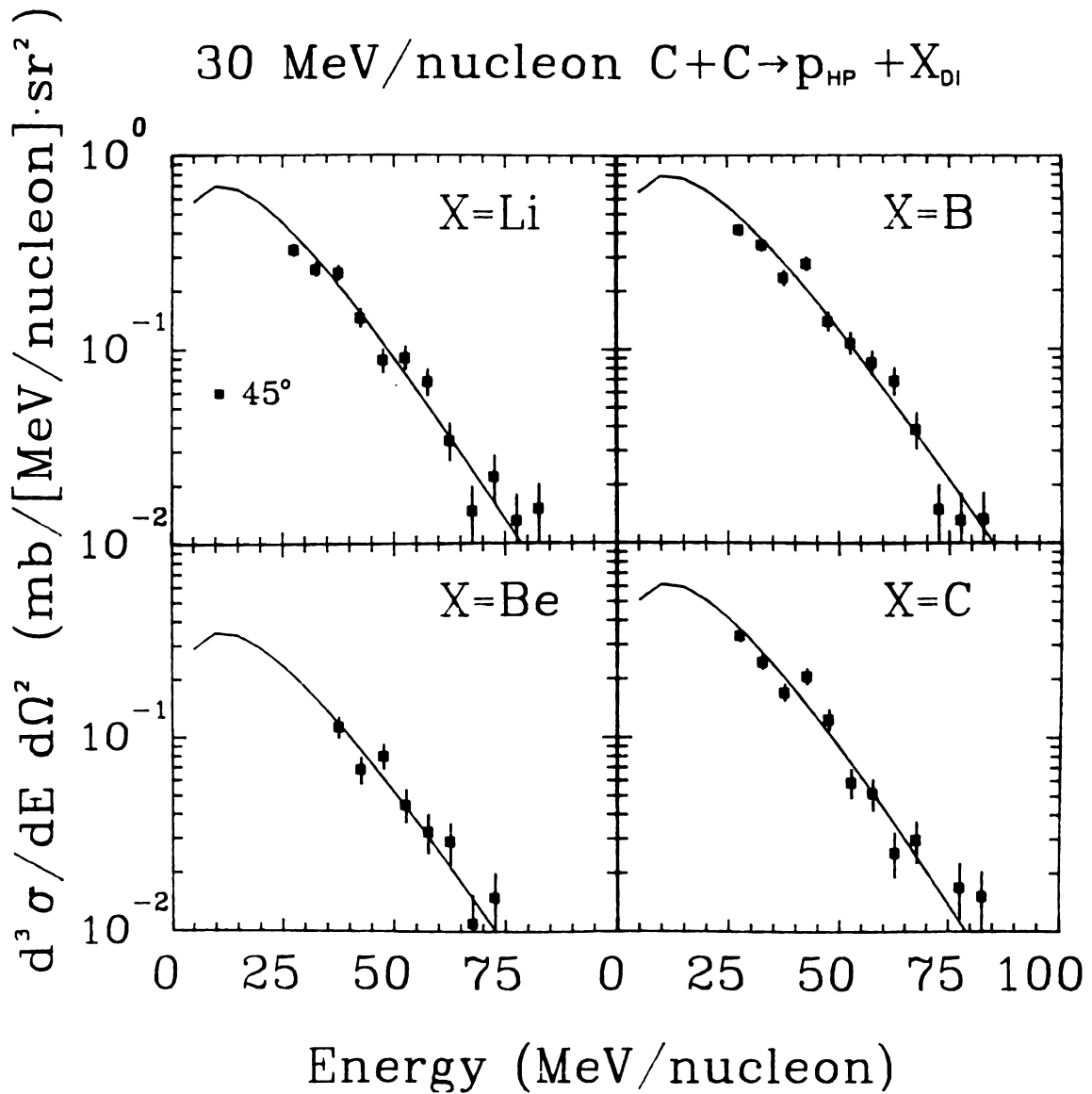


FIGURE IV-19

Energy spectra for protons at 45° in the Hit plastics in coincidence with the DI for 30 MeV/A C+C. Solid lines correspond to a moving source fit.

PLF triggered proton coincidence spectra are tabulated in Tables IV-3-10. The temperatures from the fits are plotted in Figures IV-14 and IV-15 as ratios to the inclusive values. There again seems to be no significant dependence of the temperature parameter on the mass of the trigger particle. It would at first be expected that the different coincident particles would come from different sources which in turn would have different temperatures.

4. Same Side - Opposite Side Comparison

In order to observe any collective and dynamic effects one can measure light particles in coincidence with a heavier fragment on the same and opposite sides of the reaction plane. All nuclear reaction events can be described in terms of a reaction plane described by an azimuthal angle of $\phi=0$ and 180° . For the light particle - PLF reactions, an azimuthal angle of $\phi=0^\circ$ corresponds to the side of the reaction plane on which the PLF particle was detected. These particles would be detected in the bragg curve plastic scintillator (BP) detectors. Light particles on the opposite side of the PLF would be associated with $\phi=180^\circ$ and be detected in the hit plastic (HP) scintillators. For the case of the light particle - BCS coincidence data, the reaction plane is not as easy to define. If we assign the slow moving particles detected in the bragg curve spectrometer as being emitted from the



target then we might associate this side as $\phi=180^\circ$ and where the projectile is incident on the target as the $\phi=0^\circ$ side.

First consider the light particle - BCS spectra, Figures IV-20 and IV-21 show the 30 MeV/nucleon C+C proton spectra in coincidence with lithium and carbon in the BCS at 45° , respectively. The curved lines correspond to momentum conservation calculations. In figure IV-20 the solid line refers to a single source size which best fits the data which corresponds to 18 nucleons, the dashed line refers to the weighted source size calculation. One can fit the data to a single size source but when a more realistic calculation is done, it over-predicts the data. The solid line in figure IV-21 is a single source size momentum conservation calculation using the maximum number of nucleons possible, that being 24 nucleons. The calculation over predicts the difference between the opposite and same side as compared to the data even though it uses the largest possible source size. The largest possible source size should produce the smallest possible difference from momentum conservation laws. The calculation using the weighted source sizes produces an even larger difference. The implication of these two figures is that the momentum conservation calculation does not explain these differences. This in turn might imply that they do not come from the same source instead, these particles may come from different sources such as the target fragment. These are often called target-like fragments (TLF). If one now considers the 30

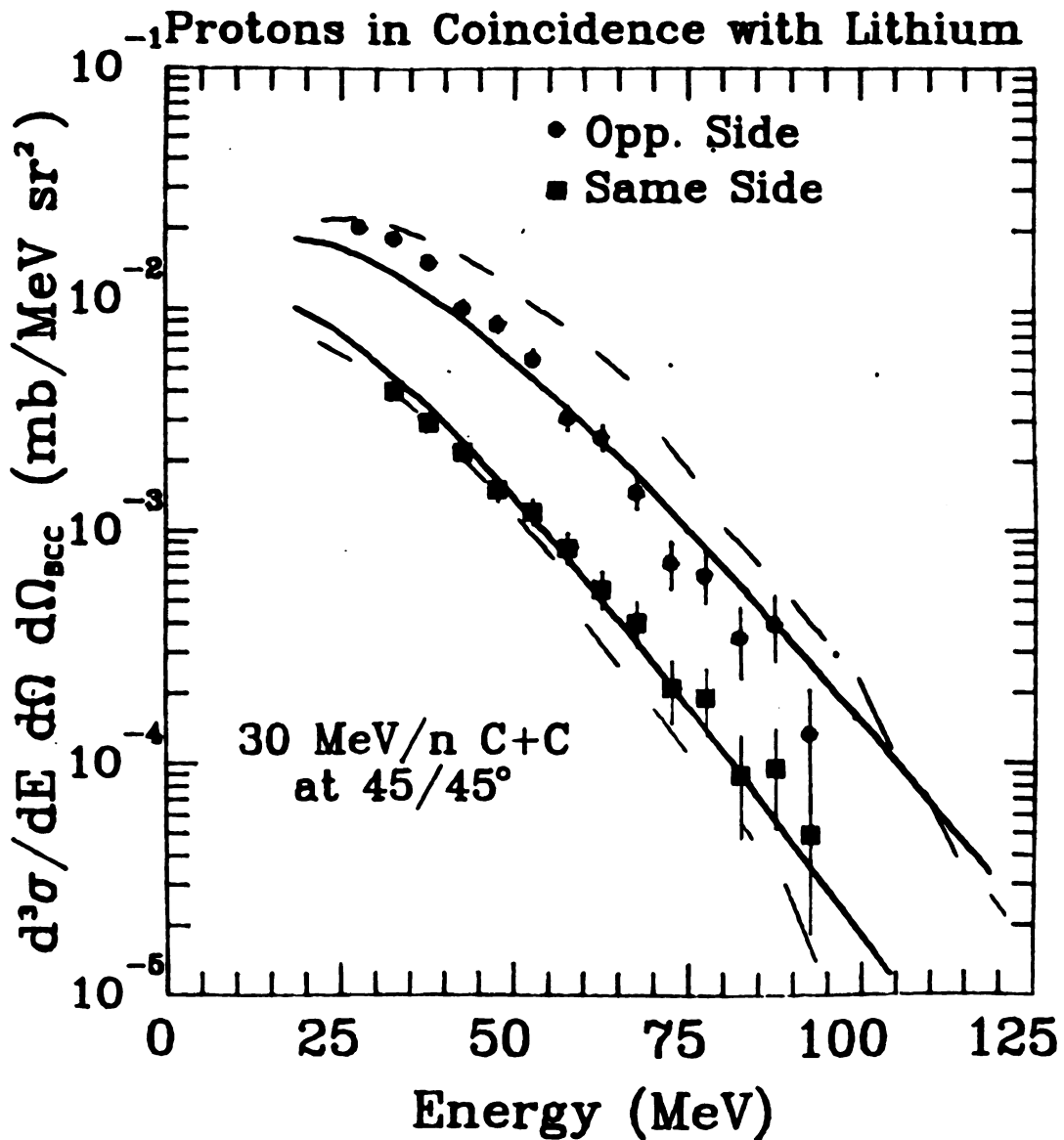


FIGURE IV-20

Proton energy spectra for the HP (opp. side) and the BP (same side) in coincidence with a lithium in the BCS for 30 MeV/A C+C. The solid (dashed) lines correspond to single (weighted) source momentum conservation calculation. The single source used 24 nucleons.

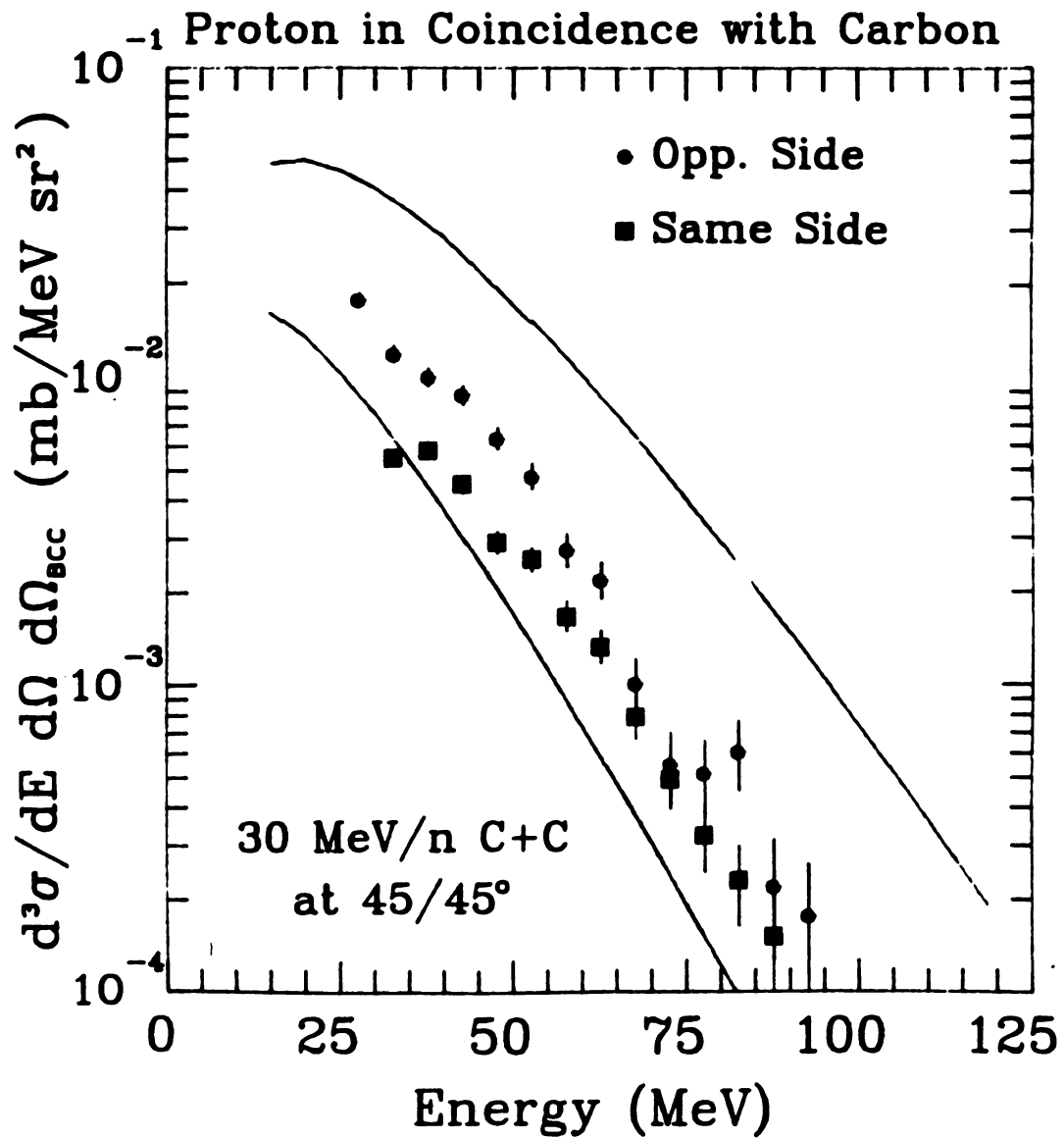


FIGURE IV-21

Proton energy spectra for the HP (opp. side) and the BP (same side) in coincidence with a carbon in the BCS for 30 MeV/A C+C. The solid (dashed) lines correspond to single (weighted) source momentum conservation calculation. The single source used 24 nucleons.

MeV/nucleon C+Au system, figures IV-22 and IV-23 show the proton spectra in coincidence with lithium and carbon in the bragg curve detector at 45° , respectively. The solid lines refer to momentum conservation calculations with a single source size of 38 nucleons which corresponds to a source formed from the most probable impact parameter in a fireball geometry. Calculations with weighted source sizes produce much larger differences. The data seem to show an almost isotropic emission of protons in coincidence with fragments detected in the BCS. Whereas the momentum conservation calculation seems to predict a large difference between the opposite and same side, which will be more evident in the integrated cross section ratios.

Differences between the light particle spectra on the same side and opposite side of a trigger detector can be examined by comparing the temperature parameters from the moving source fits. Figures IV-24-25 show the ratios of the temperatures for the protons on the same side to those on the opposite side 15 MeV/nucleon C+Au,C respectively. Figures IV-26-27 are shown for the 30 MeV/nucleon C+Au,C respectively. The figures are broken up into three different sections, the top two correspond to protons in coincidence with the quasi-elastic (QE) and deep-inelastic (DI) part of the PLF spectrum at 15° . The bottom section refers to protons in coincidence with the BCS at 45° . The proton spectra for both the same side and the opposite side were taken at 45° . The only system that varied the velocity

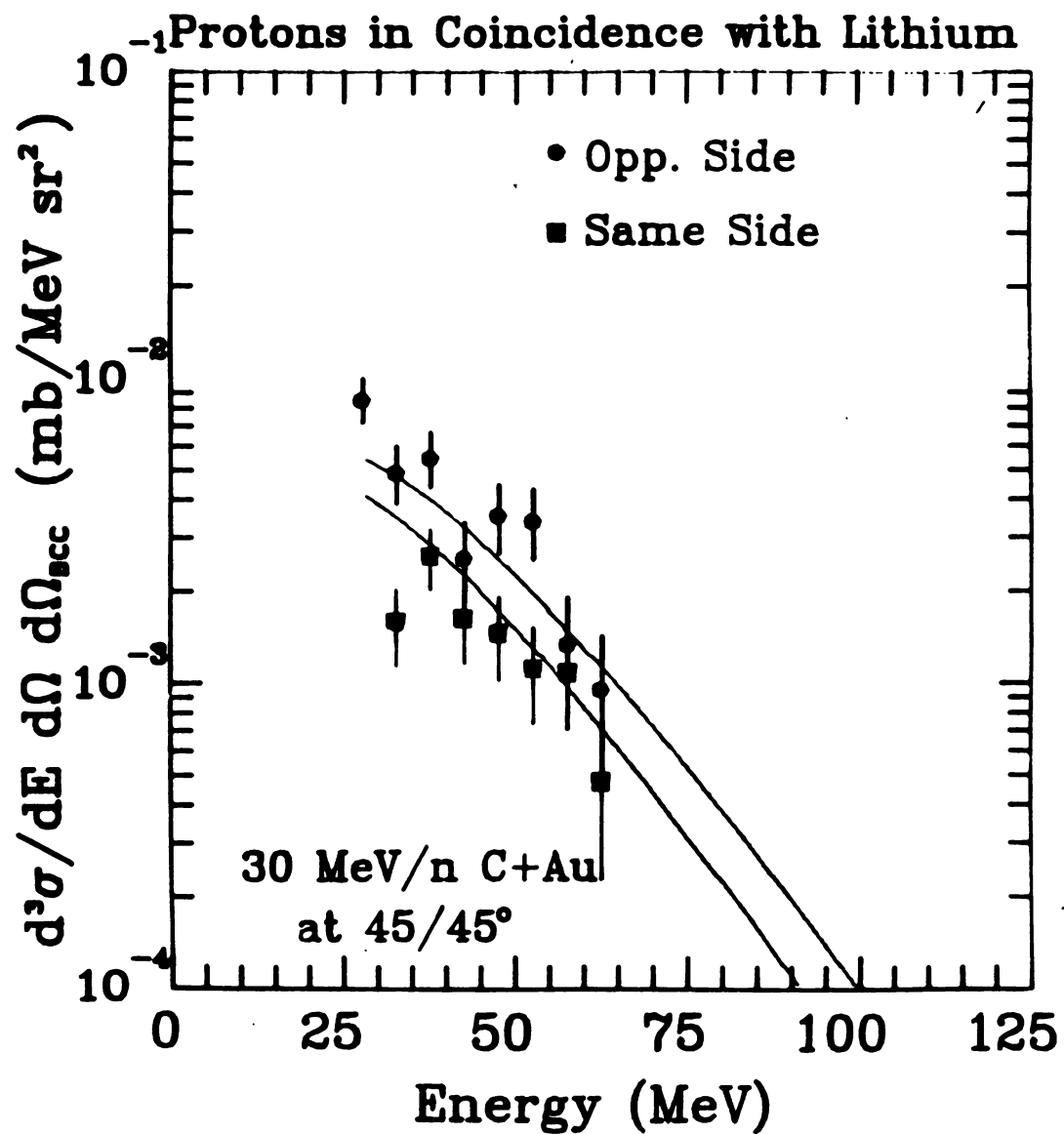


FIGURE IV-22

Proton energy spectra for the HP (opp. side) and the BP (same side) in coincidence with a lithium in the BCS for 30 MeV/A C+Au. The solid lines correspond to single (38 nucleons) source momentum conservation calculation.

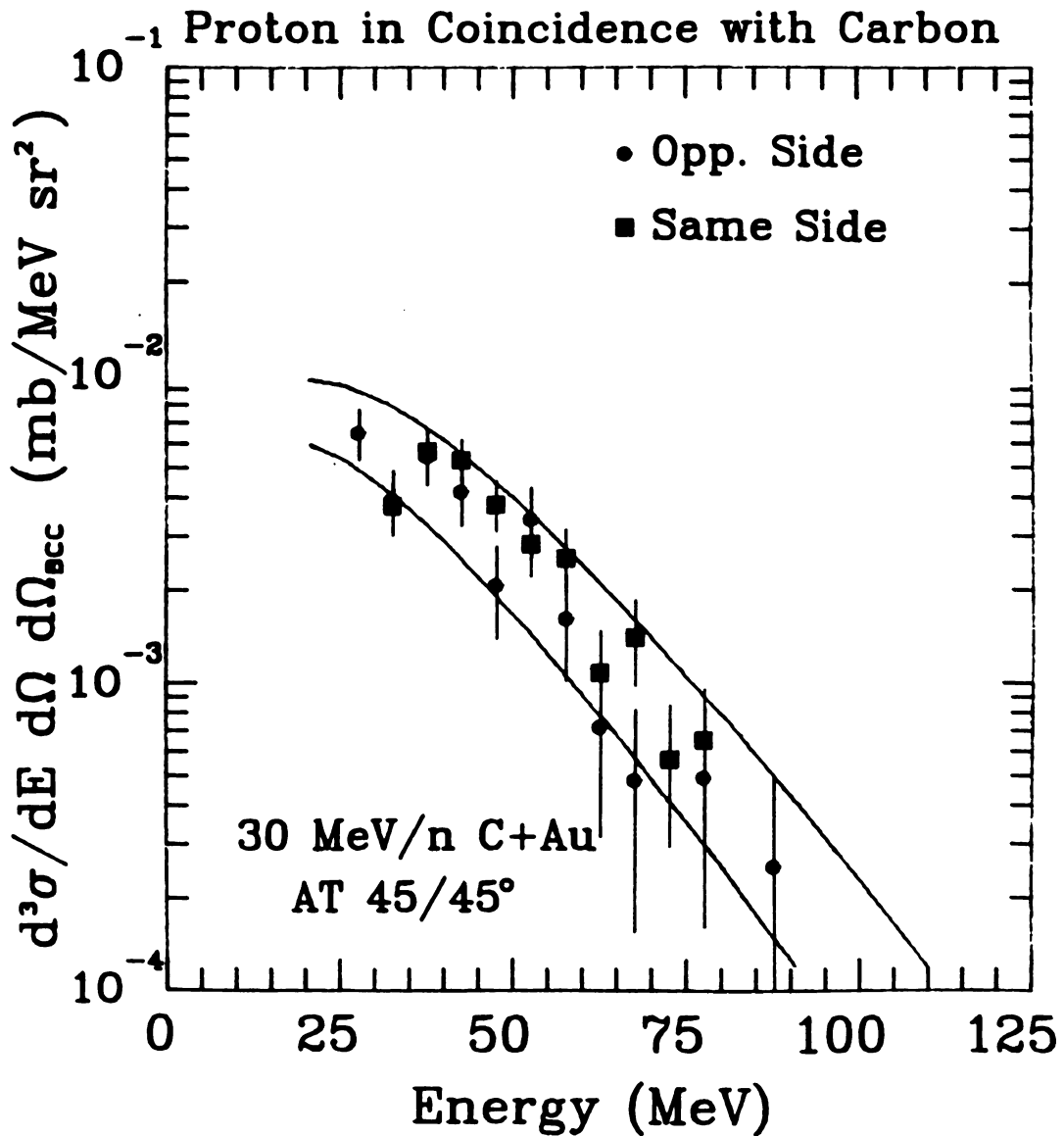


FIGURE IV-23

Proton energy spectra for the HP (opp. side) and the BP (same side) in coincidence with a carbon in the BCS for 30 MeV/A C+Au. The solid lines correspond to single (38 nucleons) source momentum conservation calculation.

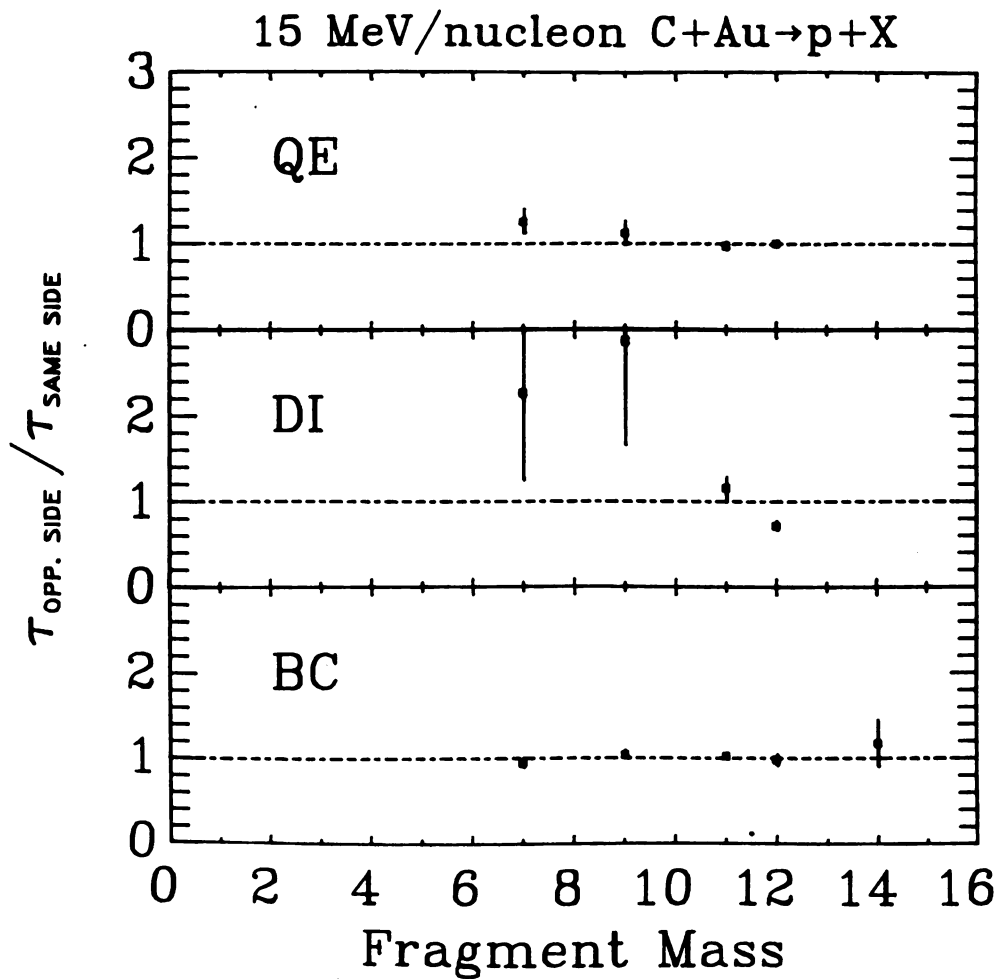


FIGURE IV-24

Ratio of opposite (HP) to same (BP) side temperatures from the moving source fits for 15 MeV/A C+Au for protons.

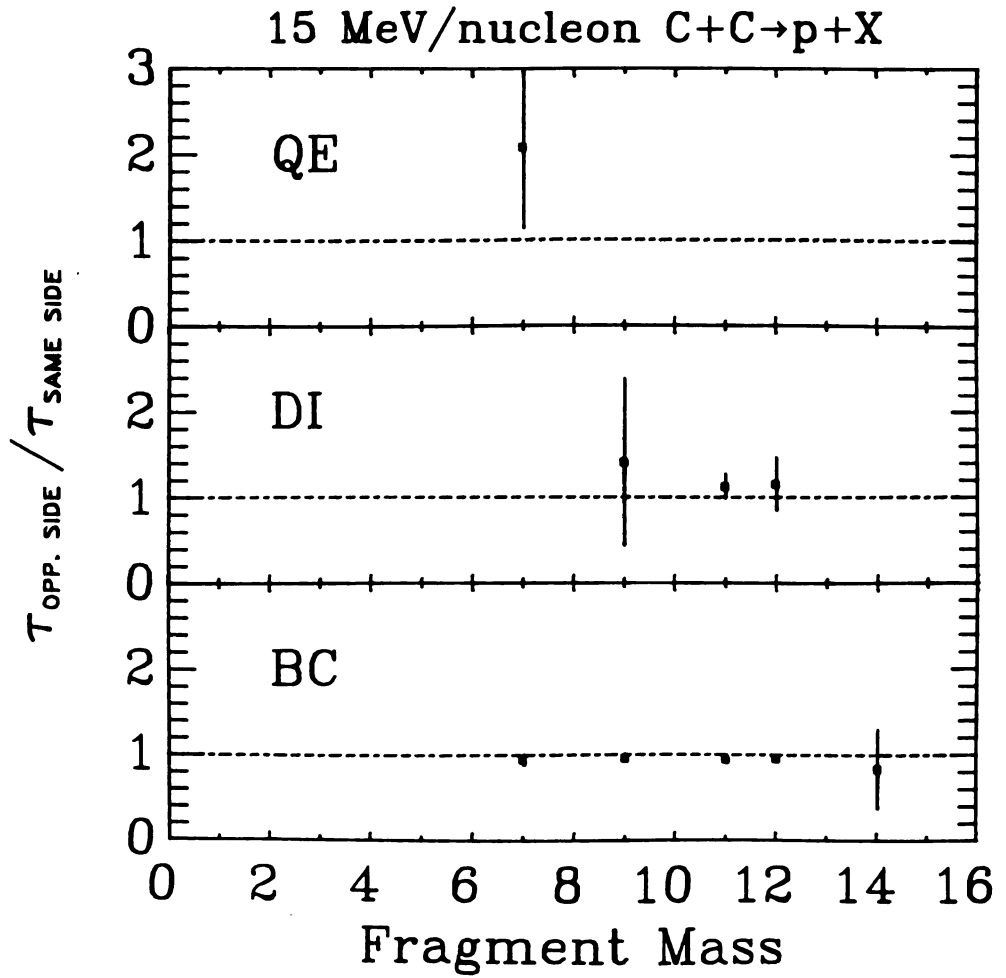


FIGURE IV-25

Ratio of opposite (HP) to same (BP) side temperatures from the moving source fits for 15 MeV/A C+C for protons.

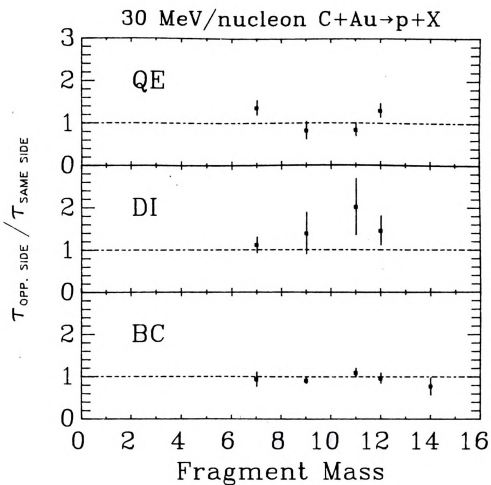


FIGURE IV-26

Ratio of opposite (HP) to same (BP) side temperatures from the moving source fits for 30 MeV/A C+Au for protons.

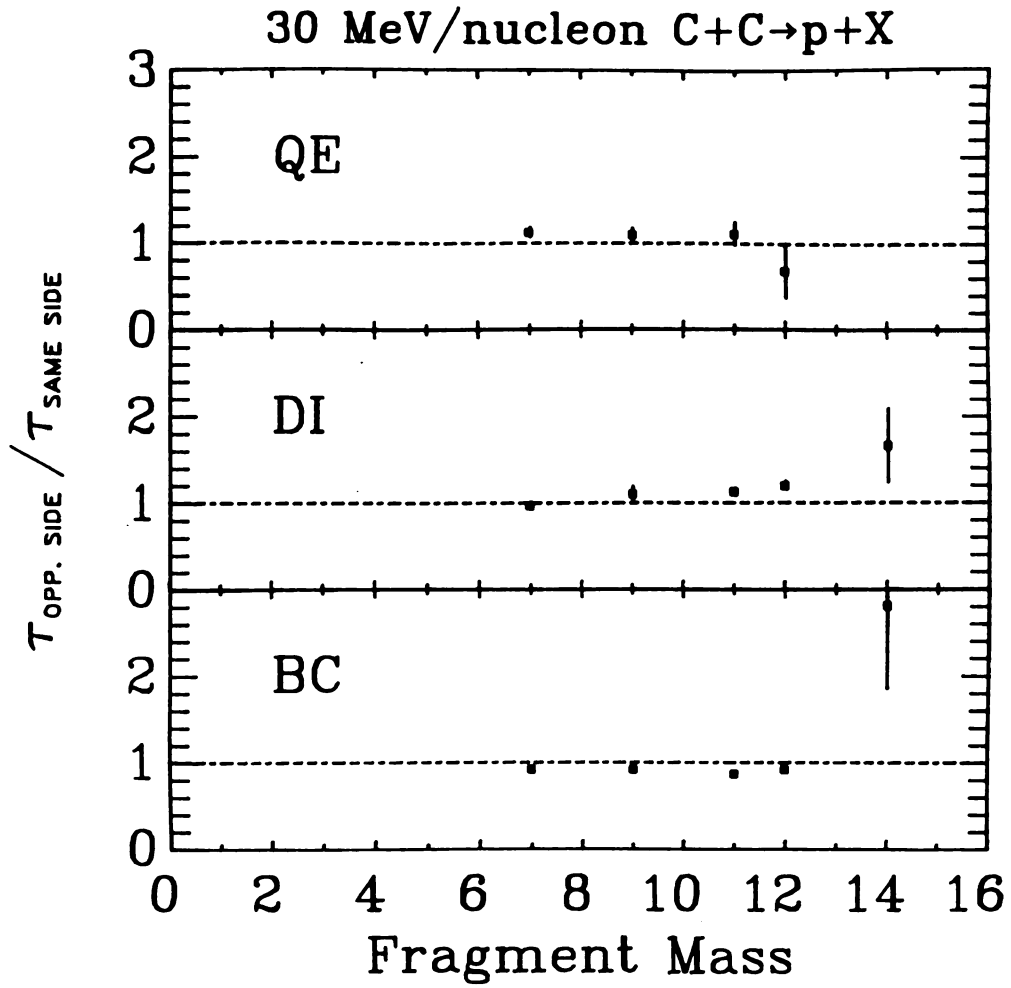


FIGURE IV-27

Ratio of opposite (HP) to same (BP) side temperatures from the moving source fits for 30 MeV/A C+C for protons.

in the moving source fit was 30 MeV/nucleon C+Au, therefore the ratios of the velocities are shown in figure IV-28. There seems to be no general trend or deviation from 1 in the ratios of the temperatures and velocities. This would indicate that the light particles come from similar sources.

A more sensitive indicator of variations is the integrated cross section. By comparing the integrated cross sections for the opposite and same sides one can now compare not only protons but almost all the light particles measured in the plastic scintillator telescopes. Figures IV-29-42 show the ratios of the integrated coincidence cross sections for the 15 and 30 MeV/nucleon C+Au,C for most of the light particles as a function of the fragment mass detected in the trigger detector. Each figure is broken up into three sections as described previously. Because of the lower cross section and the low energy cut off of the plastic scintillator, the 15 MeV/nucleon data had fewer statistics for the He isotopes and therefore not enough for coincidence cross section comparison. The lines represent the momentum conservation calculation integrated over the weighted source sizes.

For the 30 MeV/nucleon C+Au one finds very little variation from a ratio of 1, except for the protons, whereas the momentum calculation shows a marked increase in the ratio as a function of fragment mass. This trend shows the effects of momentum conservation since an increase in mass of the trigger particle would only increase the number of

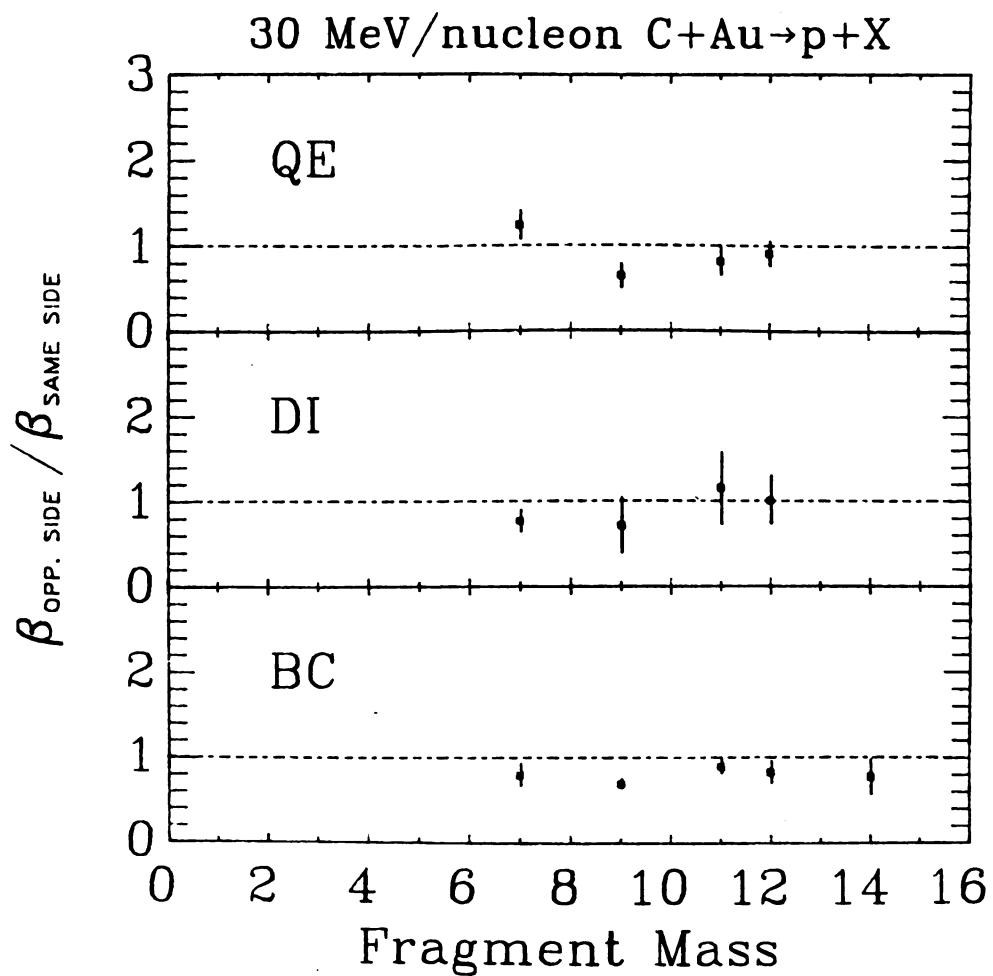


FIGURE IV-28

Ratio of opposite (HP) to same (BP) side velocities from the moving source fits for 30 MeV/A C+Au for protons.



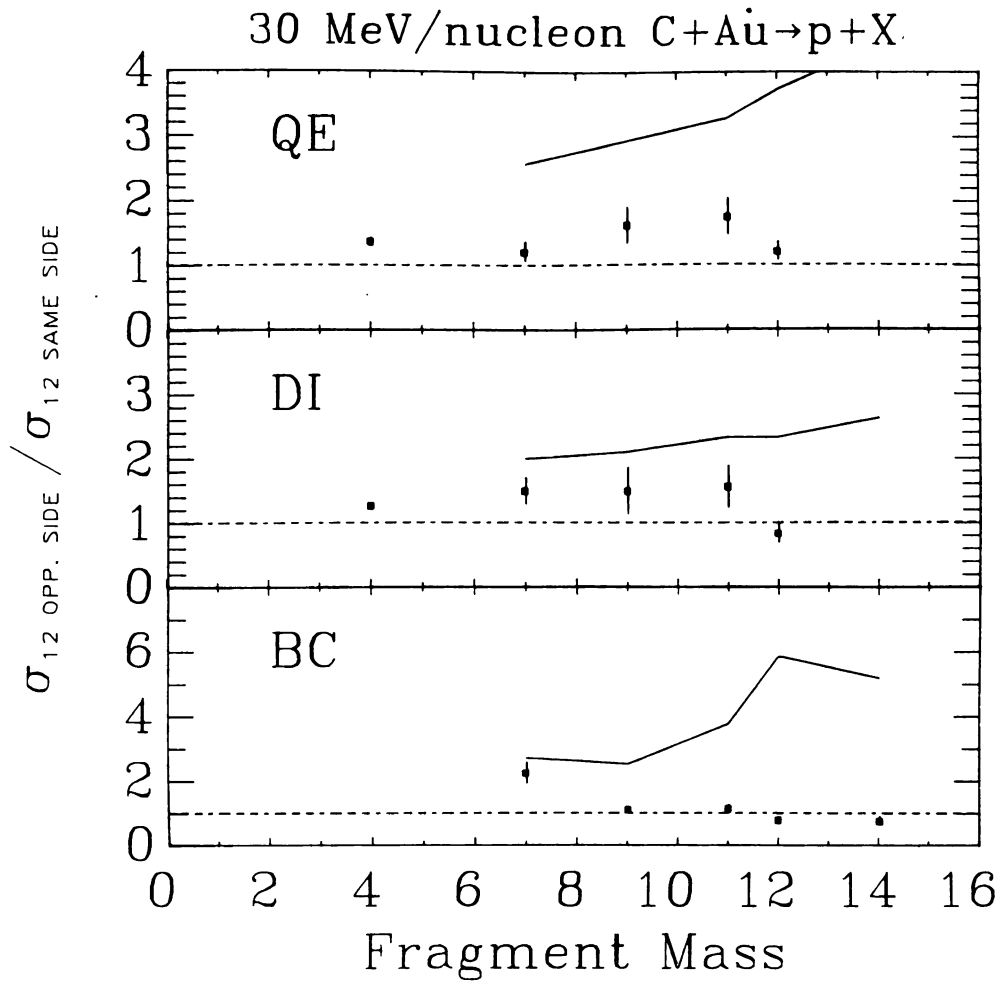


FIGURE IV-29

Ratio of opposite (HP) to same (BP) side integrated cross sections for for 30 MeV/A C+Au for protons.

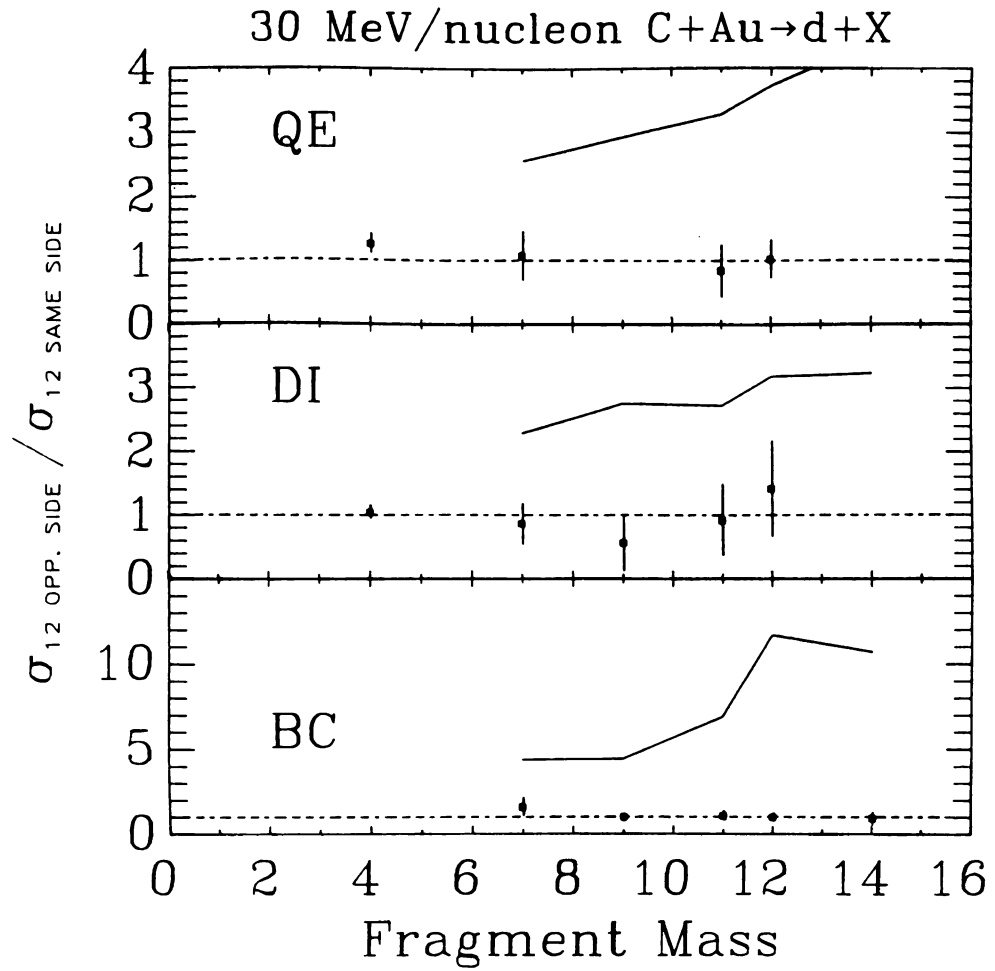


FIGURE IV-30

Ratio of opposite (HP) to same (BP) side integrated cross sections for for 30 MeV/A C+Au for deuterons.



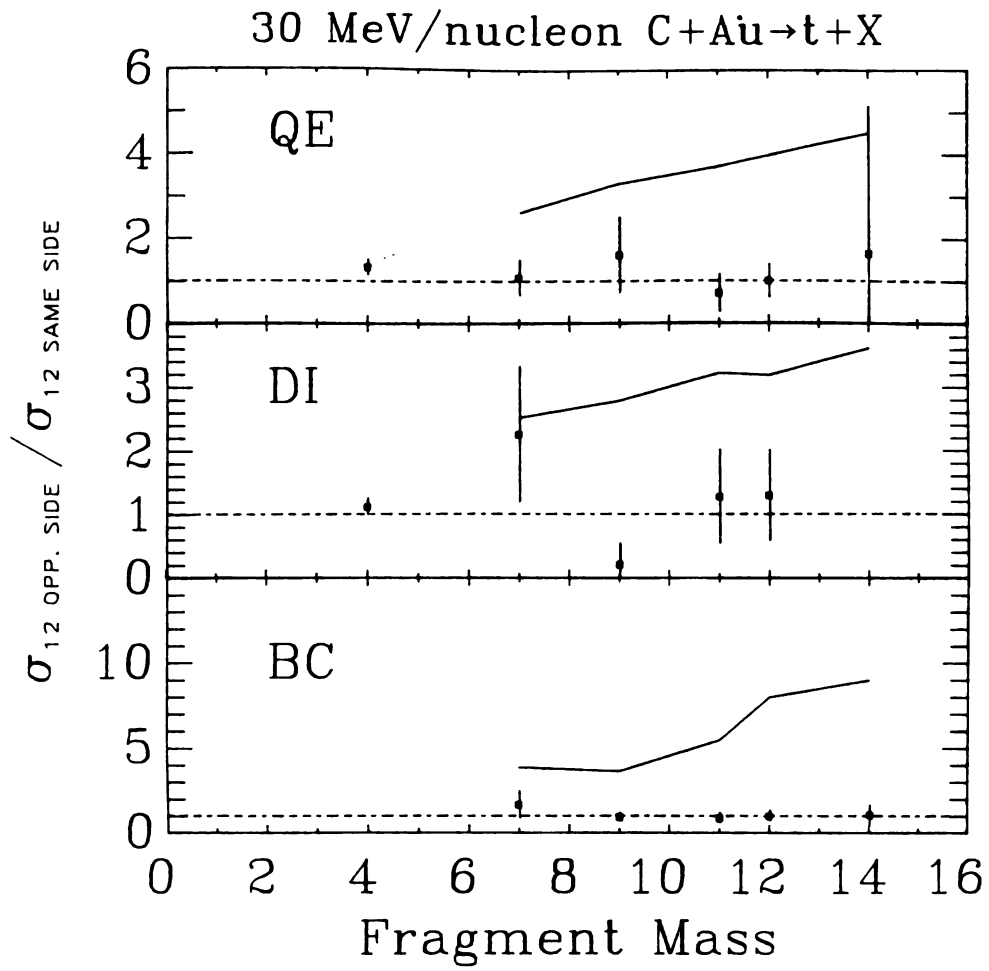


FIGURE IV-31 Ratio of opposite (HP) to same (BP) side integrated cross sections for for 30 MeV/A C+Au for tritons.

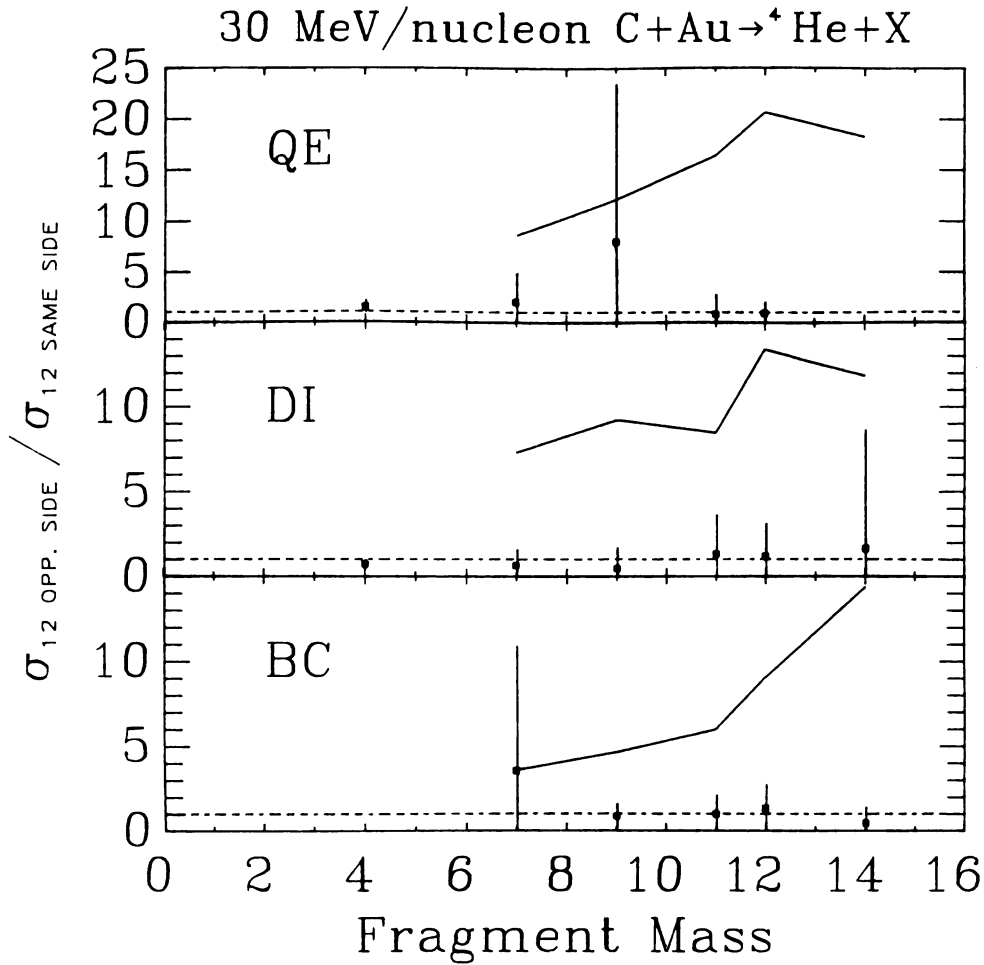


FIGURE IV-32 Ratio of opposite (HP) to same (BP) side integrated cross sections for for 30 MeV/A C+Au for ^4He .

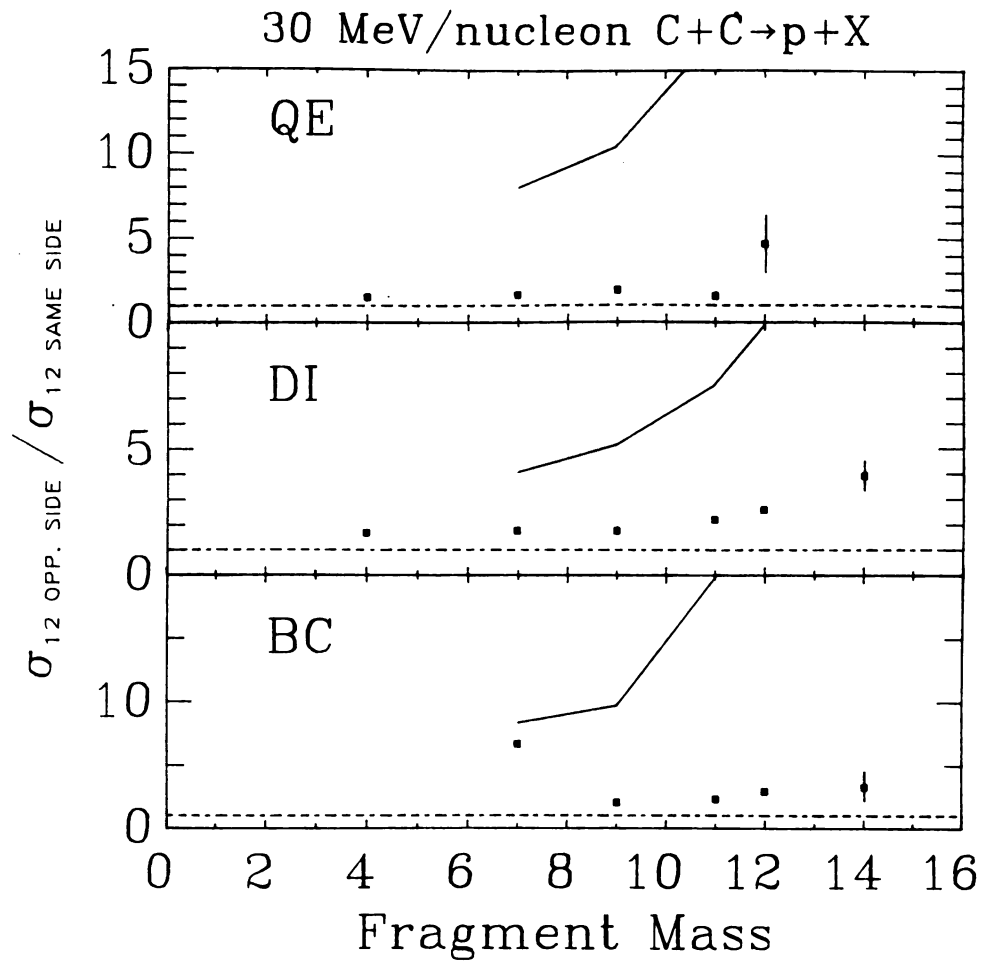


FIGURE IV-33 Ratio of opposite (HP) to same (BP) side integrated cross sections for for 30 MeV/A C+C for protons.

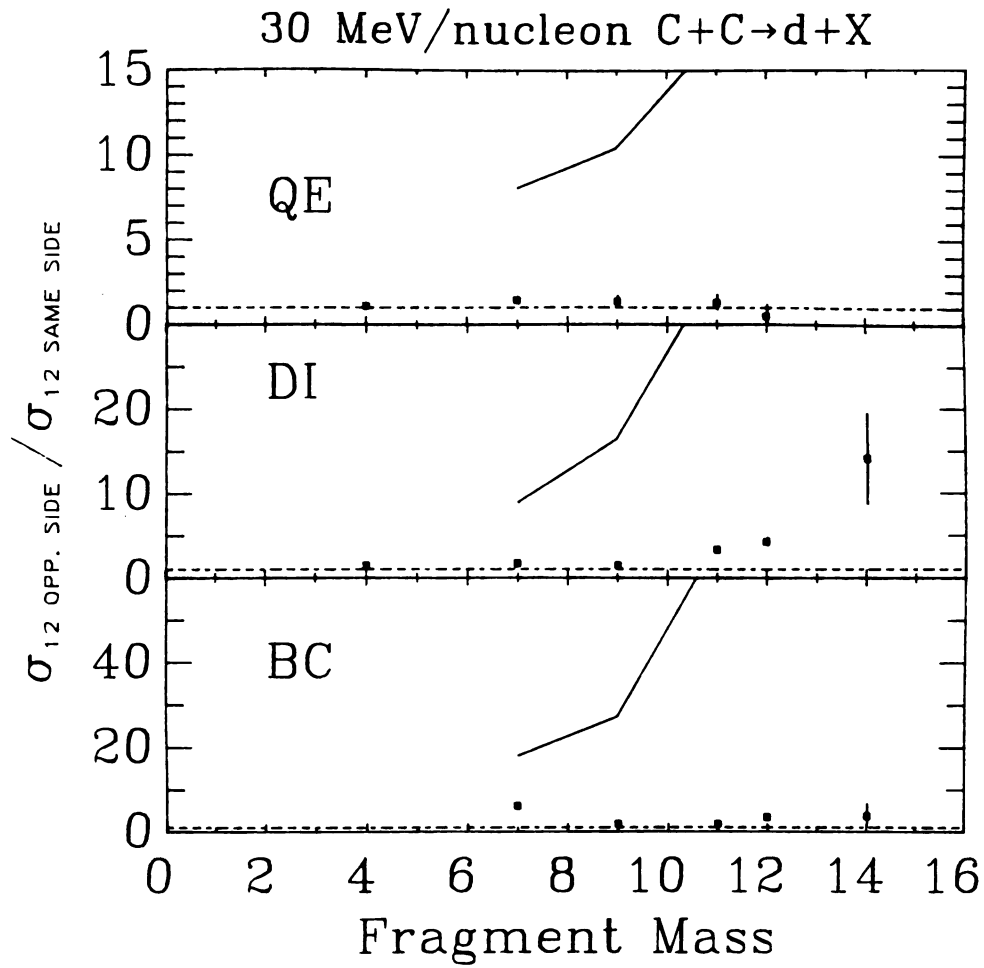


FIGURE IV-34

Ratio of opposite (HP) to same (BP) side integrated cross sections for for 30 MeV/A C+C for deuterons.

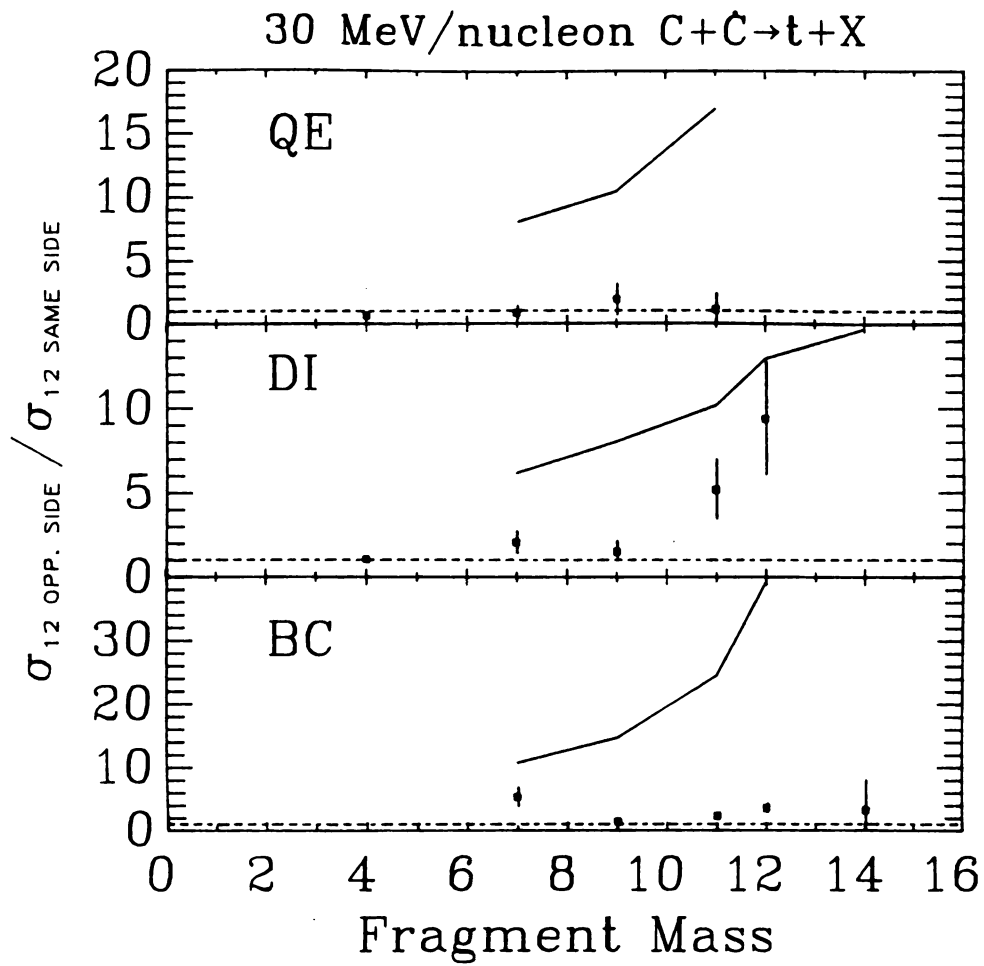


FIGURE IV-35

Ratio of opposite (HP) to same (BP) side integrated cross sections for for 30 MeV/A C+C for tritons.

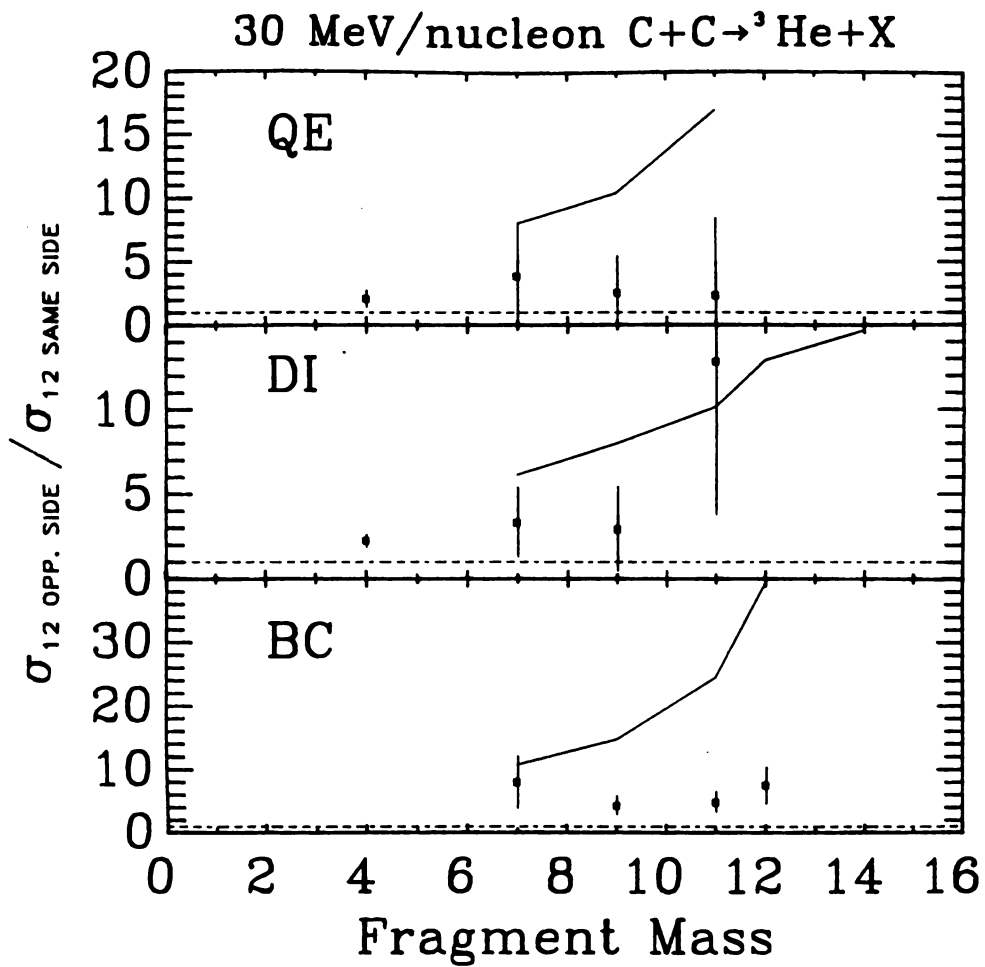


FIGURE IV-36

Ratio of opposite (HP) to same (BP) side integrated cross sections for for 30 MeV/A C+C for ³He.

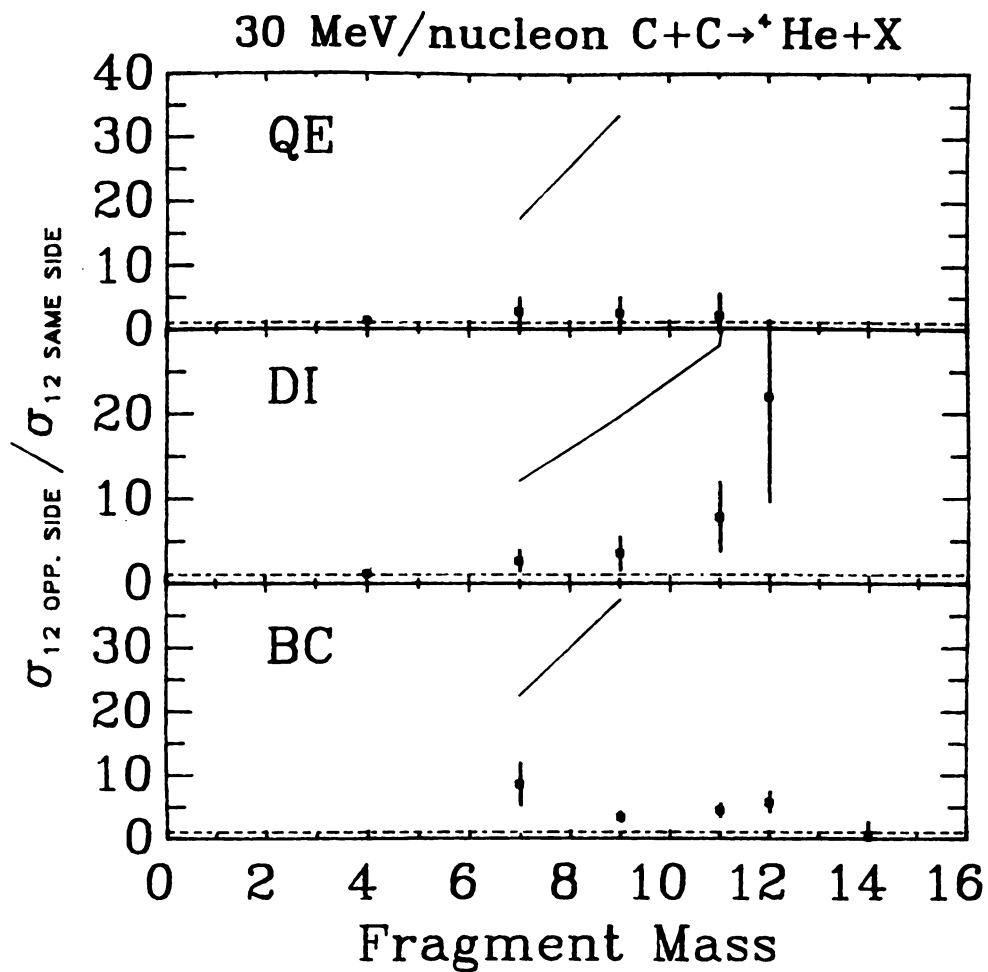


FIGURE IV-37

Ratio of opposite (HP) to same (BP) side integrated cross sections for for 30 MeV/A C+C for ⁴He.



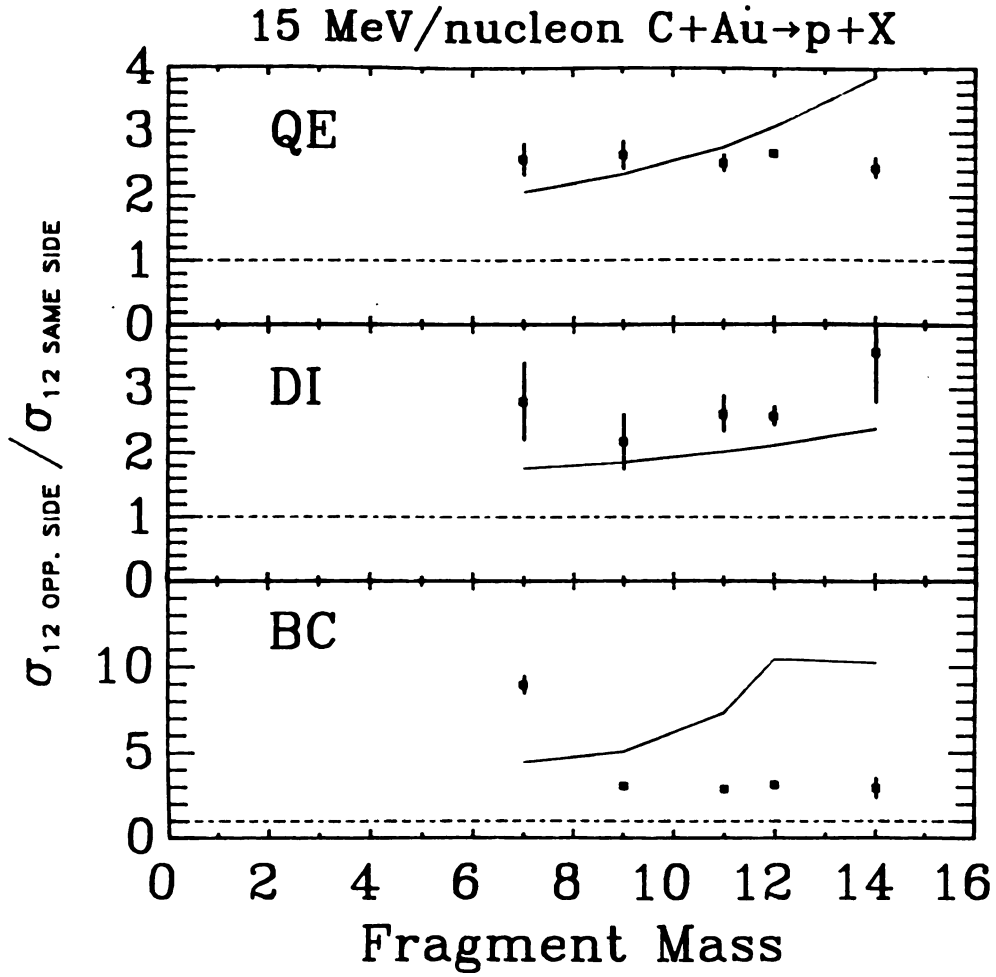


FIGURE IV-38 Ratio of opposite (HP) to same (BP) side integrated cross sections for for 15 MeV/A C+Au for protons.

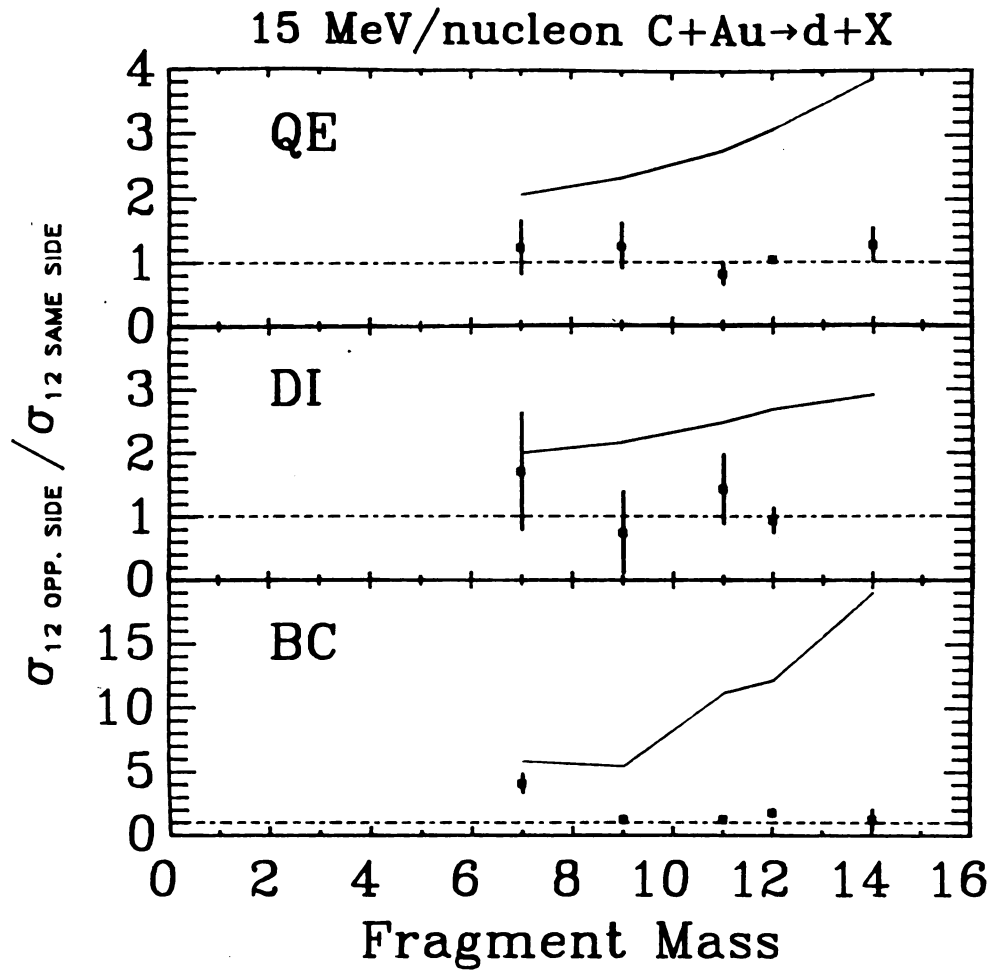


FIGURE IV-39 Ratio of opposite (HP) to same (BP) side integrated cross sections for for 15 MeV/A C+Au for deuterons.

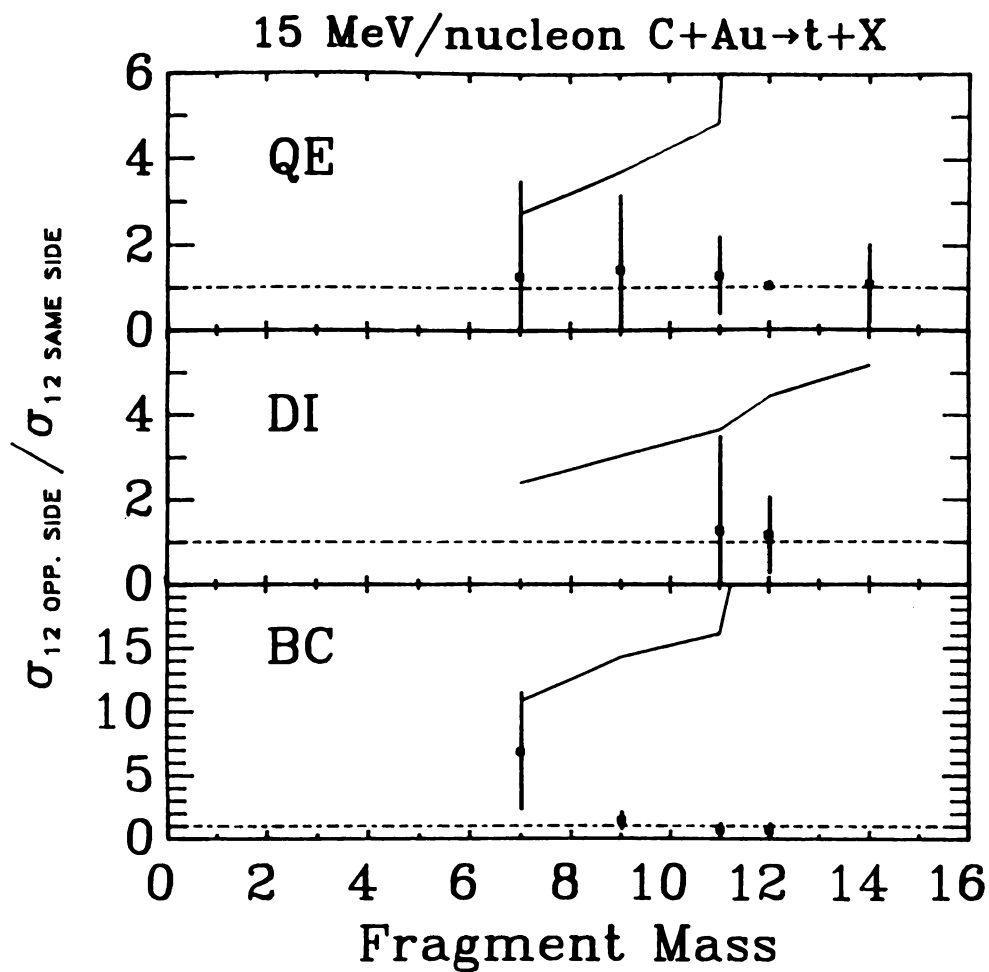


FIGURE IV-40 Ratio of opposite (HP) to same (BP) side integrated cross sections for for 15 MeV/A C+Au for tritons.

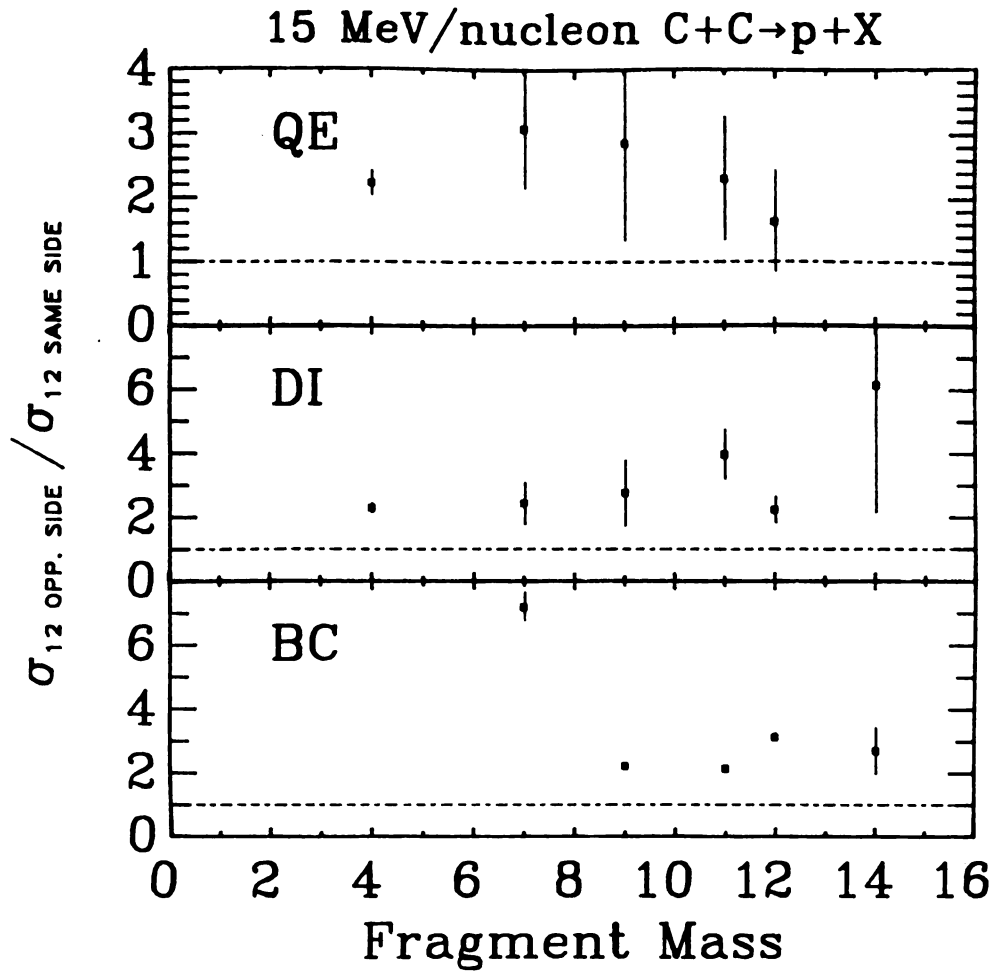


FIGURE IV-41

Ratio of opposite (HP) to same (BP) side integrated cross sections for 15 MeV/A C+C for protons.

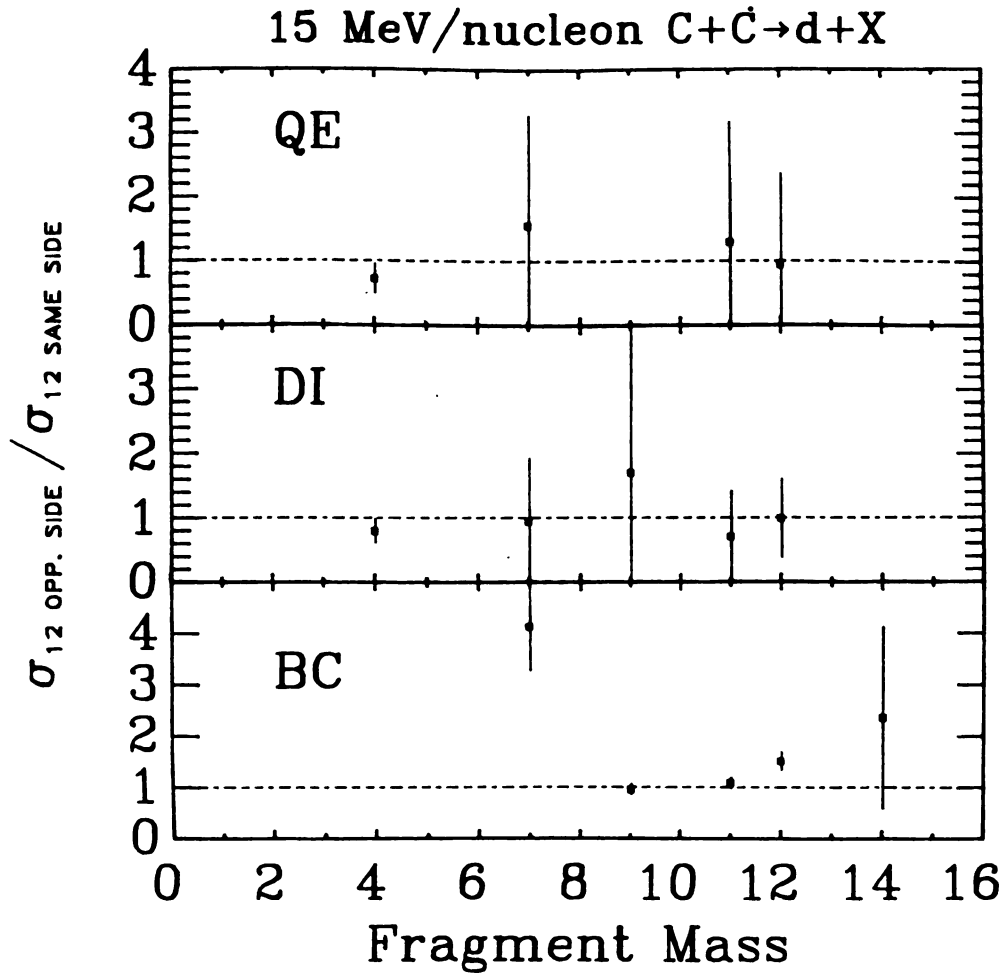


FIGURE IV-42

Ratio of opposite (HP) to same (BP) side integrated cross sections for for 15 MeV/A C+C for deuterons.

light particles emitted on the opposite side in order to balance momentum. This difference is most noticeable with the light particles in coincidence with the BCS. Differences between the opposite and same side cross sections in the calculations can be as much as 10 to 15 times, whereas the data does not reflect this sort of difference. Differences between the data and momentum conservation calculations seem to increase with increasing light particle mass for not only the BCS but also for the QE and DI part of the PLF trigger.

One certainly would not expect to find any real variations for the light particles in coincidence with the deep-inelastic part of the PLF spectra because of the thermal origin of these fragments. It is although, surprising to not find any variations in the light particles in coincidence with the quasi-elastic part of the PLF spectra. One would expect to find some momentum conservation effects which would enhance some differences. The data differ from what Caskey et al. [Ca 85] found with 35 MeV/nucleon N+Ho for which neutrons were measured from 10 to 135 degrees in coincidence with the quasi-elastic part of the PLF spectra at 10 degrees. They found an enhancement of the neutrons on the same side as compared to the opposite side for neutrons measured at 10°, whereas for neutrons measured at 60°, the opposite side of the PLF detector had an enhancement of neutrons. In another experiment it was

observed that this enhancement was not as prominent when the PLF detector was at 15 degrees [Re 85].

The 30 MeV/nucleon C+C data definitely show a somewhat higher value than 1 for the opposite to same side ratio, especially for the protons. Yet the momentum conservation calculation can at times be as much as 10 times larger than the data. The light particle - deep inelastic ratios show a marked increase with fragment mass. This increase, although not as large as the momentum conservation calculation, shows the effects of a single emitting source for the two particles. The protons in coincidence with the quasi-elastic part of the PLF do not show this same effect. This can be interpreted in terms of the amount of interaction between the projectile and target. The QE mechanism is associated with large impact parameters with a limited interaction with the target. The DI part of the PLF spectra is associated with smaller impact parameters. Collective and dynamic effects associated with strong target interactions is observed in the proton - DI coincidence integrated cross section ratios by its enhancement of the opposite side and the similar trend as the calculation. The momentum calculation in fact, predicts that there is not enough energy to emit both particles in some cases. This is because of the smaller source sizes associated with C+C reactions. These cases include protons in coincidence with the QE particles above a mass of 9, deuterons in coincidence all QE particles and tritons in coincidence with all the

trigger particles. The calculation predicts the helium isotopes to be in coincidence with all the trigger particles because of a coulomb repulsion term in the calculation.

The momentum conservation calculation consistently predicts a much higher ratio. A single source size with even the maximum number of nucleons for the C+C reaction (24) does not even come close to the data, as was shown previously. This disagreement would indicate that the two coincident particles do not come from a single thermalized source. The fact that there is some target mass dependence with an enhancement of the opposite side for carbon but not for the gold target and that the two coincident particles do not come from a single thermal source would suggest that some form of a collective, dynamic effect is being observed. The target dependence would be expected for a collective effect especially if the trigger is the bragg curve detector in which the intermediate mass fragment is emitted from the carbon target but not as easily from the gold target. The target mass dependence could be interpreted as some form of shadowing which would increase the emission of light particles on the opposite side. In addition, the BC - light particle coincidence reactions can be associated with very gentle and peripheral reactions for the C+C data. This is observed in the enhancement of the opposite to same side ratios for the C+C data, whereas the C+Au data indicates an almost isotropic emission for the BC data.

Collective, dynamic effects would certainly be a function of the incident energy of the projectile. We would expect the effects to be larger for the 30 MeV/nucleon C+Au,C than for the 15 MeV/nucleon data. On the other hand, the 15 MeV/nucleon C+Au data for the coincident protons show an even larger enhancement of the ratios than for the 30 MeV/nucleon C+Au data, even more so than the momentum conservation calculation, yet the BCS trigger calculation now seems to agree with the data except for the Li point. This could be explained by the lower energy/nucleon in the emitting source, which in turn could mean a lower multiplicity for the reaction. This would mean that these fewer particles emitted would carry away more information about the momentum conservation of the reaction, which in turn would mean an enhancement of the opposite to same side ratio. The deuterons and tritons still have data points around 1 yet the calculations show a larger ratio.

The small source sizes and low excitation energy of the 15 MeV/nucleon C+C reactions causes the momentum conservation calculation to not even predict the emission of both a light particle and either an intermediate mass or projectile like fragment. This in itself should preclude any coincident emission from a single thermalized source. The data seems to show an opposite side enhancement for the 15 MeV/nucleon C+C protons, yet little recognizable enhancement for the deuterons.

CHAPTER V

SUMMARY AND CONCLUSIONS

A. SUMMARY OF RESULTS

A Bragg curve spectrometer - plastic scintillator array was developed for this experiment and as a prototype subarray for a 4π detector [We 85]. The unique ability of this detector to measure light particles and complex fragments at the same angle made it indispensable for measuring opposite and same side coincident events. The recent development of slow plastic scintillator by Bicron (BC 444) has eliminated the need to use CaF_2 as the ΔE element, which had limited the low energy range of the telescopes. The Bragg curve spectrometer was shown to successfully detect and identify target-like velocity fragments. The dynamic range of the detector can be extended by using it as an ion chamber for a ΔE signal and the plastic scintillator as the E signal. The close-packed scintillator arrays have been shown to successfully identify light particles in each of the telescopes which have been optically isolated with a minimum of space between them.

The emission of light particles in coincidence with projectile-like and target-like fragments has been studied in ^{12}C -induced reactions on C and Au at 15 and 30 MeV/nucleon. The inclusive light particle double differential cross sections were also obtained. The light

particle spectra were found to smoothly fall off exponentially with energy. All of the light particle spectra could be described by a single moving source characterized by a Boltzmann distribution in a moving frame. The observed particles arise from a source moving with a velocity intermediate between that of the target and of the projectile which was found to be consistent with previous work [Ha 85]. The parameters describing the light particles intermediate velocity source were extracted and temperatures and velocities were studied. The ratios of the coincidence to inclusive-light-particle temperature parameter were studied as a function of the mass of the coincident complex fragment. The extracted source parameter was found to be relatively independent of the mass of the emitted coincident fragment, suggesting that they are all emitted from a common thermal source.

Light particles, at $\pm 45^\circ$, were in coincidence with complex fragments at 15° and 45° . The complex fragments measured at 15° ($2 \leq Z \leq 7$) were thought to be projectile-like fragments and low and high energy cuts were applied to separate the deep-inelastic and quasi-elastic parts, respectively. The fragments measured at 45° were detected in the Bragg Curve Spectrometer and were slow moving target-like velocity fragments ($3 \leq Z \leq 7$). The opposite to same side ratios for the extracted temperature parameters show almost no enhancement or trends suggesting again that the light particles are emitted from the same thermal source. This

effect is also observed for the ratio of the velocities for the 30 MeV/nucleon C+Au data.

Integrating the cross section over energy allows one to have a more accurate and quantitative comparison of opposite to same side effects and it also allows one to use light particles other than protons by summing all the available statistics. The 30 MeV/nucleon C+Au showed no general enhancement of the opposite side or trends, except for some slight enhancement of the protons for the quasi-elastic and deep-inelastic cross sections. The C+C data at 30 MeV/nucleon show a general enhancement of the opposite side for the light particles in coincidence with the Bragg Curve detector. The light particles in coincidence with the deep-inelastic part of the PLF spectra show an enhancement of the opposite side with a definite increase with fragment mass. The protons show a slight enhancement for the opposite side for the quasi-elastic but have a ratio of about 1 for all the other light particles.

The momentum conservation calculations, shown by the solid lines, is an extreme simplification in order to compare to the data. At these energies one does not expect to find a separate participant region or even a localized thermal source or "hot spot". Mean field effects are expected to have a large contribution to the dynamics of these reactions. Evidence for thermalization in intermediate energy nucleus-nucleus collisions have been observed in inclusive light particle and complex fragment

spectra, light particle - complex fragment correlation measurements and p-p correlation results [Fo 85, Wes 85]. Because of the simplification of the momentum conservation calculation, one might argue that a comparison to the data is not a very useful one. Awes et al. [Aw 83] used a Monte Carlo calculation, for a semi-analytical approach to the distribution of the particles, to determine the momentum conservation and other kinematic correlation effects on a coincidence experiment. This type of calculation would show all of the correlation effects due to the conservation of energy, momentum, charge, and baryon number. This would allow one to show that the kinematic effects of a certain reaction mechanism are minimal or at least well understood before associating structures in the correlation functions with dynamic effects.

The only set of data that seem to follow the general trend of the momentum conservation calculations, in which the opposite to same side ratio increases with fragment mass, are the 30 MeV/nucleon C+C ratios in coincidence with the deep-inelastic part of the projectile-like fragments. The 15 MeV/nucleon C data had much fewer statistics and therefore more difficult to observe any trends. The same enhancement of the opposite side is seen for the protons for both the Au and C targets. Whereas for the other light particles the ratios are about 1. The momentum conservation calculation does show some agreement for the coincident protons in the 15 MeV/nucleon C+Au ratios.

B. CONCLUSIONS

We have seen that the complex fragments as well as the light particles are emitted from a thermalized subsystem of the projectile and target, yet on the other hand the simple single source model is inadequate at these energies because the reaction was shown to allow the exchange of energy and momentum between the participant and spectators. These ratios can not be explained solely by momentum conservation from a single source.

Momentum conservation effects should be a function of the impact parameter. This effect is seen most clearly when comparing the 30 MeV/nucleon C+C light particle integrated cross section ratios of the DI part of the PLF spectra with the QE part. The QE part is usually associated with larger impact parameters than the DI part. The smaller impact parameter of the DI part of PLF spectra show the collective effects most clearly, with its increase of opposite side enhancement as function of fragment mass. Whereas the light particles in coincidence with the QE part of the PLF spectra show almost no enhancement of the opposite side. This could be associated with the highly inelastic bounce-off effect of hydrodynamics [St 80]. This model predicts that for collisions which are not head-on, the incident projectile is inelastically scattered from the target nucleus into the $\phi=0^\circ$ side of the reaction plane and then decays by emission of light particles. The light particles are focussed in the direction of the scattered projectile due to its relatively

high velocity. These light particles were in fact not measured in these experiments. The target nucleus is also excited and decays by emission of light particles while slowly recoiling into the $\phi=180^\circ$ side of the reaction plane. These spectra were measured and are characteristic of emission from a stationary or low velocity source.

The relatively low multiplicity of protons, $\approx 2/\text{collision}$ [We 84], at 30 MeV/nucleon would lead one to suspect a strong direct or "knock-out" component in light particle emission. Fox et al. [Fo 85] have shown that the in- to out-of-plane ratios for p-p large angle correlations had no peak at quasi-elastic angles for 40 MeV/nucleon $^{12}\text{C}+\text{C}$, whereas peaks corresponding to the quasi-elastic nucleon-nucleon scattering were seen for 800 MeV/nucleon [Ta 80] and 85 MeV/nucleon [Car 85] $^{12}\text{C}+\text{C}$. The correlation between other light particles increases with the mass of the observed particles, as was seen for the 85 MeV/nucleon data. These correlations were not able to be described by the same momentum conservation calculation as was used in this thesis. A VUU calculation [Kr 85], which is based on a cascade calculation with a mean field effect included, was able to reproduce the p-p correlations. This agreement indicates the importance of the mean field effect at these energies.

There appears to be some target mass dependence. This dependence is seen in the 30 MeV/nucleon C+Au data as compared to the C+C data. The C+Au data shows a definite

lack of opposite side enhancement of the coincident light particles for all the different trigger types and fragments, whereas the C+C data shows the enhancement. This difference may be interpreted in terms of the larger mass target dissipating the momentum transferred to it by the projectile or in other words some form of shadowing. This effect has in fact been seen previously for 800 MeV/nucleon C+C,Pb [Ta 80].

The two competing effects of shadowing and momentum conservation can have opposite results. The first favoring same side emission and the second opposite side emission. As pointed out by Tsang et al. [Ts 84], the absorption effects of shadowing are expected to be more pronounced for the emission of composite light particles as compared to the emission of protons. This could explain why the proton coincident ratios for all cases showed an enhancement of the opposite side, whereas the other light particles did not.

This thesis has shown effects of thermalization in the emission of light particles in coincidence with complex fragments which along with other information about intermediate energy heavy ion reactions, fill in some of the missing pieces about fully understanding the reaction dynamics.

The next generation of experiments will use a 4π logarithmic detector in order to totally reconstruct the events [We 85]. This detector will be able to detect light particles ($A \leq 4$), medium mass nuclear fragments ($A \leq 40$),

fission fragments, and projectile-like fragments resulting from these intermediate energy collisions.

LIST OF REFERENCES

REFERENCES

A

- [Am 75] A.A. Amsden, G.F. Bertsch, F.H. Harlow and J.R. Nix, Phys. Rev. Lett. 35(1975)905.
- [An 85] S.P. Angius, Michigan State University NSCL Annual Report 84-85 (1985).
- [As 82] J.M. Asselineau, J. Duchon, M.L. Haridon, P. Mosrin, R. Regimbart and B. Tamain, Nucl. Instr. Meth. 204(1982)109.
- [Aw 81] T.C. Awes, G. Poggi, C.K. Gelbke, B.B. Back, B.G. Glagola, H. Breuer and V.E. Viola, Jr., Phys. Rev. C24(1981)89.
- [Au 83] R. Au, W. Benenson, R. Fox and D. Notman, IEEE Nucl. Sci. NS30-5(1983)3808.

B

- [Ba 75] H.G. Baumgardt, T.U. Schott, T. Sakamoto, E. Schopper, H. Stöcker, J. Hofmann, W. Scheid and W. Greiner, Z. Phys. A273(1975)359.
- [Be 76] H.W. Bertini, R.T. Santoro and O.W. Hermann, Phys. Rev. C14(1976)590.
- [Bh 79] R.K. Bhowmik, E.C. Pollacco, N.E. Sanderson, J.B.A. England and G.C. Morrison, Phys. Rev. Lett. 43(1979)619.
- [Bi 67] J.B. Birks, Theory and Practice of Scintillation Counting (Pergamon Press, London 1967)p.100.
- [Bo 84] D.H. Boal, Advances in Nuclear Physics, J.W. Negele and E. Vogt, editors 1984.
- [Bu 81] G. Buchwald, L.P. Csernai, J.A. Maruhn, W. Greiner and H. Stöcker, Phys. Rev. C24(1981)135.
- [Bu 83] G. Buchwald, G. Graebner, J. Theis, J.A. Maruhn, W. Greiner and H. Stöcker, Phys. Rev. C28(1983)1119.
- [Bu 84] G. Buchwald, G. Graebner, J. Theis, J. Maruhn, W. Greiner and H. Stöcker, Phys. Rev. Lett. 52(1984)1594.

C

- [Ca 85] G. Caskey, A. Galonsky, B. Remington, M.B. Tsang, C.K. Gelbke, A. Kiss, F. Deak, Z. Seres, J.J. Kolata, J. Hinnefeld and J. Kasagi, Phys. Rev. C31(1985)1597.
- [Car 85] L. Carlen, H.A. Gutafsson, B. Jakobsson, A. Kristiansson, P. Kristiansson, A. Oskarsson, H. Ryde, M. Westenius et. al., Proceedings of the Second International Conference on Nucleus-Nucleus Collisions, Ed. B. Jakobsson and K. Aleklett, 158(1985).
- [Ch 85] C.B. Chitwood, J. Aichelin, D.H. Boal, G. Bertsch, D.J. Fields, C.K. Gelbke, W.G. Lynch, M.B. Tsang, J.C. Shillcock, T.C. Awes, R.L. Ferguson, F.E. Obenshain, F. Plasil, R.L. Robinson and G.R. Young, Phys. Rev. Lett. 54(1985)302.
- [Cu 82] J. Cugnon, D. Kinet and J. Vandermeulen, Nucl. Phys. A379(1982)553.

D

- [Da 81] S. DasGupta and A. Mekjian, Phys. Reports 72C(1981)133.

F

- [Fi 84] D.J. Fields, W.G. Lynch, C.B. Chitwood, C.K. Gelbke, M.B. Tsang, H. Utsunomiya and J. Aichelin, Phys. Rev. C30(1984)1912.
- [Fo 85] D. Fox, D.A. Cebra, Z.M. Koenig, J.J. Molitoris, P. Ugorowski, H. Stöcker and G.D. Westfall, Michigan State University preprint MSUCL-534(1985).
- [Fr 83] W.A. Friedman and W.G. Lynch, Phys. Rev. C28(1983)16.
- [Fu 79] H.W. Fulbright, Nucl. Instr. Meth. 162(1979)21.

G

- [Ga 80] S.I.A. Garpman, S.K. Samadder, D. Sperber and M. Zielinskapfabe, Phys. Lett. 92B(1980)56.
- [Go 77] J. Gosset, H.H. Gutbrod, W.G. Meyers, A.M. Poskanzer, A. Sandoval, R. Stock and G.D. Westfall, Phys. Rev. C16(1977)629.

- [Go 78] A.S. Goldhaber, Phys. Rev. C17(1978)2243
- [Gos 78] J. Gosset, J.I. Kapusta and G.D. Westfall, Phys. Rev. C18(1978)844.
- [Go 79] P.A. Gottschalk and M. Weström, Nucl. Phys. A314(1979)232.
- [Gr 82] C.R. Gruhn, M. Bimini, R. Legrain, R. Loveman, W. Pang, M. Roach, D.K. Scott, A. Shotter, T.J.M. Symons, J. Wouters, M. Zisman, R. DeVries, Y.C. Peng and W. Sondheim, Nucl. Instr. Meth. 196(1982)33.
- [Gu 76] H.H. Gutbrod, A. Sanddoyal, P.J. Johansen, A.M. Poskanzer, J. Gosset, W.G. Meyer, G.D. Westfall and R. Stock, Phys. Rev. Lett. 37(1976)667.
- [Gu 83] H.H. Gutbrod, H. Loher, A.M. Poskanzer, T. Renner, H. Riedesel, H.G. Ritter, A. Warwick, F. weik and H. Wieman, Nucl. Phys. A400(1983)343c.
- [Gu 84] H.A. Gustafsson, H.H. Gutbrod, B. Kolb, H. Lohner, B. Ludewigt, A.M. Poskanzer, T. Renner, H. Riedesel, H.G. Ritter, A. Warwick, F. Weik and H. Wieman, Phys. Rev. Lett. 52(1984)1590.

H

- [Ha 52] W. Hauser and H. Feshbach, Phys. Rev. 87(1952)366.
- [Ha 79] R.L. Hatch and S.E. Koonin, Phys. Lett. 81B(1979)1.
- [Ha 85] B.E. Hasselquist, G.M. Crawley, B.V. Jacak, Z.M. Koenig, G.D. Westfall, J.E. Yurkon, R.S. Tickle, J.P. DuFour and T.J.M. Symons, Phys. Rev. C32(1985)145.
- [Ho 80] H. Ho, P. Gonthier, M.N. Namboodiri, J.B. Natowitz, L. Adler, S. Simon, K. Hagel, R. Terry and A. Khodai, Phys. Lett. 96B(1980)51.

J

- [Ja 83] B.V. Jacak, G.D. Westfall, C.K. Gelbke, L.H. Harwood, W.G. Lynch, D.K. Scott, H. Stöcker, M.B. Tsang and T.J.M. Symons, Phys. Rev. Lett. 51(1983)1846.
- [Ja 84] B.V. Jacak, Ph.D. thesis, Michigan State University 1984.

K

- [Ka 77] J.I. Kapusta, Phys. Rev. C16(1977)1493.
- [Ko 77] S.E. Koonin, Phys. Rev. Lett. 39(1977)680.
- [Kr 85] H. Kruse, B.V. Jacak, J.J. Molitoris, G.D. Westfall and H. Stöcker, Phys. Rev. C31(1985)1770.

L

- [Ly 82] W.G. Lynch, L.W. Richardson, M.B. Tsang, R.E. Ellis, C.K. Gelbke and R.E. Warner, Phys. Lett. 108B(1982)274.

M

- [Mc 84] R.J. McDonald, L.G. Sobotka, Z.Q. Yao, G.J. Wozniak and G. Guarino, Nucl. Instr. Meth. 219(1984)508.
- [Me 69] D.F. Measday and C. Richard-Serre, Nucl. Instr. Meth. 76(1969)45.

P

- [Pa 84] Particle Data Group, Rev Mod. Phys. 56(1981)153.
- [Pe 68] R.H. Pehl, F.S. Goulding, D.A. Landis and M. Lenzlinger, Nucl. Instr. Meth. 59(1968)45.
- [Po 85] J. Pochodzalla, W.A. Friedman, C.K. Gelbke, W.G. Lynch, M. Maier, D. Ardouin, H. Delagrange, H. Doubre, C. Gregoire, A. Kyanowski, W. Mittig, A. Peghaire, J. Peter, F. Saint-Laurent, Y.P. Viyogi, B. Zwieglinski, G. Bizard, F. Lefebvres, B. Tamain and J. Quebert, Phys. Rev. Lett. 55(1985)177.

R

- [Re 85] B. Remington, private communication (1985).

S

- [Sa 83] A. Sandoval, R. Bock, R. Brockmann, A. Dacal, J.W. Harris, M. Maier, M.E. Ortiz, H.G. Pugh, W. Rauch, R.E. Renfordt, F. Riess, L.S. Schroeder, R. Stock, H. Strobele and K.L. Wolf, Nucl. Phys. A400(1983)365c.

- [Sc 81] D.K. Scott, Nucl. Phys. A354(1981)375c.
- [Sc 82] Ch. Schiessl, W. Wagner, K. Hartel, P. Kienle, H.J. Korner, W. Mayer and K.E. Rehm, Nucl. Instr. Meth. 192(1982)291.
- [So 75] M.I. Sobel, P.J. Siemens, J.P. Bondorf and H.A. Bethe, Nucl. Phys. A251(1975)502.
- [St 80] H. Stöcker, J.A. Maruhn and W. Greiner, Phys. Rev. Lett. 44(1980)725.
- [St 81] N. Stelte and R. Weiner, Phys. Lett. 103B(1981)275.
- [St 83] H. Stöcker, G. Buchwald, G. Graebner, P. Subramanian, J.A. Maruhn, W. Greiner, B.V. Jacak and G.D. Westfall, Nucl. Phys. A400(1983)63c.
- [Su 81] P.R. Subramanian, L.P. Csernai, H. Stöcker, J.A. Maruhn, W. Greiner and H. Kruse, J. of Phys. G7(1981)L1241.

T

- [Ta 80] I. Tanihata, M.C. Lemaire, S. Nagamiya and S. Schnetzer, Phys. Lett. 97B(1980)363.
- [To 83] V.D. Toneev and K.K. Gudima, Nucl. Phys. A400(1983)173.
- [Ts 74] Y.S. Tsai, Rev. Mod. Phys. 46(1974)815.
- [Ts 84] M.B. Tsang, W.G. Lynch, C.B. Chitwood, D.J. Fields, D.R. Klesch, C.K. Gelbke, G.R. Young, T.C. Awes, R.L. Ferguson, F.E. Obenshain, F. Plasil and R.L. Robinson, Phys. Lett. 148B(1984)265.

W

- [We 76] G.D. Westfall, J. Gosset, P.J. Johansen, A.M. Poskanzer, W.G. Meyer, H.H. Gutbrod, A. Sandoval and R. Stock, Phys. Rev. Lett. 37(1976)1202.
- [We 82] G.D. Westfall, B.V. Jacak, N. Anantaraman, M.W. Curtin, G.M. Crawley, C.K. Gelbke, B.E. Hasselquist, W.G. Lynch, D.K. Scott, M.B. Tsang, M.J. Murphy, T.J.M. Symons, R. Legrain and T.J. Majors, Phys. Lett. 116B(1982)118.
- [We 83] G.D. Westfall, Phys. Scr. T5(1983)103

- [We 84] G.D. Westfall, Z.M. Koenig, B.V. Jacak, L.H. Harwood, G.M. Crawley, M.W. Curtin, C.K. Gelbke, B.E. Hasselquist, W.G. Lynch, A.D. Panagiotou, D.K. Scott, H. Stöcker and M.B. Tsang, Phys. Rev. C29(1984)861.
- [We 85] G.D. Westfall, J.E. Yurkon, J. Van Der Plicht, Z.M. Koenig, B.V. Jacak, R. Fox, G.M. Crawley, M.R. Maier and B.E. Hasselquist, Nucl. Instr. Meth. A238(1985)347.
- [Wes 85] G.D. Westfall, Michigan State University preprint MSUCL-532(1985).
- [Wo 82] C.Y. Wong, Phys. Rev. C25(1982)1461.

Y

- [Ya 81] Y. Yariv and Z. Franenkel, Phys. Rev. C24(1981)488.





MICHIGAN STATE UNIVERSITY LIBRARIES

3 1293 00700 0973